PHD THESIS OF THE UNIVERSITE DE LYON
Perpared at
l'Université Claude Bernard Lyon 1

Doctoral school N°162
MEGA
Mécanique - Energétique - Génie Civil - Acoustique
Doctoral speciality: Acoustics and signal/image processing

Publicly defended on December 7th, 2021, by:
N. Ghigo

Ultrafast Ultrasound Imaging for Simultaneous 2D Wall and Flow Motion of the Abdominal Aorta

---

In the presence of the jury composed of:

Nadjia Kachenoura	Research associate, INSERM,	Reviewer
Jean Provost	Associate professor, Polytechnique Montréal,	Reviewer
Ayache Bouakaz	Research associate, INSERM,	Examinator
Giulia Matrone	PhD, Università degli Studi di Pavia,	Examinator
Stefano Ricci	PhD, Università degli Studi di Firenze,	Examinator
Hervé Liebgott	Professor, CREATIS, UCBL,	Director
Piero Tortoli	Professor, Università degli Studi di Firenze,	Co-Advisor
Didier Vray	Professor, CREATIS, INSA,	Co-Advisor (Invited)
Brahim Harbaoui	Hospital Practitioner, UCBL,	Invited

UNIVERSITE CLAUDE BERNARD – LYON 1

Président de l'Université	M. Frédéric FLEURY
Président du Conseil Académique	M. Hamda BEN HADID
Vice-Président du Conseil d'Administration	M. Didier REVEL
Vice-Président du Conseil des Etudes et de la Vie Universitaire	M. Philippe CHEVALLIER
Vice-Président de la Commission de Recherche	M. Petru MIRONESCU
Directeur Général des Services	M. Pierre ROLLAND

COMPOSANTES SANTE

Département de Formation et Centre de Recherche en Biologie Humaine	Directrice : Mme Anne-Marie SCHOTT
Faculté d'Odontologie	Doyenne : Mme Dominique SEUX
Faculté de Médecine et Maïeutique Lyon Sud - Charles Mérieux	Doyenne : Mme Carole BURILLON
Faculté de Médecine Lyon-Est	Doyen : M. Gilles RODE
Institut des Sciences et Techniques de la Réadaptation (ISTR)	Directeur : M. Xavier PERROT
Institut des Sciences Pharmaceutiques et Biologiques (ISBP)	Directrice : Mme Christine VINCIGUERRA

COMPOSANTES & DEPARTEMENTS DE SCIENCES & TECHNOLOGIE

Département Génie Electrique et des Procédés (GEP)	Directrice : Mme Rosaria FERRIGNO
Département Informatique	Directeur : M. Behzad SHARIAT
Département Mécanique	Directeur M. Marc BUFFAT
Ecole Supérieure de Chimie, Physique, Electronique (CPE Lyon)	Directeur : Gérard PIGNAULT
Institut de Science Financière et d'Assurances (ISFA)	Directeur : M. Nicolas LEBOISNE
Institut National du Professorat et de l'Education	Administrateur Provisoire : M. Pierre CHAREYRON
Institut Universitaire de Technologie de Lyon 1	Directeur : M. Christophe VITON
Observatoire de Lyon	Directrice : Mme Isabelle DANIEL
Polytechnique Lyon	Directeur : Emmanuel PERRIN
UFR Biosciences	Administratrice provisoire : Mme Kathrin GIESELER
UFR des Sciences et Techniques des Activités Physiques et Sportives (STAPS)	Directeur : M. Yannick VANPOULLE
UFR Faculté des Sciences	Directeur : M. Bruno ANDRIOLETTI

Abstract

This thesis is focused on ultrasound imaging for clinical application. The goal is to give to clinicians an ultrasound mode to simultaneously extract wall motion and flow at high frame rate in blood vessels that can be imaged with a convex probe.

Cardiovascular diseases may involve the heart, blood vessels or both. Their formation process is still not fully understood, although it is hypothesized that some parameters related to flow velocity and wall motion could be markers of some pathologies. Assessing such parameters might allow early cardiovascular diseases detection and understanding.

The heart induces fast, transient, complex motions in connected arteries. A high frame rate modality is needed to extract as much information as possible on the condition of the cardiovascular system. Unfortunately, no technique is currently used in clinics for the extraction of both flow and wall pathological markers at high frame rate with a convex probe. Convex probes are used to visualize blood vessels located deeply under the skin. Their relatively low frequency and large field-of-view make them ideal to image large portions of vessels even under a large layer of fat. Therefore, in this thesis, an ultrasound sequence and an algorithm allowing the extraction at high frame rate of both flow and tissue motions parameters is presented. The work focuses on arteries investigated with a convex probe.

There are three main scientific contributions in this thesis:

1. the design of the high frame rate ultrasound sequence,
2. an algorithm for 2D estimation of both flow and tissue motion,
3. an experimental proof of concept.

The ultrasound sequence is based on very few diverging waves transmissions and echoes acquisitions, followed by compounding, to preserve the frame rate while maintaining as much as possible the image quality. The case of deep vessels is considered, in which the frame rate is inherently limited by the long round-trip time of the ultrasound wave. The processing pipeline used an approach that introduces a lateral oscillation in ultrasound images. The images then contain two oscillations, one in the direction of the ultrasound propagation, and one added in the perpendicular direction to the ultrasound propagation. Vectorial velocity fields can be extracted with a 2D phase-based estimator. Validations for both flow and wall motion estimation were performed through an in-house realistic abdominal aorta phantom designed for the experimental tests.

Finally, the clinical proof of concept was performed on a healthy volunteer.

Résumé

Cette thèse est consacrée à l'imagerie ultrasonore, aussi appelée échographie. L'objectif est de fournir aux cliniciens un mode ultrasonore permettant d'extraire simultanément le mouvement pariétal et le flux à une cadence d'imagerie élevée dans les vaisseaux sanguins pouvant être imagés avec une sonde convexe. Les maladies cardiovasculaires regroupent les maladies qui touchent le cœur, les vaisseaux sanguins, ou les deux. Leur processus de formation n'est pas encore totalement compris, bien que l'on suppose que certains paramètres, liés à la vitesse d'écoulement et au mouvement de la paroi, pourraient être des marqueurs de certaines de ces pathologies. L'évaluation de ces paramètres pourrait permettre une détection précoce de ces maladies. Le cœur induit des mouvements rapides, transitoires et complexes dans les vaisseaux sanguins et notamment dans les artères. Une modalité à haute cadence d'images est alors nécessaire pour extraire le plus d'informations possible sur l'état du système cardiovasculaire. Malheureusement, aucune technique n'est actuellement utilisée en clinique pour extraire à la fois des marqueurs de flux et de pathologie de la paroi à des fréquences d'imagerie élevée avec une sonde convexe. C'est pourquoi, dans cette thèse, une séquence ultrasonore et un algorithme permettant l'extraction des paramètres de flux et de tissu, à des taux d'imagerie élevés sur des artères évaluées avec une sonde convexe, sont présentés.

Il y a trois contributions scientifiques principales dans cette thèse :

1. la conception de la séquence ultrasonore à une haute cadence d'imagerie,
2. un algorithme pour l'estimation du mouvement 2D du flux et du mouvement tissulaire,
3. une preuve de concept expérimentale.

La séquence ultrasonore est basée sur l'acquisition de très peu d'ondes divergentes, suivie d'une méthode de composition d'images (i.e. compounding), afin de préserver la cadence d'imagerie tout en augmentant la qualité de l'image finale. Cette thèse se concentre sur l'étude des vaisseaux profonds, où la cadence d'imagerie est intrinsèquement limitée par le temps d'aller-retour conséquent de l'onde ultrasonore. La méthode d'estimation de mouvement proposée introduit une oscillation latérale virtuelle dans l'imagerie ultrasonore qui, couplée à un estimateur 2D basé sur la phase, permet d'extraire des champs de vitesse vectoriels. Les validations de l'estimation du flux et du mouvement de la paroi ont été effectuées expérimentalement sur un fantôme d'aorte abdominale réaliste conçu au laboratoire.

Enfin, la preuve de concept clinique a été réalisée sur un volontaire sain.

Riassunto

Questa tesi è centrata sull'imaging a ultrasuoni per applicazioni cliniche. L'obiettivo è quello di ottenere una modalità ad ultrasuoni capace di valutare, simultaneamente e ad alto frame rate, il movimento delle pareti e il flusso nei vasi sanguigni che possono essere visualizzati con sonde convesse.

Le malattie cardiovascolari possono coinvolgere il cuore, i vasi sanguigni o entrambi. Il loro processo di formazione non è ancora completamente compreso, anche se si ipotizza che alcuni parametri relativi al flusso e al movimento delle pareti potrebbero essere marcatori di alcune patologie. La valutazione di questi parametri potrebbe facilitare la diagnosi precoce di queste malattie.

Il cuore induce nelle arterie movimenti di breve durata e complessi: una modalità di indagine ad alto frame rate è quindi necessaria. Sfortunatamente, nessuna tecnica ad alto frame rate è attualmente disponibile in clinica per l'estrazione di entrambi i marcatori patologici di flusso e parete, quando si renda necessario l'utilizzo di una sonda convessa. Le sonde convesse sono utilizzate per visualizzare i vasi sanguigni situati in profondità sotto la pelle. La frequenza relativamente bassa e il grande campo visivo caratteristici delle sonde convesse le rendono ideali per l'analisi di grandi porzioni di vasi anche sotto un ampio strato di grasso. Pertanto, in questa tesi, è stata proposta una sequenza di trasmissione di ultrasuoni da una sonda convessa e un algoritmo di elaborazione degli echi che permette l'estrazione ad alto frame rate dei parametri di flusso e di movimento dei tessuti.

Questa tesi presenta tre principali contributi scientifici :

1. una sequenza originale di trasmissione di ultrasuoni per imaging ad alto frame rate,
2. un nuovo algoritmo per la stima del movimento 2D del flusso e del movimento dei tessuti,
3. la verifica sperimentale di quanto proposto.

Il metodo proposto prevede la trasmissione di pochissime onde divergenti, seguita da un metodo di composizione dell'immagine (i.e. compounding), al fine di aumentare la qualità dell'immagine finale preservando il frame rate . Questa tesi è concentrata sullo studio di vasi profondi. Le immagini sono ottenute creando un'onda di pressione a doppio campo, oscillante sia nella direzione della propagazione degli ultrasuoni che nella direzione perpendicolare. I campi di velocità vettoriali possono essere ottenuti con uno stimatore basato sulla fase 2D. Le misure ottenute sul flusso e sul movimento della parete sono state validate sperimentalmente su un fantoccio realistico dell'aorta addominale appositamente progettato.

Infine, la metodologia proposta è stata testata su un volontario sano.

Table of Contents

List of Abbreviations

1D	One-Dimensional
2D	Two-Dimensional
3D	Three-Dimensional
AA	Abdominal Aorta
AAA	Abdominal Aorta Aneurysm
BF	BeamForming
BM	Block Matching (methods)
BMF	Blood Mimicking Fluid
BP	Blood Pressure
CFM	Color Flow Mapping
CNR	Contrast to Noise Ratio
CVD	CardioVascular Diseases
CW	Continuous Wave (Doppler)
DAS	Delay And Sum (beamforming)
ECG	ElectroCardiogram
EVAR	EndoVascular Aortic Repair
FFT	Fast Fourier Transform
FOV	Field Of View
FPS	Frame Per Second
ILT	IntraLuminal Thrombus
IQ	In-phase and Quadrature
IUS	International Ultrasonics Symposium
MI	Mechanical Index
NCC	Normalized Cross-Correlation
NRMSE	Normal Root Mean Square Error
OAR	Open Aortic Repair
OF	Optical Flow (methods)
PII	Pulse Intensity Integral
PIV	Particle Image Velocimetry
PPI	Pulse Pressure squared Integral
PRF	Pulse Repetition Frequency
PSF	Point Spread Function
PSV	Peak Systolic Velocity
PVA	PolyVinyl Alcohol
PW	Pulse Wave (Doppler)
PWI	Pulse Wave Imaging
PWV	Pulse Wave Velocity
ROI	Region Of Interest
RF	Radio Frequency
SNR	Signal to Noise Ratio
SPTA (intensity	Spatial Peak Temporal Average
TGC	Time Gain Compensation
TI	Thermal Index
TO	Transverse Oscillation (method)
ULA-OP Platform	ULtrasound Advanced Open
US	UltraSound
VS	Virtual Sources
WSR	Wall Shear Rate
WSS	Wall Shear Stress

Mathematical notations

$\cos(\cdot)$	cosine function
$\sin(\cdot)$	Sinus function
$\tan(\cdot)$	Tangent function
$\arctan(\cdot)$	Inverse tangent function
j	Imaginary number
$\Im(\cdot)$	Imaginary function
$\Re(\cdot)$	Real function
I	Imaginary part of a signal
Q	Real part of a signal
$\mathcal{F}(\cdot)$	Fourier transform
$\mathcal{F}^{-1}(\cdot)$	Inverse Fourier transform
$\delta(\cdot)$	Dirac function
$\lvert \cdot \rvert$	Absolute function
$\lVert \cdot \rVert$	Euclidian norm function
$\circledast$	Convolution operator
$*$	Correlation operator
*	Conjugate notation
$\exp(\cdot)$	Exponential function
$\int \cdot$	Integral notation
$\mathbb{E}$	expected operator
$\frac{\partial \cdot}{\partial \cdot}$	Derivation notation
∇_{xz}	Spatial gradient
R_t	Radon transform function
$\hat{R}$	Mean complex autocorrelation function
$g(\cdot)$	Gaussian function
σ	Standard deviation of the Gaussian function
α	Attenuation (dB.m^{-1}.Hz^{-1})
ρ	Mass density (Kg.m^{-3})
μ	Viscosity (Pa.s)
υ	Poisson's ratio
c	Speed of sound (m/s)
T_w	Temperature of water (°C)
E_{young}	Young's modulus (Pa)
f_0	Emitted frequency (Hz)
f_r	Received frequency (Hz)
f_d	Doppler frequency (Hz)
f_t	Tangential frequency (Hz)
λ	Wavelength of ultrasound (m)
λ_x	Lateral wavelength (m)
λ_z	Axial wavelength (m)
λ_t	Tangential wavelength (°)
T_{PRF}	Pulse repetition time (s)

$F_{\#}$	F-number
w_{ap}	Notation of the active aperture
L	Total width of the active aperture w_{ap} (m)
N_{cycle}	Number of emission/reception cycles
N_{frame}	Number of frames
W_{vessel}	Width of the vessel visible in an ultrasound image (m)
z_f	Focus depth (m)
h	2D-Point Spread Function
h_x	Lateral Point Spread Function
h_z	Axial Point Spread Function
R	Radius of the probe (m)
E	Element of the probe
(x_e, z_e)	Cartesian coordinates of element E
(θ_e, R)	Polar coordinates of element E
w_e	Width of element E (m)
t	Time (s)
$s(t)$	Acoustic signal
A	Amplitude term
ϕ	Phase term
$\Delta\phi$	Phase Difference
$p(z,t)$	Pressure (Pa)
S	Scatterer notation
r_s	Radial distance of a scatterer S (m)
r_{AA}	Radial distance necessary to image the Abdominal Aorta (m)
v	Velocity notation (m/s)
v_x	Lateral velocity (m/s)
v_z	Axial velocity (m/s)
v_t	Tangential velocity (°/s)
v_r	Radial velocity (m/s)
v_w	Velocity of the wall w (m/s)
a_w	Acceleration of the wall w (m/s²)
τ	Estimation lag (s)
Δx	Lateral displacement (m)
Δz	Axial displacement (m)
$\Delta t°$	Tangential displacement (°)
Δt	Time shift (s)
(w_1, w_2)	Two consecutive windows in a region-of-interest
(W_1, W_2)	Fourier transform of (w_1, w_2)
(i,j)	Position of a pixel
$I(i,j)$	Intensity of a pixel
$(\theta_{i,j}, r_{i,j})$	Polar coordinates of a pixel
β	Angle between a Virtual Source and the center axis of the probe (°)
h_v	Thickness of the vessel (m)
R_v	Radius of the vessel (m)
R_{lumen}	Radius of the lumen(m)

Thesis introduction

This thesis is focused on ultrasound imaging for blood vessels that can be imaged with a convex probe, such as the abdominal aorta. The goal is to give to clinicians an ultrasound mode to simultaneously extract wall motion and flow at high frame rate even in deep vessels. This could lead to significant markers on blood pattern, wall motion and even wall and flow interaction, potentially useful to diagnose, monitor and better understand vascular diseases.

This thesis is divided into 4 chapters.

The first chapter serves as a general introduction. The cardiovascular system is described along with some common arterial disorders. The basic principles of ultrasound imaging are then introduced, and the different modes currently used in clinic are discussed. The standard focused imaging and ultrafast imaging approaches are compared. Clinical markers of cardiovascular diseases that can be extracted from flow and wall motion are presented. These markers are extracted from different ultrasound sequences, and this chapter is concluded by the interest of the simultaneous assessment of flow and wall characteristics.

The second chapter presents the state of the art of the standard motion estimation techniques commonly used in vascular ultrasound imaging. First, the Doppler-based techniques are described with both the frequency-based and phase-based approaches. Then, speckle-tracking, optical flow and transverse oscillation approaches are described. After discussing the standard estimation techniques, the state of the art of simultaneous measurement of tissue motion and flow is presented. Several teams from across the world have worked on this subject, focusing on the use of linear array transducers. This second chapter concludes with the goals and the selected approach chosen during the thesis for the simultaneous measurement of tissue and flow motion using a convex probe.

The third chapter.is focused on the ultrafast ultrasound scheme that will be used during the rest of this thesis. First, the convex array transducer CA631 of Esaote SpA (Italy) used during this thesis was studied. Its ultrasound transmitted pressure field is characterized thanks to hydrophone measurements. Knowing the characteristics of the probe is the first essential step needed to understand the acquired signal. Then, an ultrasound emission sequence capable of conserving a high framerate while furnishing a sufficient image quality in deep tissue was studied. Several compounding schemes were investigated with few sub-images. Then, a delay-and-sum algorithm was used and a way to consider the elements' position and directivity is presented. At the end of this chapter, all the necessary steps for obtaining suitable ultrasound images have been described and will be used for the rest of the thesis.

The fourth chapter is the description of the methodology for the simultaneous measurement of flow and tissue motion at high frame rate. Transverse oscillation by Fourier filtering approach is implemented on a convex probe and motions are then assessed with a 2D phase-based estimator. After this methodological part, the estimator is validated based on *in vitro* experiments. An experimental set-up generating flow and tissue motion was used with an in-house phantom. The

process to extract the pulse wave velocity from the tissue motion estimation is described. The fourth chapter concludes with a discussion on the *in vitro* experiments and the possible challenges for the *in vivo* passage.

In chapter five, an *in vivo* study on a healthy volunteer is presented. First, the safety of the volunteer is ensured by preliminary safety measurements on the ultrasound sequence. Vectorial flow and wall motion estimation obtained on the abdominal aorta are then presented. The chapter concludes with the limitation, opportunities, and future works to go further in clinical usability.

This thesis is concluded by the overall conclusion and perspectives for this work.

Chapter 1: General Background

1.I Human cardiovascular system

The cardiovascular system (from the Latin words for "heart" and "vessel"), also called the circulatory system, is an organ system allowing blood to circulate through the body. It is constituted of the heart, the blood vessels and blood. The circulatory system is seen as having two components: a systemic circulation and a pulmonary circulation. The pulmonary circulation transports deoxygenated blood between the heart and the lungs, where the blood absorbs nutrients and oxygen while releasing carbon dioxide. The newly oxygenated blood circulates through the systemic circulation from the heart to the rest of the body, providing oxygen and nutrients. The pulsatile contractions of the heart are the source of blood circulation into the blood vessels.

1.I.A The heart

The heart is a muscle organ which pumps blood through the body. It is divided into four different chambers: the upper left and right atria and the lower left and right ventricle (Figure 1.1). The upper

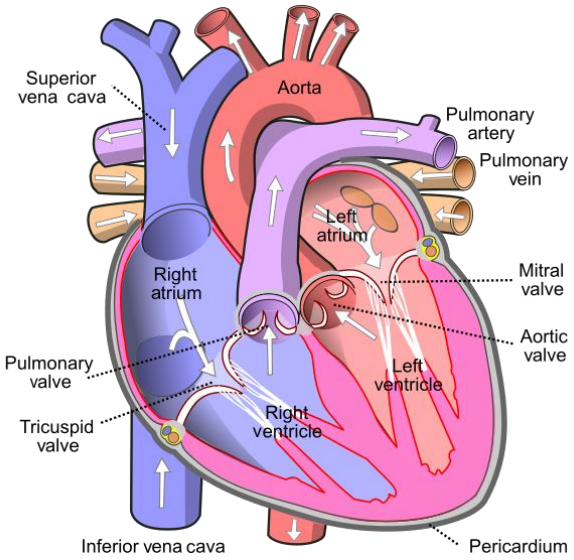

Figure 1.1: Representation of the heart, the main organ of the circulatory system. The blood circulates through the body as a result of the contraction of the heart's four chambers: two atria and two ventricles. [Wikimedia Commons - Wapcaplet].

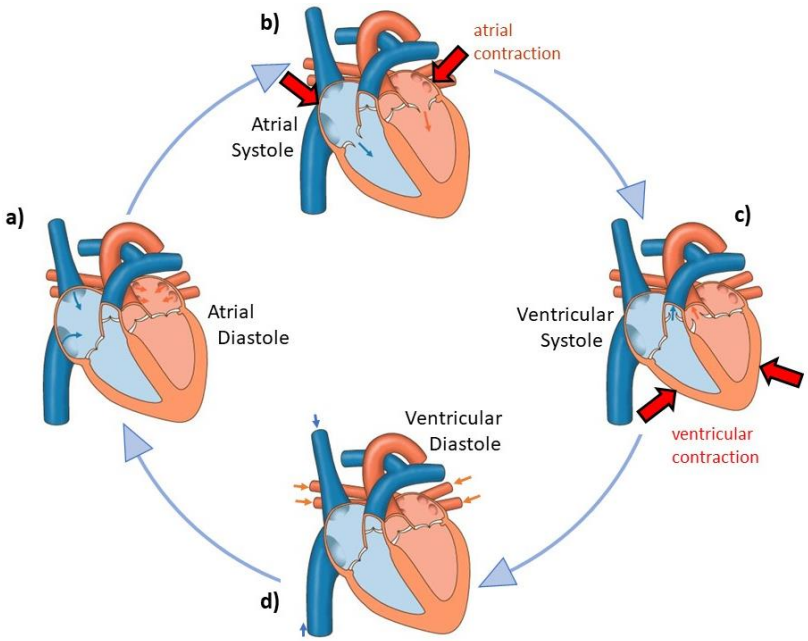

Figure 1.2: Schematic representation of a cardiac cycle. a) Atrial Diastole: all heart muscles are in relaxation; all valves are closed. The blood returns to atria. b) Atrial Systole: atria contraction pushes the blood to the ventricles; Mitral and tricuspid valves are opened. c) Ventricular Systole: ventricles contraction pushes the blood to arteries. Mitral and tricuspid valves are closed; pulmonary and aortic valves are opened. d) Ventricular Diastole: all heart muscles are in relaxation; all valves are closed. The blood returns to atria by the vena cavae and pulmonary vein. [modified from Servier Medical Art images]

part of the heart is the attachment point for several large blood vessels: the venae cavae, aorta and pulmonary trunk. The lower part of the heart is called the apex.

The deoxygenated blood from the systemic circulation enters the heart's right atrium through the superior and inferior venae cavae and is ejected in the right ventricle. It is then pumped into the pulmonary circulation where it is oxygenated. The newly oxygenated blood reenters the systemic circulation by the aorta passing through the left atrium and left ventricle. A schematic view of a cardiac cycle is pictured in Figure 1.2.

The heart activity can grossly be divided into two principal phases: the systole and the diastole. During systole, the myocardium contracts, ejecting blood to the lungs (right ventricle) and to the body (left ventricle). During diastole, the cardiac muscle dilates expanding the heart's volume and causing blood to flow in.

The cardiac muscle, also called myocardium, is responsible for the heart contraction, which generates the blood circulation. These contractions are commanded by the sinoatrial node, a group of cells located in the right atrium's wall and producing an electrical impulse contracting the myocardium. This electric activity is frequently monitored using an electrocardiogram (ECG). The ECG is easily recorded by placing electrodes directly on the skin and is often used as a true heart's clock when synchronized with another imaging method. The ECG makes it possible to know exactly in which heart's phase the images are obtained.

The ECG shows four principal spots of interest (Figure 1.3):

1. The P wave corresponds to the atrial contraction.
2. The QRS complex combine the Q, R and S waves that occur in a rapid succession. It corresponds to the ventricular contraction and the atrial dilatation.

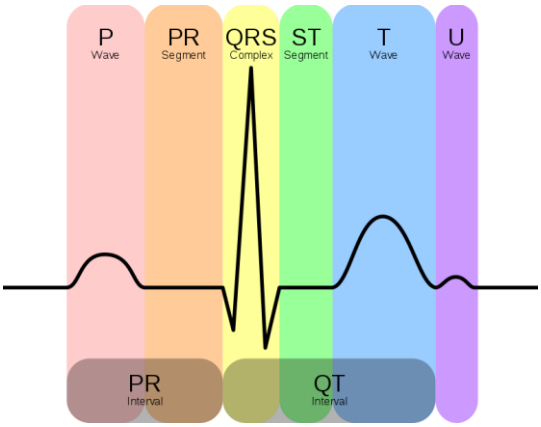

Figure 1.3: Schematic plot of a normal electrical impulse for a human heart as seen on a ECG. [Wikimedia Commons – Hank van Helvete].

3. The T wave corresponds to the ventricular dilatation.
4. The U wave has a low amplitude and is often completely absent. It causes remain yet unknown.

1.I.B Blood vessels

The blood circulates in the body through blood vessels, which can be roughly decomposed in three different categories:

- The arteries transport blood from the heart to the rest of the body. Most arteries carry oxygenated blood; the two exceptions are the pulmonary and the umbilical arteries. The diameter of healthy arteries can go from more than 2.5 cm near the heart to 2 mm for the smallest. Arteries are subjected to high pressure, pulsatile blood flow.
- The veins transport blood toward the heart. Most veins carry deoxygenated blood; the two exceptions are the pulmonary and umbilical veins. They are similar in size to the arteries but possess valves to compensate for a lower blood pressure and prevent the formation of backflow.
- The capillaries are the smallest blood vessels and have a diameter of less than 10 µm. They are responsible for nutrients and oxygen exchanges with the surrounding tissues which is made possible by their thin permeable walls. The capillaries receive rich blood from the arteries, the blood then becomes poor after nutrient exchanges with the surrounding tissues. Finally, capillaries merge together forming veins, which then return blood back to the heart through the venae cavae. The capillaries that supply the large blood vessels are called the *vasa vasorum* (in Latin, the “vessels of the vessels”).

Blood vessels are often depicted as tubes composed of three layers (Figure 1.5). The internal cavity, containing the blood, is referred to as the lumen.

1. The inner layer, the intima, is directly in contact with the blood. It is the thinnest layer and is highly elastic.
2. The middle layer, the media, is made of muscle cells, elastic tissue, and collagen. It is the thickest layer in arteries.

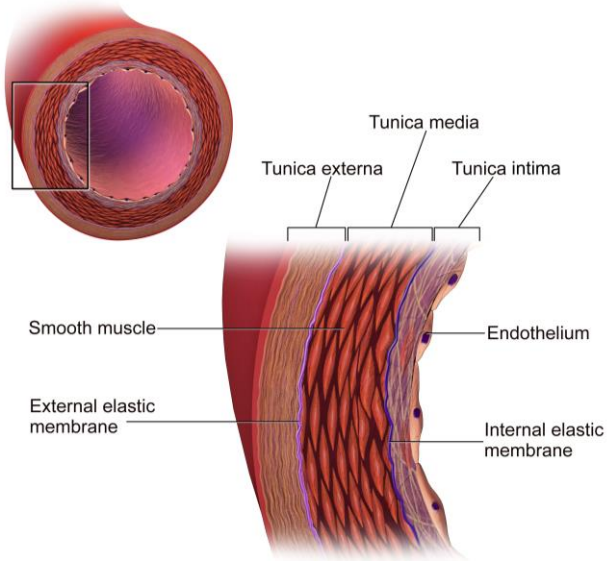

Figure 1.4 : Schematic representation of a blood vessel wall. [Wikimedia Commons – Blausen].

3. The outer layer, the adventitia, is mainly composed of elastic tissue, and collagen. In the larger blood vessels, it also contains nerves and capillaries (i.e. vasa vasorum). It is the thickest layer in veins.

The intima and media layers can be difficult to separate from one another with non-invasive medical procedures. Hence, they are often considered as one medium: the intima-media.

1.II Usual pathology markers on blood vessels

In this section, usual pathology markers of vascular diseases, i.e. diseases of the blood vessels, are presented. We here focus on pathology markers accessible without any imaging techniques and clinical markers obtained through ultrasound imaging will be discussed in section 1.VII.

Cardiovascular disease (CVD) is a class of diseases that involve the heart, blood vessels or both. The state of the heart and of the blood vessels are inherently linked as they are connected to each other (W. Nichols, O'Rourke, and Vlachopoulos 2011). Hence the presence of a heart disease often tends to fragilize blood vessels, leading to arterial disease. Similarly, a defect in a blood vessel can have a strong impact on the heart.

Cardiovascular diseases are the leading cause of death worldwide, which can be explained because of its predominance in the elderly. It is estimated that up to 90% of CVD may be preventable (McGill, McMahan, and Gidding 2008). Prevention of CVD involves reducing the exposure to risk factors through healthy eating, exercise, avoidance of tobacco smoke, limiting alcohol intake etc. Treating risk factors, such as high blood pressure, blood lipids and diabetes is also beneficial.

The underlying mechanisms of CVD vary depending on the disease but are almost always linked with a weakness in blood vessels. One of the predominant vascular diseases, called atherosclerosis, is the formation of a plaque inside the lining of the wall. Plaque formation is generally a slow process that takes decades to evolve into a pathological case. Almost all people after 60 years old have some degree of atherosclerosis as plaque formation usually starts during childhood (Hong 2010) and worsens with age through different steps (Figure 1.6). The first step is the presence of a fatty streak that cannot be distinguished from a healthy artery. The lesion is the first stage that can be visible using

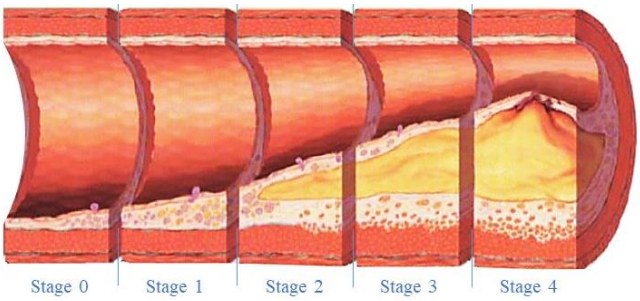

Figure 1.5: Progression of atherosclerosis: Stage 0 healthy/fatty streak, Stage 1 lesion, Stage 2 atheroma, Stage 3 fibrous plaque, and Stage 4 advanced plaque/rupture. [Wikimedia Commons – Npatchett].

histology. Then comes the formation of an atheromatous plaque. The disease becomes clinically apparent with the formation of the fibrous plaque, which is the third stage. The last stage will depend on the patient, localization of the artery, and still unknown parameters. It may evolve into a critical stenosis, i.e. an abnormal narrowing of the lumen that drastically reduces the diameter of the artery. Another possibility is the formation of a thrombus, a blood clot, that can clog a blood vessel. The last option is the formation of an aneurysm, a local distortion of the artery diameter, that can lead to its rupture. In all cases, the last stage can be deadly since it can result in oxygen deprivation for vital organs or in hemorrhage. Even without evolving to the last stage, a rupture of the fibrous plaque can occur and creates a dangerous clot downstream of the original location.

Several markers can be the sign of a potential vascular disorder. During a typical vascular exam, the clinician will access the blood pressure with a sphygmomanometer in the shape of a brassard. When blood flows through the blood vessels, it applies a pressure against its walls, called blood pressure (BP). In a healthy adult at rest BP should approximately be equal to 120 mmHg during systole and 80 mmHg during diastole (denoted 120/80 mmHg). If the BP is significantly higher, the patient will be described as having hypertension, also known as high blood pressure. Hypertension is a major risk factor for CVD and other major diseases (Lackland and Weber 2015).Lifestyle changes and medications can lower blood pressure and decrease the risk of long-term health complications.

The pulse is the heartbeat noticeable by palpation of an artery. It Is typically access at the carotid, radial, femoral, popliteal, posterior tibial and dorsalis pedis arteries. By checking that the pulse is adequate and equal on both sides of the body, doctors can localize potential vessel disorders such as the presence of a thrombose. A pulse palpation gives information on the heart rate and its regularity, and on the volume of blood ejected by the left ventricle according to the pulse amplitude.

Clinicians also perform a global physical exam looking for any abnormal skin coloration or visible pathologies such as varicose veins or leg ulcers. The patient is weighted, and their body mass index calculated. Questions to access life hygiene are also relevant (smoking, physical exercise etc.). All these measurements and observations are valuable tools to quantify cardiovascular risk and act accordingly.

1.III Abdominal aorta

The aorta is the main and largest artery in the human body, originating from the left ventricle of the heart and extending down to the abdomen. It carries oxygenated blood to all the body. The aorta is typically divided into different sections according to the blood flow direction (see Figure 1.7):

- The ascending aorta corresponds to the beginning of the aorta where blood flows upward from the heart.

- The aorta then makes a hairpin turn called the aortic branch
- The rest of the aorta is called the descending aorta as the blood flows downward. The descending aorta is typically divided into two subsections:
    - The thoracic aorta corresponds to the beginning of the descending aorta travelling in the thorax.
    - The abdominal aorta (AA) corresponds to the very end of the aorta, after the diaphragm. The AA then divides into two paired arteries, the common iliac arteries. It is usual to divide the abdominal aorta into two segments due to changes in wall composition:
        - The suprarenal abdominal segment is inferior to the diaphragm and superior to the renal arteries.
        - The infrarenal abdominal segment is inferior to the renal arteries and superior to the iliac bifurcation.

The infrarenal abdominal aorta is particularly prone to atherosclerotic plaque formation while the thoracic aorta is relatively resistant. Major differences in wall composition and hemodynamic conditions have been implicated in the differential localization of disease in the infrarenal aorta.

The flow in the AA is particularly complex as a result of the multiple branches delivering blood to the organs in the abdomen (Tortoli et al. 2002). The renal arteries take up to 20% of total cardiac output, causing the infrarenal aorta to experience reversed flow and, though, oscillatory wall shear stress (Amirbekian et al. 2009). There is also a reduced amount of vasa vasorum in the AA (compared to in the thoracic aorta); consequently, the tunica media must rely mostly on diffusion for nutrition, which makes it more susceptible to damage (MacSweeney, Powell, and Greenhalgh 1994). Furthermore, the proportion of elastin, responsible for the elasticity of the vessel wall, diminish the more the aorta moves away from the heart. The rigidity of the infrarenal aorta also explains its predominance for CVD.

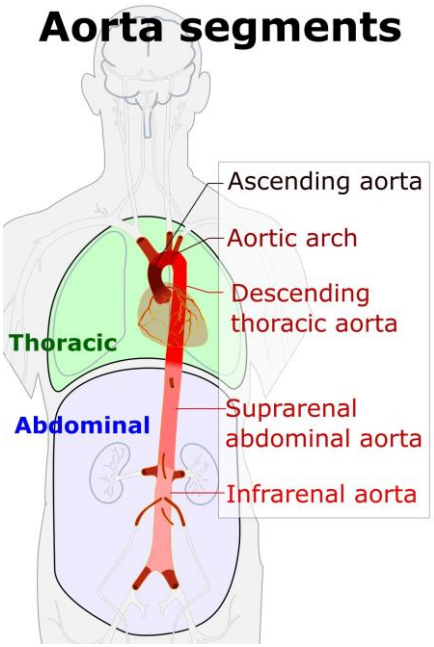

Figure 1.6: Schematic representation of the different sections of the abdominal aorta. [Wikimedia Commons – Edoarado].

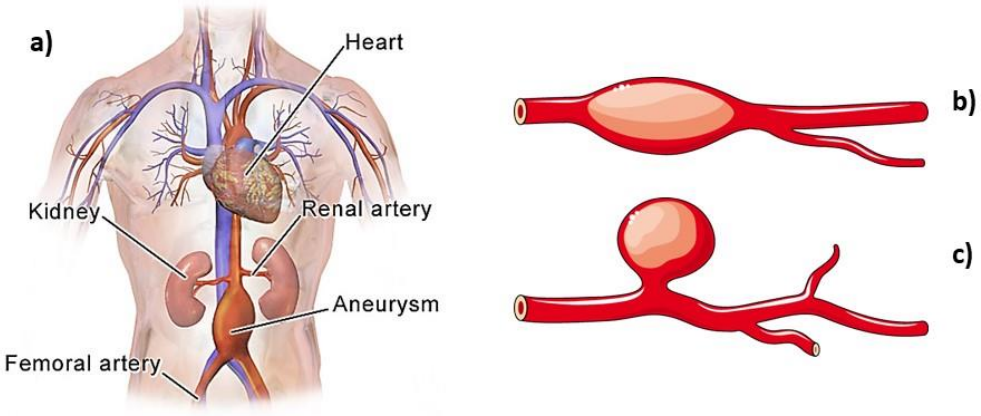

Figure 1.7 : a) Diagram of an infrarenal aneurysm. The diameter of the abdominal aorta is dilated by more of 50%. [Wikimedia Commons – BruceBlaus]. An abdominal aorta aneurysm can take two shapes: a) fusiform; b) saccular aneurysm. [Servier Medical Art images]

1.IV Abdominal Aorta disorders

The infrarenal portion of the aorta is vulnerable to the development of atherosclerotic plaque that weakens the artery walls, allowing other pathologies to develop. A prominent example of such disease is the Abdominal Aortic Aneurysm denoted AAA. AAA is characterized by a localized enlargement of the diameter of the abdominal aorta of more than 50% of the normal diameter (Figure 1.8). As the infrarenal abdominal aorta is the most fragile part of the aorta, about 85% of all AAA occur below the kidneys. AAA can take two different shapes: it is mostly fusiform (symmetrical ballooning on both sides of the blood vessel) but can also be saccular (ballooning only on one side) (Figure 1.8).

The AAA is particularly dangerous as its diameter grows until it ruptures. If ruptured the mortality is around 90%, with a vast and rapid hemorrhage (Kent 2014). This explain the needs to intervein before the AAA ruptures, which may be difficult as AAA tends to be asymptomatic until ruptured. AAA are often diagnosed during a routine ultrasound check-up. Some countries have a nationwide AAA screening program to detect as many people affected as possible (Wanhainen, Hultgren, and Linne 2017; Jawien et al. 2014; Scott 2002).

In more than 70% of the cases, IntraLuminal Thrombus (ILT) covers the AAA walls. While ILT is frequently observed in aneurysmal disease, the complete vessel occlusion is a comparably rare event associated with a high rate of mortality. The impacts of the presence of ILT are still up to debate, though it has been showed it promotes aneurysm development via localized hypoxia at the underlying aortic wall (Piechota-Polanczyk et al. 2015). The ILT has repeatedly been suggested to protect the aneurysm from rupture by reducing the peak wall stress, acting like a buffer. However as large ILT are associated with faster AAA growth, its weakening effects for the aorta walls seems predominant over the wall stress relief it may provide.

Another complication of AAA is the risk of blood clots. Small blood clots can develop in the aortic aneurysm where blood tends to be stagnant. If a blood clot breaks loose from the aneurysm, it can block a blood vessel elsewhere, possibly causing serious complications.

AAA is not to be confounded with a pseudoaneurysm, or false aneurysm. A pseudoaneurysm often occurs after a severe trauma, where most of the aortic wall has been breached, and blood collects just outside the vessel preventing further blood from escaping the vessel (Figure 1.9).

The abdominal aorta can also rupture due to an aortic dissection. Aortic dissection occurs when an injury to the innermost layer i.e. the intima, allows blood to flow between the layers of the aortic wall, forcing the layers apart and forming a channel within the vessel itself (Figure 1.9).

1.V Clinical interventions

The threshold for repair of an abdominal aorta aneurysm varies slightly from individual to individual, depending on the balance of risks and benefits when considering repair versus ongoing surveillance. However, intervention is usually recommended if the AAA has a diameter larger than 5.5 cm in males and 5 cm in females (Kent 2014) ; or if its growth increases more than one centimeter per year (Keisler and Carter 2015). However, these recommendations are known to be unreliable and other indicators are still needed. Two modes of repair are available: Open Aortic Repair (OAR), and EndoVascular Aortic Repair (EVAR). OAR is the first historical surgery available, with the first recorded interventions dating back to the ancient Greeks. It has since been progressively replaced by EVAR that has less perioperative mortality (Greenhalgh 2004). However, OAR is still in use if the patient has a relatively good physical condition, if he is not eligible for EVAR, or if he suffers from aneurysm advanced symptoms.

1.V.A Open aortic repair

Open Aortic Repair (OAR) consists in a large surgical incision allowing the clinicians to access the disease part of the aorta. In presence of an aneurysm, the aneurysmal portion of the aorta is replaced with a graft sewed into the proximal and distal aorta walls (Figure 1.10). The aneurysmal sac is then closed around the graft. Often, the aorta and its branching arteries are cross clamped during open surgery in order to prevent hemorrhage. This technique leaves the branches of the aorta without blood during the time it takes to sew in the graft, potentially resulting in ischemia (Chong et al. 2009). In infrarenal aneurysms, the relative tolerance of the lower extremities to ischemia allows surgeons to clamp with low risk of ill effect.

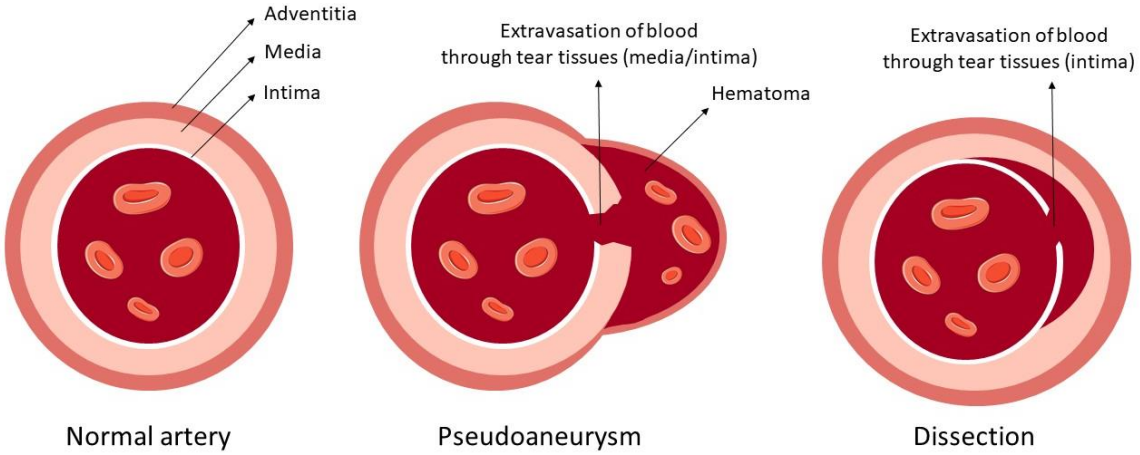

Figure 1.8: Diagram of an healthy artery, a pseudoaneurysm and a dissection. In a pseudoaneurysm, a hematoma form through a rupture in the media/intima medium. In a dissection, an hematoma form through a rupture in the intima medium. [blood cells from Servier Medical Art images]

The main drawback of open repair is the large physiologic demand of the operation, which is associated with increased rates of short-term mortality (Hertzer et al. 2002). This major operation is often difficult especially for older patients and full recovery time, i.e. full recovery of the pre-operative energy, can take up to 6 months.

1.V.B Endovascular aneurysm repair

EndoVascular Aneurysm Repair (EVAR) is a minimally invasive surgery used to treat pathology of the aorta and most commonly aneurysm. An endograft is introduced into the patient's femoral artery all the way to the aneurysmal portion of the AA. The endograft is then deployed, with a special care being paid to not block the flow of the renal arteries during the process. The upper part of the endograft deploys first, followed by the lower part passing through the beginning of the iliac arteries. This endograft acts as an artificial lumen, protecting the aneurysm sac from more blood pressure and further dilatation (Figure 1.11). With the decrease of pressure, the aneurysm usually thrombosis and shrinks in size overtime (Greenhalgh and Powell 2008). Due to the complexity of the vascular system, specifically near the renal arteries, and the risk of ischemia, standard EVAR can be contraindicated in

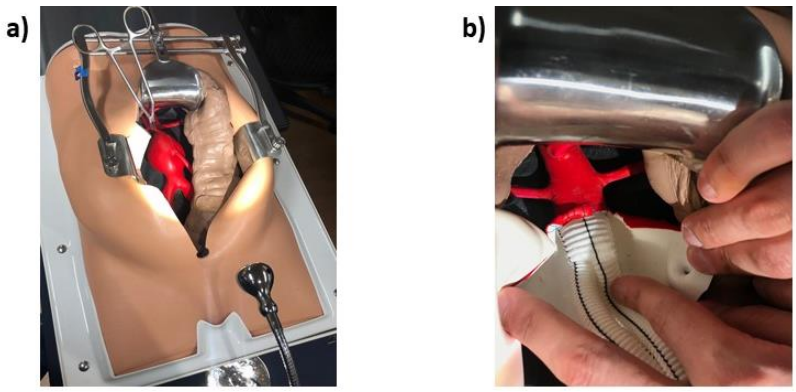

Figure 1.9: (a) Open infrarenal aortic repair on a model with an infrarenal aortic cross-clamp in place, (b) front wall suture line with a bifurcated graft. [Wikimedia Commons – Bakerstmd]

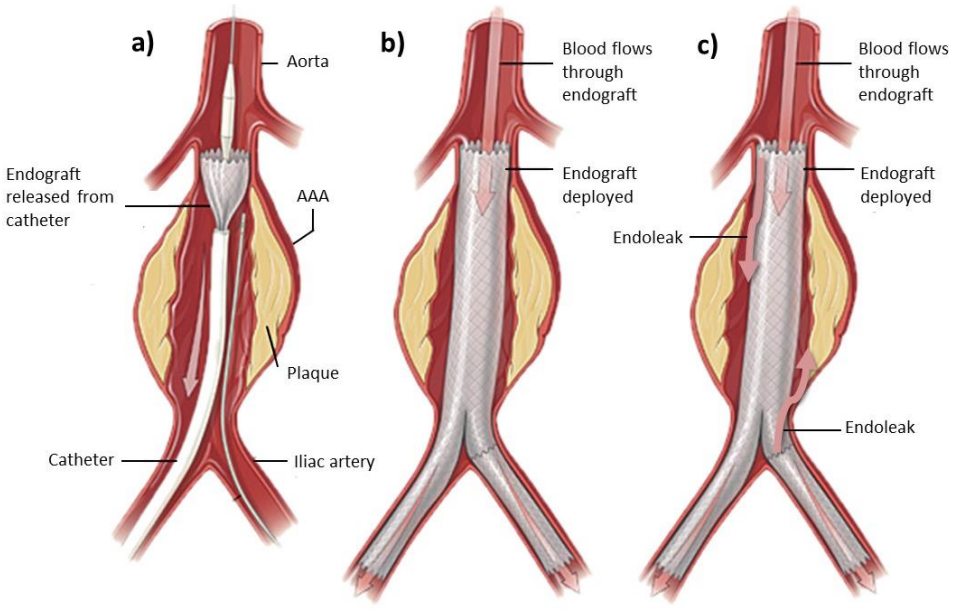

Figure 1.10: Sketch of an endovascular aneurysm repair. (a) Upper part deployment of the endograft in the aneurysmal part of the aorta. (b) Endograft fully and successfully deployed in both iliac arteries. (c) Endograft deplayed with the presence of endoleaks both at the neck of the attachment site and in the iliac arteries (Type I endoleak). [Wikimedia Commons – US National Institutes of Health]

some cases. This is typically the case if the aneurysm happens too close to the renal arteries as there will be an inadequate length of aorta for the endograft attachment. In such cases, special endografts with custom-made fenestrations (i.e. holes) for conserving correct blood supply may be used, or the patient may undergo OAR.

EVAR has a lower mortality rate than OAR. The reduction in death, however, does not persist long-term when the high operation risk of OAR is over. After a few years the survival after repair is similar with EVAR or open surgery (Greenhalgh 2004). This observation may also be explained by some durability problems encountered by some endografts, causing the need for additional surgical procedures. The main durability problem of EVAR is endoleaks i.e. a leak of blood into the aneurysm sac even after the endograft is deployed. These endoleaks are quite common and may be left untreated if the remaining blood pressure on the aneurysm sac is low and if its size does not grow. Five different types of endoleaks exist depending on where the leak of blood originates from: the type I is pictured in Figure 1.11.c. The major interest of EVAR today lies in the improvement of the endografts to avoid endoleaks and to adapt them to all AAA morphology.

1.VI Ultrasound Imaging

All sound waves with frequencies higher than 20 kHz i.e. higher than the standard upper audible limit of human hearing; are defined as ultrasound (Figure 1.12). In 1794, Lazzaro Spallanzani was the first to demonstrate that non-audible sound existed by studying the phenomenon of echolocation in bats (Spallanzani 1794). The first technological application of ultrasound was an attempt to detect submarines by Paul Langevin in 1917 (Wade 2000). The use of ultrasound as a diagnostic tool started in 1942 when the neurologist Karl Dussik tried to detect brain tumors (Dussik 1942).

1.VI.A Clinical context

UltraSound (US) has been used for assessment of cardiovascular properties since the 50s (Satomura 1957). Ultrasound imaging is both a qualitative and quantitative diagnosis tool. It is generally used to

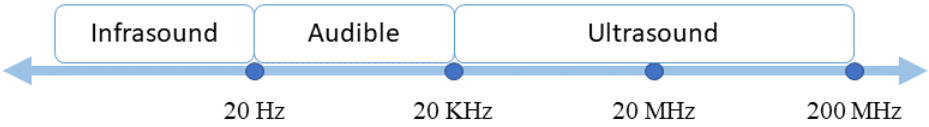

Figure 1.11: Frequency range of sound. Ultrasound corresponds to frequency higher than 20 kHz.

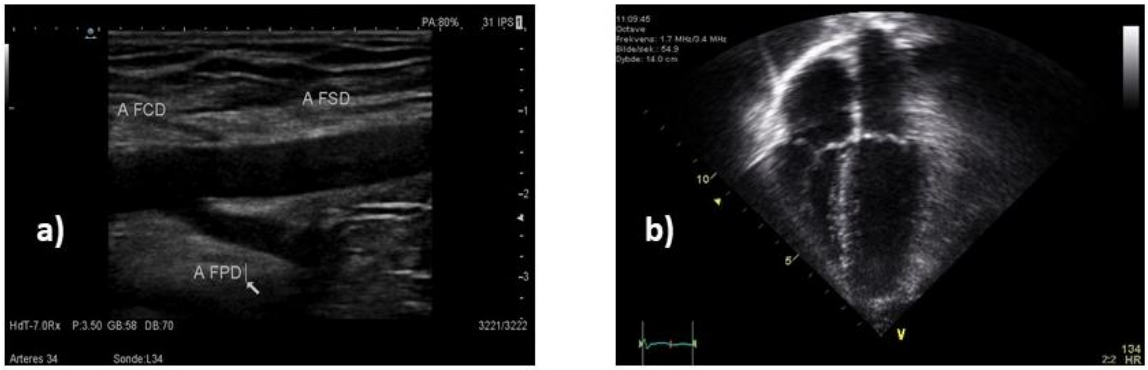

Figure 1.12: Conventional ultrasound images: a) division of the common right femoral into the superior and posterior femoral arteries *[Courtesy of Pr. Anne Long, Hôpital Edouard Herriot, Lyon, France]* ; b) Echocardiogram four chambers.

create an image of the organ of interest. The clinical interpretation is then based on the anatomical aspect of the images -with measurements based on grayscale images- coupled with functional information, such as Doppler velocities (quantitative flow estimates). In clinics, the frequency used in ultrasound imaging ranges from 1 to 20 MHz, depending on the specific application and the medium depth. In cardiology, ultrasound is commonly used as an investigation tool for both the vessels and heart (Figure 1.13).

Ultrasound imaging has now become a widely used modality specially in routine check-ups as it provides images in real-time at a low-cost and without any harmful ionization. It has also the advantage of being portable and can be easily brought to the patient bedside. Drawbacks include a limited field-of-view, high image variability between clinicians, and difficulties to image structure behind bone or air.

As AAA stays often asymptomatic until it reaches a worrying stage, US routine check-up (screening) seems indicated for its diagnosis. For the specific diagnosis of AAA, US nationwide screenings have proven effective in preventing AAA related deaths in the UK and Sweden, and US screenings are in place for all men after 65 years old (Scott 2002; Wanhainen, Hultgren, and Linne 2017). Other countries such as Australia, Estonia, Poland, and the USA also have US screenings in place for specific regions and population (Jawien et al. 2014; McCaul et al. 2016; Chun et al. 2019; Reile et al. 2020). A lot of studies are still in place nowadays to find an efficient cost-effective way of targeting population for US screening. Criteria for population screening includes of course sex and age, but also smoking history, and family history of CVD (Powell 2016; Spanos, Labropoulos, and Giannoukas 2018; Watson, Gifford, and Bandyk 2020).

1.VI.B Principle

Ultrasound imaging is based on the propagation of ultrasound waves inside the medium of interest. Each medium can be considered as a set of scatterers that backscatter ultrasound after insonification. A common hypothesis is to consider the scatterers as emitting circularly in all directions.

For academic purposes let us consider a punctual source transmitting an ultrasound wave at time $t_{emission}$ in all direction. The ultrasound wave will reach the scatterer point distant of z_0 at time $t_{backscatter}$. The initial ultrasound wave continues to propagate at a lower intensity, while a part of it is being

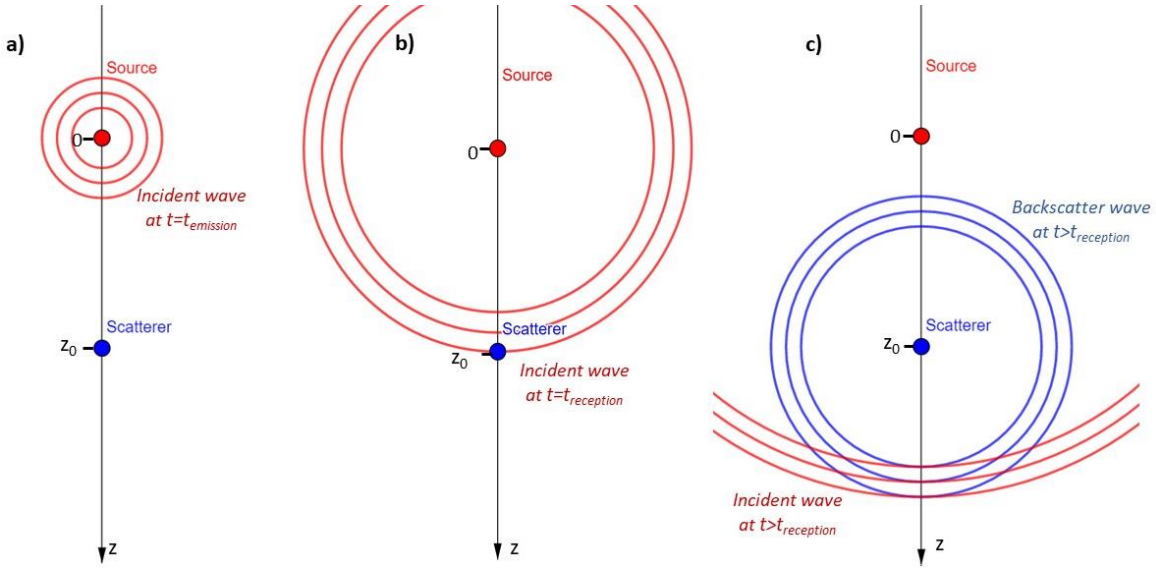

Figure 1.13: Principle of backscattering: a) incident wave when the source is emitting, b) incident wave when the scatterer is receiving and c) incident and backscattered waves after reception by the scatterer.

Table 1.VI.1: Speed of sound and attenuation values depending on the medium

Medium	Speed of sound c (m/s)	Attenuation coefficient α (dB/MHz/cm)
Water	1 480	0.002
Blood	1 575	0.15
Fat	1 450	0.6
Soft tissue	1 540	0.75
Muscle	1 585	1.5
Bone	4 080	10

backscattered by the scatterer (Figure 1.14). The backscattered wave will then reach the source at a time $t_{reception}$. The speed of sound through the medium will determine the time required for the wave to reach the scatterer and the time required for the backscattered wave to reach the source. By knowing $t_{emission}$ and $t_{reception}$, the distance z_0 can be recovered with a hypothesis on c the speed of sound. as $c = \frac{2\,z_0}{\Delta_T}$, i.e. $z_0 = \frac{c\,\Delta_T}{2}$ with $\Delta_T = t_{reception}\text{-}t_{emission}$ being the reception delay. The same principle is applied in marine acoustic by sonar. In clinics, tissues are composed of different layers with different speeds of sound (Table 1.VI.1). An average speed of sound of 1540 m/s is often considered by general consent for most medical applications. Ultrasound waves are also affected by attenuation, depending on the wave frequency. This attenuation effect can be corrected using Time Gain Compensation (TGC) if the Signal-to-Noise Ratio (SNR) is adequate.

Ultrasound images are known for having a particular pattern, called speckle, which is due to an heterogenous repartition of scatterers in the medium (Figure 1.18). Indeed, each scatterer insonified by an ultrasound wave, will emit in its turn a spherical echo wave. This echo, will then interfere with other scatterers' echoes, creating a complex wave, forming the speckle.

In clinics, probes or transducers, with more than one ultrasound source, called elements, are used to insonify the medium. The elements can convert an electrical signal to an ultrasound wave, and vice versa. The ultrasound beam pattern of a transducer can be determined by the active elements area (i.e. the elements emitting an ultrasound signal) and shape, the ultrasound wavelength, and the speed of sound in the medium. In theory, to obtain the desired waveform, the elements must have an infinitesimal size. In practice, the elements have a determined width and are separate from each other by a distance called kerf; while the width plus the kerf is the pitch (i.e. distance from two elements centers); as illustrated for a linear probe in Figure 1.16. The limited aperture and element spacing create unintended lobes that are local maxima in the ultrasound wave pattern. Ultrasound probes receive echoes from the medium consisting of raw Radio-Frequency (RF) data. (Figure 1.17).

In clinics, different types of probes are used in function of the medical application.

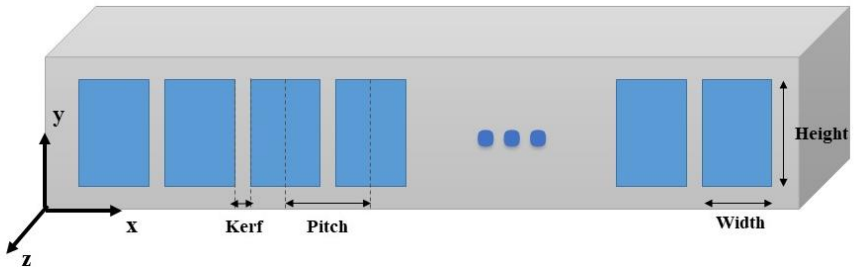

Figure 1.15: Schematic representation of a linear probe. The elements are represented in blue.

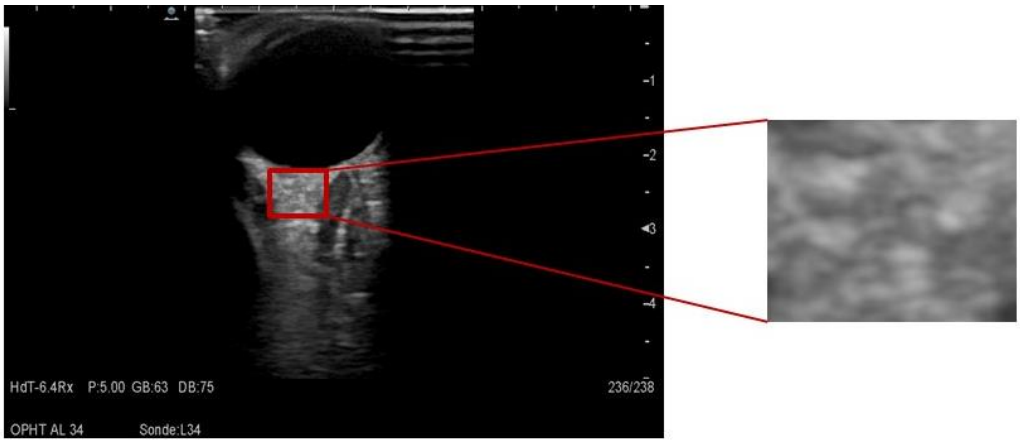

Figure 1.17: Zoom on the speckle of a conventional ultrasound image of an eye *[Courtesy of Pr. Anne Long, Hôpital Edouard Herriot, Lyon, France]*

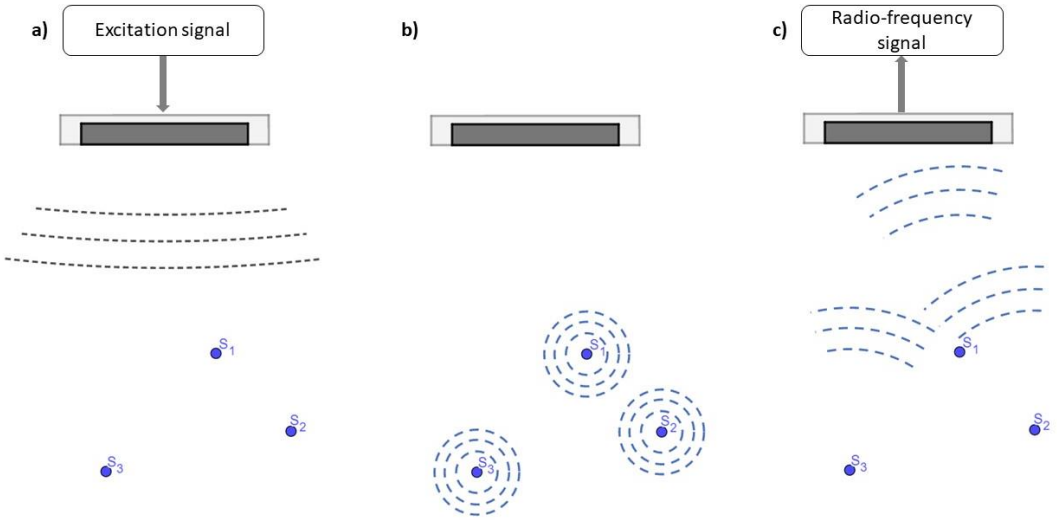

Figure 1.16: Transmission and reflection of the ultrasonic wave: a) An electrical signal excites the probe and causes an incident wave propagating through the medium. (b) upon contact with the incident wave, the scatterers backscatter a spherical wave. (c) The backscattered echoes are received by the probe and converted into a radio-frequency signal.

1.VI.C Different probes shapes

There exist different types of ultrasound probes depending on the clinical need. The central frequency and the shape of the probe alongside with elements size and position may be different. For example, a lower central frequency will increase the imaging quality at high depth as low frequency are less affected by attenuation. However, this comes at the price of image resolution. It would then make sense to use a high frequency probe to visualize the shallow tissue of the skin, and a lower one to study deep organs such as the livers. Similarly, some probes are shaped to have a large or a narrow field-of-view (respectively convex/phased array), to be inserted inside the patient's body (endocavitary and transesophageal probes), to focus the energy (therapeutic probe) etc. Photos of a linear, phased array and convex probes available at the PILOT [1]ultrasound platform are pictured in Figure 1.19.

[1] The LyonTech Multimodal and Experimental Imaging Platform, denoted PILoT, is an imaging platform that brings together MRI, ultrasound and optical modalities in Lyon, France.

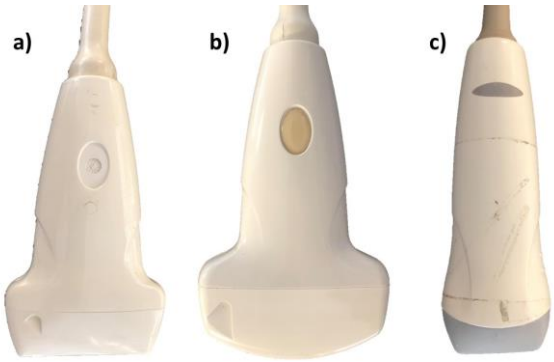

Figure 1.18: Illustration of a) linear, b) convex and c) phased array: These probes are the LA523, the C631 and the PA230, from Esaote SpA® (Italy) available on the PILoT1 platform.

Linear probes are the commonly used to study superficial tissue, such as shallow blood vessels. They typically are composed of 64 to 256 elements, with a center frequency ranging from 5 to 15 MHz. As their name indicate, the ultrasound elements are placed on a straight line.

As ultrasound are highly reflected by bones, the visualization of the heat located behind the ribs is particularly. Phased arrays have a small aperture with 64 to 128 elements placed in a narrow straight line, allowing ultrasound signals to pass between the ribs. A sector field-of-view is produced by steering the emitted ultrasound wave. Small delays in element firing allow for electronic field steering without moving the ultrasound probe.

The elements of convex probes are placed on a circle arc, producing a large sectorial field-of-view. They are primarily used for abdominal scans to image deep and large organs. For allowing a deep imaging range, low frequencies are used, typically in the range from 1 to 5 MHz. As the elements are not placed on a straight line, the RF data received by the elements are not in the cartesian coordinate system, but in the polar coordinate system of the probe as illustrated in blue in Figure 1.20. After image formation, an interpolation onto a cartesian grid is realized for visualization purpose.

1.VI.D Focused imaging

Conventional ultrasound imaging is performed by a succession of emission/reception cycles. First, an ultrasonic beam focused at a specific point inside the medium is emitted by applying different delays (and weights) to the probe elements (Figure 1.21.a). Often just a subset of elements called active elements are used in transmission. The propagation of the ensuing ultrasonic waveform follows an hourglass shape that has its minimum lateral size, corresponding to the minimum lateral resolution, at the focused depth (Figure 1.22.a). Before and after the focused point the lateral resolution increases. This technique as the advantage to concentrate the energy at a specific depth and line of interest, offering a good image quality both in terms of resolution and contrast. Afterward, the RF echoes from the focal point are received by the probe. Based on the *a posteriori* knowledge of the

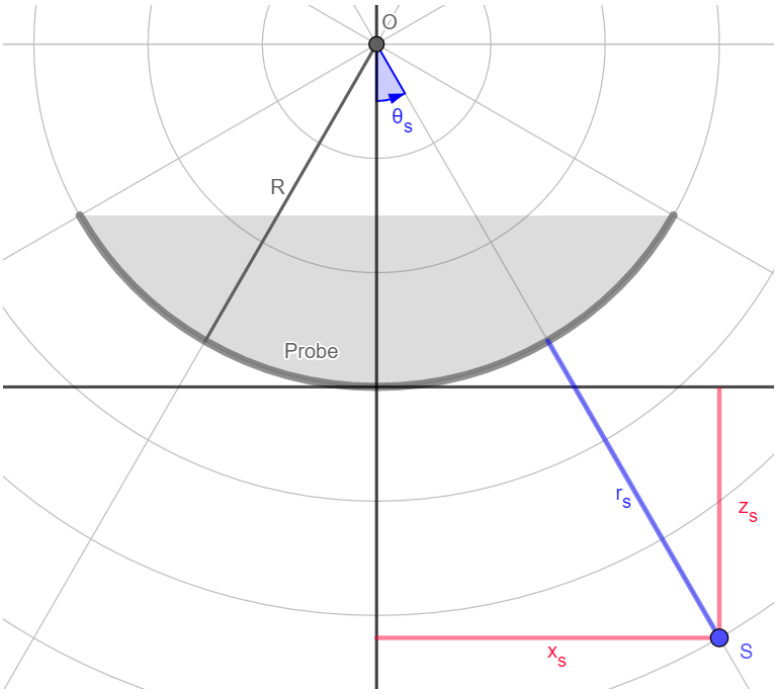

Figure 1.19: Illustration of the polar coordinates of the convex probe of origin O. A scatterer S is represented alongside its polar (r_s, θ_s) in blue and cartesian coordinates (x_s, z_s) in red.

travel times, the received signal is delayed, weighted and summed to form an RF line (Figure 1.21.b). This beamforming technique sis called “Delay-And-Sum” often abbreviated as DAS.

The medium is then fully scanned by successive sequences of transmission and reception while the focus point and the active elements are being swept along the lateral position axis. It is also possible to repeat the focalization at several depths to obtain a globally lower lateral resolution. There are two main notions linked to this succession of emission/reception cycle:

- The Pulse Repetition Frequency (PRF) represents the frequency of the emission/reception cycles. It is limited by the maximal depth of the medium of interest z_{max} as the ultrasonic wave needs to reach this depth and then travel back to the probe before the beginning of another cycle.

$$PRF = \frac{c}{2\, z_{max}} \qquad 1.1$$

- The number of ultrasound images per second is defined by the notion of Frame Per Second (FPS). In conventional imaging, the FPS can be obtained through:

$$FPS = \frac{PRF}{N_{cycle}} \qquad 1.2$$

where N_{cycle} is the number of transmission/reception cycles needed to fully form an image.

In clinics, conventional imaging, which provides a maximum frame rate of around a hundred of images per second, is typically used. With this limitation on frame rate, some highly transient and fast phenomenon are not distinguishable.

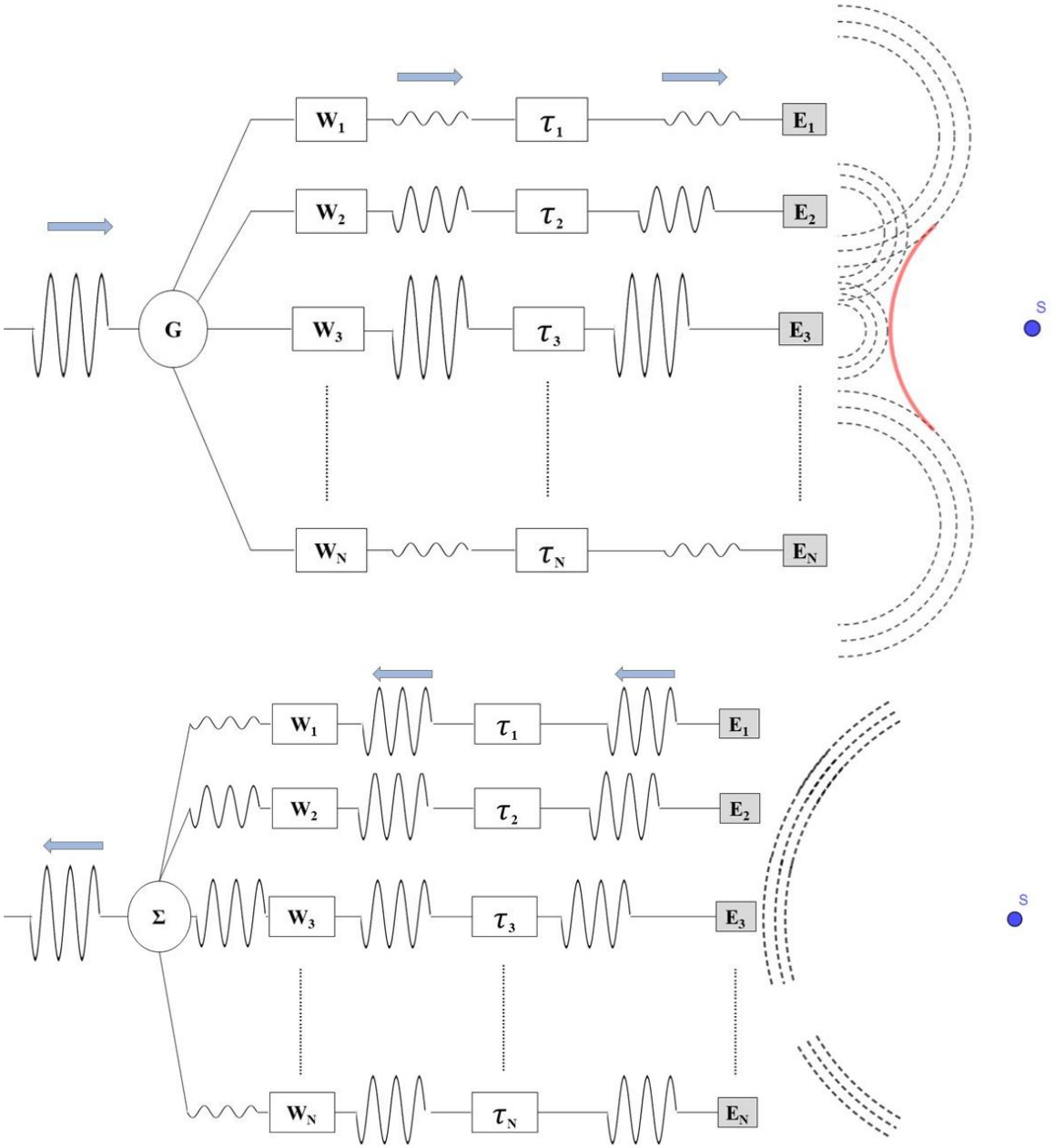

Figure 1.20: Diagram of a single RF-line delay-and-sum beamforming during a focused emission (top) and reception (bottom). The electrical signals are weighted (denoted by w_N) and delayed (denoted by τ_N) during transmission to create a specific ultrasonic waveform (represented in red). During reception, the received RF-signals are also delayed and weighed before being summated, thanks to the knowledge *a posteriori* of the flight times.

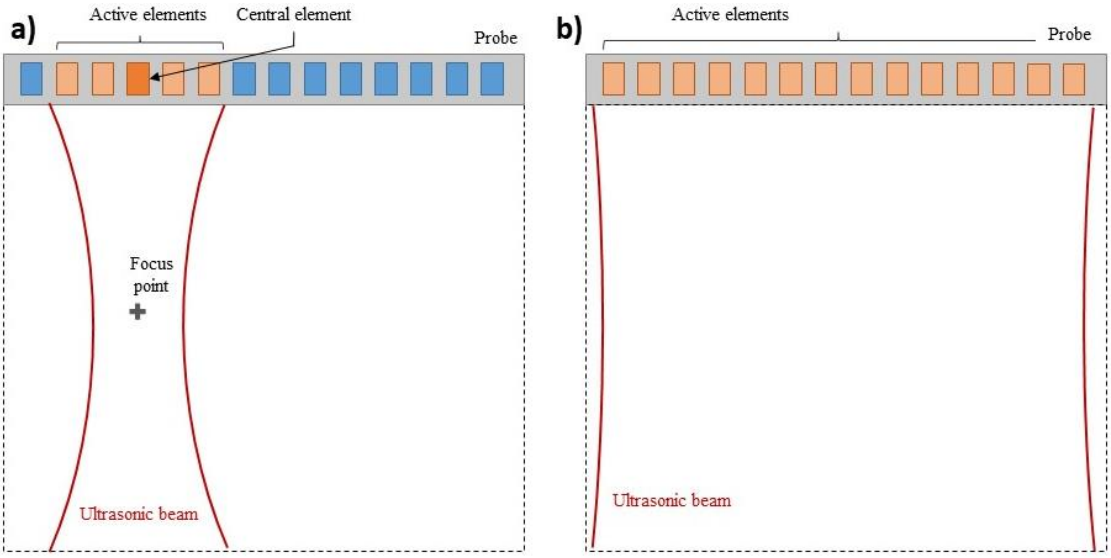

Figure 1.21: Schematic view of: (a) a focused ultrasonic beam in conventional imaging. A finite number of elements called active elements are used in transmission; (b) a plane wave ultrasonic beam in ultrafast imaging. All elements are used in transmission to create a wide field-of-view beam into the medium.

1.VI.E High frame rate imaging

When using conventional imaging, the frame rate is limited by the number of transmission/reception cycles (see Eq 1.2). To overcome this limitation, one solution consists of transmitting a wide field-of-view beam into the medium, recording the resulting backscattered echoes, and finally performing a fast beamforming. This way, one ultrasonic image is formed from one single transmission and the framerate is only limited by the maximum investigated depth (as in Eq 1.1): this is called ultrafast ultrasound imaging (Tanter and Fink 2014). The concept of ultrafast imaging dates back from the 70s with the first publication mentioning the terminology published in 1977 (Bruneel et al. 1977). However, ultrafast imaging techniques truly expanded during 2010s with computational technical upgrades making beamforming in real times of >1000 frames/s available (Tanter and Fink 2014).

A simple way to insonify broadly the medium is to apply no transmission delay on the elements. If a linear probe is used, a plane front wave will propagate through the medium, insonifying all in front of the probe (as in Figure 1.22.b). If a convex probe is used, a plane front wave is emitted in the polar coordinates of the probe (Figure 1.20). In the medium, a divergent wave that follows the geometry of the probe will propagate, insonifying a large portion of the medium.at the cost of greater energy dispersion.

As there is no transmitting focus, the quality of an ultrafast ultrasound image is not as good as in focused imaging, in terms of both resolution and contrast. To overcome this issue, compounding techniques (Montaldo et al. 2009) have been developed, allowing to recover an image quality comparable to conventional focused transmissions. Several plane or diverging waves are transmitted successively in the medium with different incident angles generating backscattered echoes containing different information. By coherently combining sub-images obtained through the beamforming of each emission's echoes, a synthetic transmitting focusing is achieved, which improves image quality.

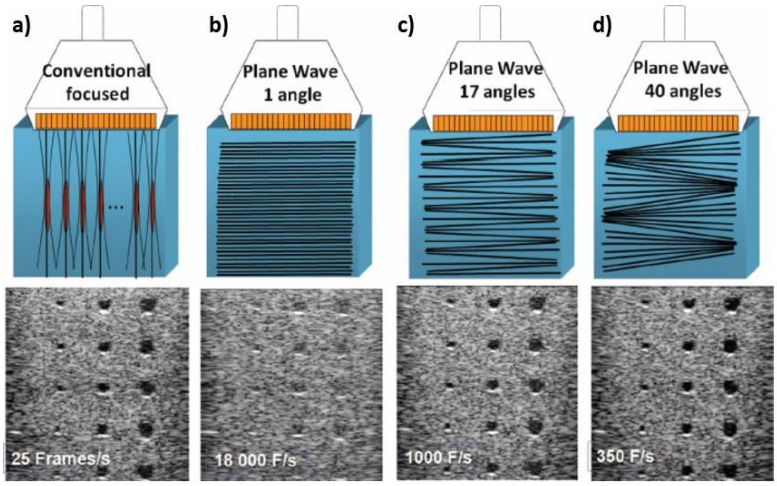

Figure 1.22: Conventional focused and ultrafast ultrasound imaging sequences for a typical medical imaging setup: (a) conventional focused imaging (≈25 Hz), (b) plane-wave imaging (≈18 kHz), (c) plane-wave compounding with 17 angles (≈1 kHz), and (d) plane-wave compounding with 40 angles (≈350 Hz). Image quality is improved with the number of sub-images compounded at the expense of the framerate. *[figure reported from (Tanter and Fink 2014)]*

One drawback of compounding methods is that the final frame rate is divided by the number of sub-images N_{frame} to be compounded (Eq 1.3): a compromise must be reached between frame rate increase and image quality (Figure 1.23).

$$FPS = \frac{PRF}{N_{frame}} \qquad 1.3$$

Compounding has been studied with linear probes (Salles, Liebgott, et al. 2014; Gasse et al. 2017) , phase arrays (Papadacci et al. 2014; Poree et al. 2016), convex probes (Kang et al. 2020) and with 2D probes (Provost et al. 2014; Salles et al. 2019). As compounding requires successive waves to be combined coherently, this approach is sensitive to high-velocity tissue motion: motion compensation can be used to decrease the influence of high-velocity tissue motion (Poree et al. 2016; Chen, D'hooge, and Luo 2018; Salles et al. 2019).

A major step in obtaining good quality images with ultrafast US is the beamforming, and several beamforming methods have been specially developed for ultrafast US. (Liebgott et al. 2016) organized a challenge at the 2016 IEEE International Ultrasonics Symposium (IUS) of Tours (France) in order to compare such beamforming algorithms on the same set of data.

Other approaches than plane/diverging waves have been proposed to increase the available framerate of conventional imaging. Synthetic transmit aperture imaging consists of emitting with only one active element while the reception is achieved with all the elements (J. A. Jensen et al. 2006). Several low-resolution images formed from each transmitted spherical waves are created. All the images are then summed up to get a high-quality image. However, the frame rate is then directly divided by the number of elements used in transmission. Lately, another high-frame rate method, multi-line transmit has been proposed (Tong et al. 2014). It consists of sending a series of several beams at the same time into the medium, permitting a higher frame rate but at the cost of cross-talks artifacts occurring between the different beams on both transmit and receive (Badescu et al. 2019).

Nowadays, the frame rate of ultrasound imaging is not limited at 100 images by second as it was with conventional imaging. Several ultrafast techniques have been proposed where the frame rate depends only on the maximal investigated depth. To compensate for the loss in image quality, compounding can be performed: the frame rate now depends on both the maximal investigated depth and the number of sub-images acquired. A framerate higher than 10 kHz can be achieve in superficial tissues.

The increased resulting frame rate makes possible to capture fast transient phenomena occurring in organic tissue.

1.VI.F Image formation

Regardless of the emission technique, once the backscattered echoes are received by the probe, there is a need for image formation to compensate for the echoes spherical propagation: this step is called beamforming. Each scatterer in the medium will be recorded by the probe as a hyperbola whose shape depends on the scatterer's position and of the speed of sound in the medium. With the knowledge *a posteriori* of the flight times, the hyperbolas laws can be recovered. The raw signal is then summed along the curve to give the image value at this point. This beamforming technique is called "delay-and-sum" often abbreviated as DAS (Figure 1.21 b). However, due to the directivity of the elements, the signal at the edge of the hyperbola fades and tends to be only noise and other scatterers contributions. Generally, only the signal from a portion of the hyperbola is considered. This aperture depends upon depth and can be fixed using the notion of f-number, denoted $F_{\#}$, with a linear probe:

$$F_{\#} = \frac{D_f}{L} \qquad 1.4$$

where L is the total width of the active aperture, and D_f is the distance to the focus; $F_{\#}$is often kept constant and its value depends on the clinical purposes of imaging.

As the received echoes are radio-frequency signals, an envelope detection (demodulation at the carrier frequency) is typically performed after beamforming for visualization purpose. A grayscale map with a log-compression to adapt the wide dynamics of the ultrasound images to the human vision capabilities is often performed. The resulting image is called a B-mode image and is almost always used in clinics (Figure 1.24).

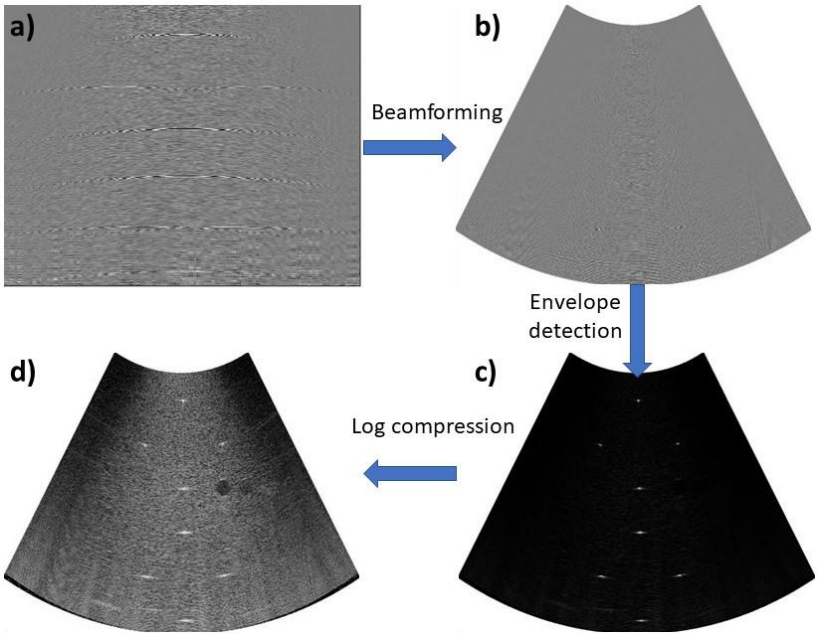

Figure 1.23: Illustration of the different steps to obtain a B-mode image: a) received echoes by a convex probe; b) RF image after beamforming; c) Envelope detection; d) B-mode image obtained after log compression

1.VII Ultrasound imaging Pathologies Markers in the AA

As abdominal disorders often stay asymptomatic for a long time, ultrasound imaging is a perfect, safe, diagnosis tool. It is used for both qualitative inspection and for quantitative measurements. This section is broken down into two subsections: wall, and flow.

1.VII.A Wall

In clinics, vascular physicians use grayscale B-mode images to evaluate different tissue characteristics. A standard tissue measurement is the evaluation of the vessel diameter, particularly useful to detect and evaluate the severity of an aneurysm (Figure 1.25). The severity of a stenosis can also be evaluated by measuring the inner diameter before, after, and in the middle of the stenosis.

As age and pathology influence the vessels walls properties, it will have an impact on tissue motion. The foremost quantitative marker with tissue motion estimation is the computation of the arterial distensibility (Hoeks et al. 1990) which is the relative radius variation during a cardiac cycle (Figure 1.26). Distensibility gives an information on arterial rigidity: a rigidified vessel tends to move less during a cardiac cycle and hence have a lower distensibility.

A more complex measurement is the estimation on the Pulse Wave Velocity often abbreviated PWV (W. W. Nichols and McDonald 1972; Benthin et al. 1991; Luo, Li, and Konofagou 2012; Huang, Guo, et

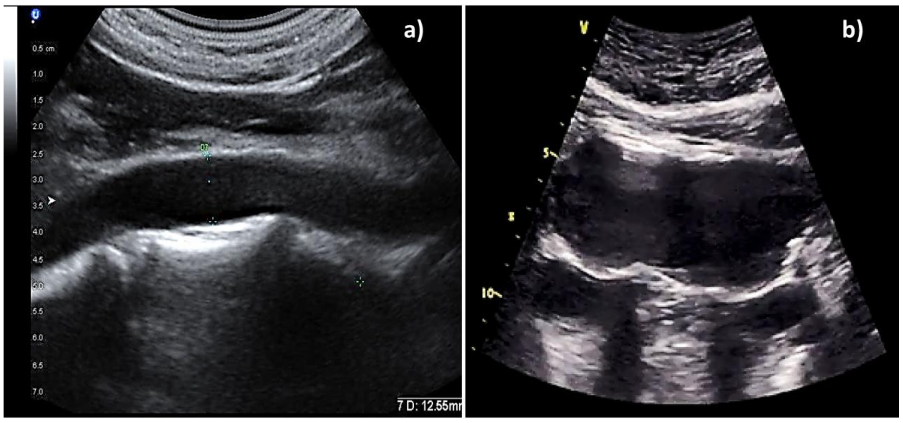

Figure 1.24: Clinical images of abdominal aortas: a) measurement of a healthy abdominal aorta diameter [*Courtesy of Pr. Anne Long, Hôpital Edouard Herriot, Lyon, France*]; b) accidental discovery of an aneurysm with an approximated diameter of 5cm [*Courtesy of Dr. Philippe Marguet, Centre Hospitalier Intercommunal de Haute-Comté, Pontarlier, France; available at https://echo-urgences.com/ on the 27/02/2020*];

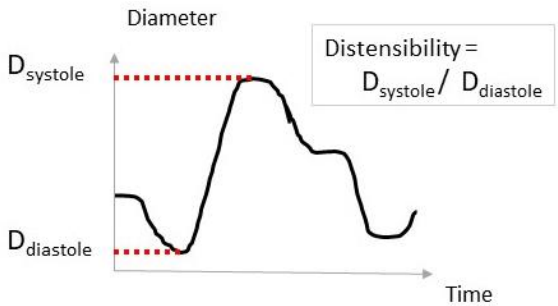

Figure 1.25: Schematic representation of an artery variation of diameter during one cardiac cycle. The maximum and minimum diameter occur during systole and diastole respectively. The distensibility can then be computed, giving information on arterial rigidity.

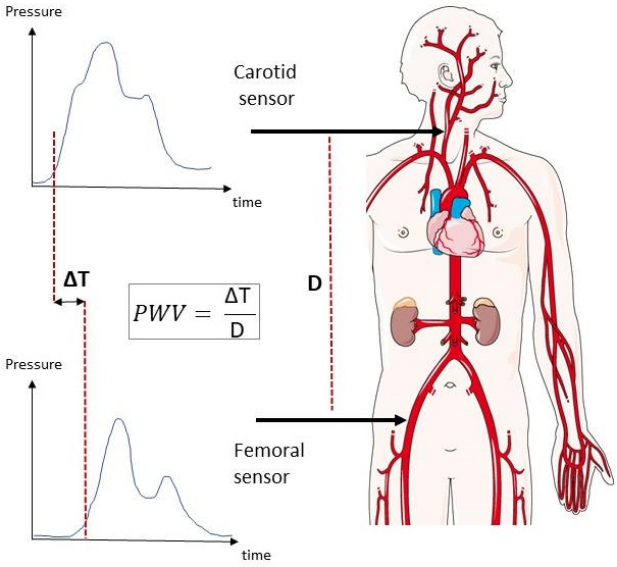

Figure 1.26: Schematic assessment of pulse wave velocity (PWV) by tonometry. Two pressures sensors are placed: one over the carotid, one over a femoral artery. By estimating the phase shift ΔT and the distance D, the PWV can be computed. *[vascular system from Servier Medical Art images]*

al. 2016; Apostolakis et al. 2017). The pulse wave is a mechanical wave propagating alongside the vessels walls and originating from the heart's valve abrupt closure. Its velocity depends upon the vessel's rigidity: the higher the speed, the more rigid the vessel is. If we consider an artery as a perfect cylinder, this relationship between velocity and rigidity can be describe using the modified Moens-Korteweg equation (Roy 1881):

$$PWV = \sqrt{\frac{E_{young}\, h_v}{2R_v\rho(1-\nu^2)}} \qquad 1.5$$

where E_{young} is the Young's modulus of the wall, h_v and R_v are the thickness and radius of the vessels respectively, and ρ and ν are the density and the Poisson's ratio. Even under the false perfect cylinder assumption and with the difficulty to correctly estimate the vessels properties, the PWV should reflect, and be an indirect measurement, of the rigidity. In clinics, to assess the PWV, one pressure sensor is placed over the carotid and one over the femoral artery. The maximum recorded acceleration in pressure corresponds to the pulse wave propagation at the sensor location. The PWV is then estimated by roughly measuring the distance from one sensor to another, and the time shift from both pressure waveforms This technique is called tonometry (Figure 1.27). There are several drawbacks for this method. First, there is a high imprecision from the rough distance measurement that is supposed to correspond to the pulse wave travel distance. Then, as the measurement is made from the carotid to the femoral artery, an average PWV is obtained for the entire body. It is of high clinical interest to obtain a more local PWV estimate, that can provide information on an artery section such as the rigidity of a plaque etc. However, the measurement of PWV by tonometry is still in good correlation with the one estimated by ultrasound (J. Vappou, Luo, and Konofagou 2010).

1.VII.B Flow

Clinicians also use qualitative and quantitative measurements on arteries flow, usually based on Doppler imaging (Nix and Johnson 1988). Such measurements can be particularly useful to detect an occlusion (i.e. no flow is passing through the vessel) or the presence of backflow. For complex geometries, for example in the presence of a plaque, color Doppler can help to detect the limit of the lumen and the actual diameter of the vessel.

Figure 1.27: Measurement of the flow in the right polpiteal artery of a healthy subject using a clinical scanner: (left) B-mode image superimposed with color Doppler, and (right) Doppler spectrum at the position of the green pointer in the image. In the spectrum, the arrows indicate the beginning of the systole (blue), the systolic peak (yellow), and the dicrotic notch (green) [*Courtesy of Pr. Anne Long, Hôpital Edouard Herriot, Lyon, France*].

For example, in Figure 1.28, the clinician uses the color Doppler for qualitative inspection. By convention, red implies that the flow is moving toward the probe whereas blue indicates a motion away from the probe. A quantitative measurement is done with Doppler spectrum at the green cursor in the B-mode image. The clinician can then visualize the value of the flow inside the vessel with for example the peak systolic velocity (yellow arrow in Figure 1.28). It is also noticeable that some backflow occurs in this case, which is normal in a healthy polpiteal artery at rest.

The high complexity of abdominal arterial flow is well known, and it can be quite challenging to estimate correctly under a large amount of abdominal fat. To overcome this issue, an esophageal probe can be placed at a thoracic depth where the esophagus and the aorta are nearby and parallel (Tortoli et al. 2002). This procedure is more complex than the use of a convex probe and is generally performed on patients under general anesthesia or in the intensive care area

Quantitative metrics depending on flow can also be extracted., such as peak systolic and end-diastolic velocities. The resistivity index, which is the ratio between those two values, is related to vascular resistance and is a marker of atherosclerosis risk (Tublin, Bude, and Platt 2003). More advanced metrics based on flow can be also estimated, such as Wall Shear Rate (WSR) and Wall Shear Stress (WSS):

$$\begin{cases} WSS = \mu WSR \\ WSR = \dfrac{\partial v}{\partial r}\Big|_{r=R} \end{cases} \quad 1.6$$

where μ is the blood viscosity, and v is flow velocity; WSR is also the spatial gradient parallel to the wall of velocity at the location of the vessel wall. The proper evaluation of the wall shear stress depends on the estimation of the actual blood viscosity. Blood is a non-Newtonian fluid i.e. its viscosity changes according to mechanical stress, making it impossible to correctly access its actual value. Nevertheless, even a rough estimation of the wall shear rate gives an information on the stress along the wall.

This stress is often considered as one indication to evaluate the risk of plaque rupture or formation (Zarins et al. 1983). Indeed, low stress has been supposed to facilitate the development of plaque while high stress after plaque development should increase the risk of inflammation and the rupture risk.

1.VIII Interest for Simultaneous Flow and Wall assessment

Wall and flow properties are inherently linked and are both influenced by the presence of cardiovascular pathologies and by age. In clinics, even if both aspects are often studied with ultrasound, they are accessed separately. As wall and flow interacts, an imaging technique assessing information from both media simultaneously could be highly relevant for pathology characterization. Indeed, such a technique could provide pathological markers from the wall and flow independently in the same heart cycle, but also wall/flow related markers.

Furthermore, the exact role of hemodynamic forces on local wall degeneration remains unclear (Leow and Tang 2018). For example, it is supposed that abdominal aorta aneurysm mainly developed in the infrarenal part of the aorta partially because of the strong backflow experienced in this portion. Nevertheless, the exact effects of this backflow remain unknown. Studying simultaneously wall and hemodynamic motions could lead to a better understanding of vascular diseases formation and artery biomechanics in general.

By providing more information, with the simultaneous measurements, we could expect better detection, more precise diagnosis, and improved monitoring of artery pathologies. However, in clinical routine, only color Doppler coupled with Doppler spectrum at a relatively low frame rate are used as advised in the guidelines and do not give any vectorial flow information.

Consequently, most of the clinical studies are based on an incomplete flow information, and ultrasound acquisitions are realized at a relatively low frame rate (maximum 100 images per second using a scan line mode) while other techniques with plane mode imaging could provide wall motion, vectorial flow, and advanced pathological markers at high frame rates.

Chapter 2: State of the art on motion estimation

This second chapter presents the standard motion estimation techniques commonly used in vascular ultrasound. We first focus on flow estimation methods. Doppler techniques, considered as the clinical golden standard, are first described. Both frequency-based and phase-based approaches are presented. Then, non-Doppler-based techniques are presented, including speckle-tracking and optical flow approaches. The specificities of approaches dedicated to wall motion estimation are then presented. After presenting the standard estimation techniques, state of the art on the specific subject of simultaneous measurement of tissue and flow motion is conducted. This state of the art includes previous works from several groups working with a linear ultrasonic probe. To the best of our knowledge, no work has been conducted on simultaneous tissue and flow motion estimation with a convex probe. This second chapter concludes with the expected bottlenecks occurring with a convex probe and the approaches selected to overcome them during this thesis.

2.I Doppler-based techniques

2.I.A Doppler effect

The Doppler effect is a change between the frequency of the transmitted wave and the received wave when there is a relative movement between the source and the target. In clinical applications, the Doppler effect is mainly used to estimate blood velocity (Hoskins 2019): an ultrasonic wave of frequency f_0 propagates inside the medium; this wave will then be backscattered by the red blood cells in motion in the vessel. The frequency of the backscattered wave is modified with respect to the incident wave by an amount proportional to the speed of the red blood cells.

The difference Δf between the transmitted frequency f_0 and the received frequency f_r is called the Doppler frequency, denoted here as f_d. This difference is positive when the flow approaches the probe and negative when the flow moves away from it.

$$f_d = \Delta f = f_r - f_0 \quad (2.1)$$

The Doppler frequency is expressed by the following relation (J. A. Jensen 1996a):

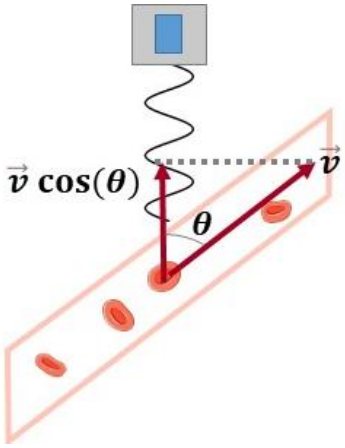

Figure 2.1: Schematic view of an application of the Doppler effect. The red blood cells have a velocity of $\vec{v}$; the Doppler frequency is proportional to $|\vec{v}|\cos(\theta)$. For visualizing purpose, only one element of the probe is represented (in blue). *[Blood cells from Servier Medical Art images]*

$$f_d = 2f_0 \frac{|\vec{v}|\, cos(\theta)}{c} \qquad 2.2$$

where $|\vec{v}|$ is the speed modulus of the red blood cells,c is the celerity of the US wave in the medium and θ is the angle between the propagation of the flow and the direction of the ultrasonic beam, commonly called the beam-to-flow angle.

The Doppler frequency or frequency shift is therefore proportional to the projection of the velocity vector on the axis of the ultrasound beam as illustrated in Figure 2.1. The beam-to-flow angle can be approximated on a B-mode image and the speed of the flow can then be recovered. The Doppler frequency is usually shifted in the audible range of frequencies (from 1 kHz to 20 kHz), which permits clinicians to both listen and watch the spectrum for diagnostics (Figure 1.28).

It appears clearly from Eq 2.2, that if the blood vessel is perfectly perpendicular to the ultrasound beam (i.e., θ=90°), no Doppler shift is present, and the blood velocity cannot be recovered.

The Doppler methods are declined in several approaches in the frequency domain or the time domain.

2.I.B Time shift approaches

Time shift approaches methods seek to estimate the temporal shift between two consecutive signals backscattered by the moving target of interest. This shift denoted Δt depends on the pulse repetition time T_{PRF} and can be expressed as (J. A. Jensen 1996a):

$$\Delta t = \frac{2\,|\vec{v}|\, cos(\theta)}{c}\, T_{PRF} \qquad 2.3$$

This time shift can be estimated as the peak of cross-correlation functions between consecutive signals (Bonnefous and Pesqué 1986). Different functions of similarities can be used beside the cross-correlation function, such as the normalize covariance, the sum of absolute differences or the sum of squared differences. (Viola and Walker 2003) compared these different similarities functions to the cross-correlation function normalized and not normalized. They conclude that the sum of squared differences presented a good compromise in terms of performance and computational complexity.

Several parameters influence time shift estimation techniques, notably the size of the investigation windows and the width of the US beam. If the velocities are exactly the same in all the Region Of Interest (ROI), the estimation accuracy will be better when the ultrasound beam is narrow and the window size is large. However, usually different velocities are present in a vessel as the flow often

assumes a parabolic shape. In this case, a large velocity distribution within the investigation window will greatly reduce the estimation accuracy. A compromise must then be found between these two conclusions (Foster, Embree, and O'Brien 1990).

2.I.C Frequency-based methods

Frequency-based approaches are focused on estimating the frequency shift occurring by Doppler effect when a moving target is insonified. In the Fourier domain, the received signal can be seen as a frequency-shifted version of the transmitted signal. If we consider the US transmission as monochromatic and if frequency changes due to propagation inside the medium are not considered, the frequency-shift should be due solely to the moving targets.

The challenge of these estimators is to provide the most local measure of velocity possible. To do this, these methods estimate an average frequency within a region as small as possible. The use of narrow band emission signals tends to facilitate the estimation in the frequency domain. However, the spatial resolution in the axial direction suffers from the decrease length of the US pulse. This remark highlights the compromise to be found between the spatial resolution of the US image and that of the estimated speeds.

Several works focused on improving the estimation of the mean frequency. Maximum likelihood (Azimi and Kak 1985; Ferrara and Algazi 1991) and parametric spectral analysis approaches (Kouame et al. 2003; Vaitkus and Cobbold 1998) have been proposed.

Each blood cells have a unique velocity and direction, yielding to a specific frequency shift. Hence, the frequency of the US waves backscattered by a blood vessel represents a composite of the heterogenous Doppler shifts. As explained, these Doppler frequencies can be averaged spatially to obtain a mean Doppler frequency that can be converted as an instantaneous velocity for the ROI averaged using the Doppler equation (Eq. 2.2). It is also possible to use Fourier analysis (fast Fourier transformations) to average the different Doppler frequencies over a circumscribed time period. After converting frequencies to velocities using the Doppler equation, the spectrum of all average velocities can be displayed. This is known as a Doppler spectrum, tracing the distribution of velocities inside the ROI during time.

2.I.D Phase-based methods

Phase-based approaches are focused on estimating the phase difference $\Delta\phi$ in the signal between successive insonifications of the medium. Phase information and the Doppler frequency are linked by the following equation with the phase shift expressed in radian (Buck et al. 2000):

$$\frac{\Delta\phi}{2\pi\, T_{PRF}} = f_d = 2f_0 \frac{|\vec{v}|\, cos(\theta)}{c} \qquad 2.4$$

If the target velocity causes an absolute phase difference greater than π, an overlap phenomenon appears, and the target velocity is not correctly estimated. Increasing the PRF might solve this problem. Nevertheless, the PRF is inherently limited by the duration of the ultrasound wave's round trip.

(Kasai et al. 1985) were the first to provide a direct access to the phase-shift and their method is still widely used nowadays. First, the received sampled signal is demodulated at the transmit frequency and can be written as a complex signal s:

$$s(t) = I(t) + jQ(t) \qquad 2.5$$

with I and Q are respectively the in-phase and quadrature components and j is the imaginary number.

The mean complex autocorrelation function, denoted $\hat{R}$, can be expressed as:

$$\hat{R}(\tau) = \mathbb{E}\big(s^*(t)\, s(t+\tau)\big) \qquad 2.6$$

where τ is the lag for estimation, * is the complex conjugate notation, and $\mathbb{E}$ is the expected operator.

The phase can then be extracted using:

$$\Delta\hat{\phi}(\tau) = arctan\left(\frac{\Im\{\hat{R}(\tau)\}}{\Re\{\hat{R}(\tau)\}}\right) \qquad 2.7$$

where $\Delta\hat{\phi}$ is the estimated phase shift; $\Im$ and $\Re$ are respectively the imaginary and real functions, and $arctan$ is the inverse tangent function.
Finally, velocity can be recovered using Eq. 2.4. In practice, spatial filtering is performed onto the autocorrelation estimates before phase extraction to reduce variance.

The presented phase shift estimation technique has been modified by Loupas *et al.* (Loupas, Powers, and Gill 1995), who use a 2D autocorrelation function. They manage to compensate for carrier frequency shifts that can occur locally due to variations in the medium, attenuation and artifacts.

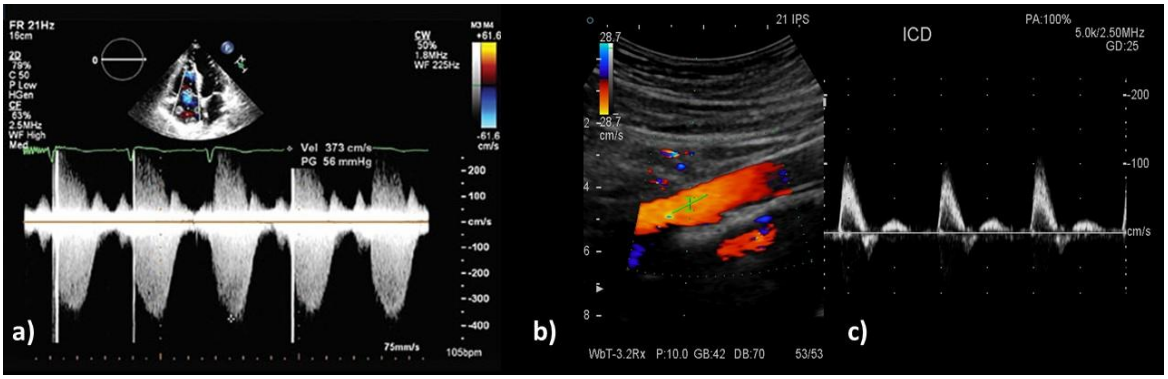

Figure 2.3: a) Continuous wave Doppler spectrum of the heart. A B-mode image is displayed on top of the spectrum to help the clinician positioning the Doppler line (dotted white) where the spectrum is computed. No information on depth is obtained and the velocities extracted correspond to the velocities alongside all the Doppler line.
b)-c) Color Flow Mapping and spectral Doppler of a healthy right internal carotid. In b), a B-mode image is superimposed over the color flow mapping. The green cursor indicates the sample volume for the Doppler spectrum and the green line represents the flow-to-beam angle chosen by the clinician. In c), the Doppler spectrum contains information on the frequency shift and hence, on the flow speed, over time. *[Courtesy of Pr. Anne Long, Hôpital Edouard Herriot, Lyon, France]*

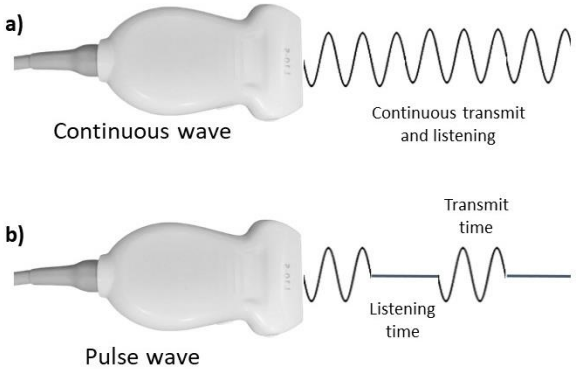

Figure 2.2: Schematic view of a) continuous wave Doppler where the transmission and reception are continuously happening and of b) pulse wave Doppler where an ultrasound pulse is emitted followed by a listening time to record the echoes from a specific depth.

On clinical scanners, color Doppler images (also called Color Flow Mapping) are often obtained through phase-based estimation techniques. Doppler estimates can be assessed at different pixels of the sequence and at different times. In each volume sample, different blood cells with unique direction and velocity contribute to the backscattered signals with their relative phase shift. By using a correlation function, the mean phase shift of each volume sample can be recovered and converted to their corresponding velocity using the Doppler equation (Eq. 2.2). These estimates constitute a 2D-axial velocity map and are then superimposed on the B-mode imagery to build a color Doppler as displayed in Figure 1.28 and Figure 2.3.

2.I.E Current clinical use

In the current clinical practice, Doppler methods are considered as golden standards mainly in the form of continuous wave Doppler, pulse wave Doppler, color Doppler and the Doppler spectrum.

Continuous Wave (CW) Doppler was first developed to detect heart wall motions (Satomura 1957) and flow patterns in peripheral arteries (Satomura 1959). One element is continuously emitting and another one is continuously receiving. The CW system allows to estimate all the velocities along the US beam without any information on position. The Doppler shift is estimated along the US beam, which only allows a projection of the true velocity to be computed as illustrated in Figure 2.1.

Pulsed Wave (PW) Doppler system developed by Wells (Wells 1969) and Baker (Baker 1970), are still sensible to the beam-to-flow angle but can extract the flow velocity at one specific depth. Two US elements are used, one in transmission will emit a short pulse and after a pause corresponding to the US wave round trip, the echoed signals are recorded. The emitting and pausing times correspond to the Pulse Repetition Frequency (PRF) of the system. The maximum Doppler shift which can be sampled is given by the Nyquist limit:

$$Nyquit_{lim} = {}^{PRF}/_{2} \qquad 2.8$$

Hence a maximum velocity v_{max} can be measured before aliasing occurs:

$$v_{max} = \frac{PRF\ c}{4 f_0\ cos(\theta)} \qquad 2.9$$

In order to be able to access higher velocity one may want to:

- increase the PRF. The PRF being limited by the distance of the sample volume, higher velocity can be estimated at shallow depth i.e., in superficial tissues.
- decrease the frequency f_0. This increases the maximum velocity detectable, offers higher penetration properties but comes at this expense of the spatial resolution.
- adjust the beam-to-flow angle θ. This can be done by changing the probe's position or by electronically tilted the US beam.

A schematic comparison of CW and PW Doppler emission schemes is displayed in Figure 2.2

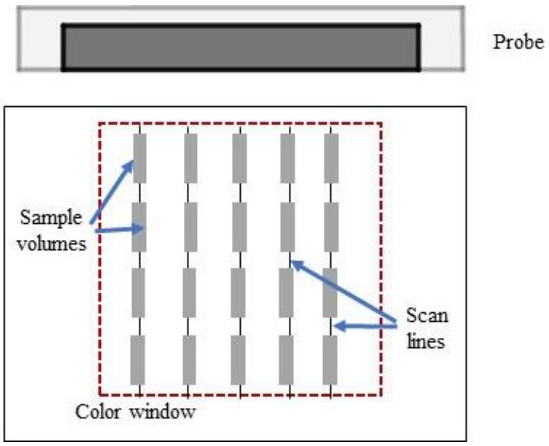

Figure 2.4: Doppler color flow mapping. Multigated sampling of multiple scan lines sweeping across an interrogated color window.

Pulsed wave systems yield velocity estimate at a single spatial location. This spatial limit was lifted by Kasai *et al.* who developed Doppler Color Flow Mapping (CFM) or color Doppler (Kasai et al. 1985). CFM obtains Doppler velocity estimates on a volume by subdividing it into several sample volumes at different depth alongside a swept scan line. First, short pulses of ultrasound are being emitted alongside the first scan line position. The backscattered echoes are then received during the listening time between each pulse. These echoes can be allocated to a range-gated sample depending on their origin's depth using their round time trip. Each scan line is repeatedly sampled using multiple pulses. The signals from the identical range gates are collected to obtain mean Doppler shifts by use of correlation function, which are averaged for each sample volume. The number of pulses per scan line is called the ensemble length. Once sampling of a scan line is completed, the interrogating scan line is swept and then processed in the same manner (Figure 2.4).

Color Doppler represents a mean velocity in each sampling volume, whereas Doppler spectrum traces the velocity distribution along time in one sampling volume chosen by the clinician. All the contributions of the different blood cells are displayed using Fourier analysis (fast Fourier transformations) to average the different Doppler frequencies over a circumscribed time period.

CW, PW Doppler, Doppler spectrum and CFM medical images are displayed in Figure 2.3

2.I.F Limits of Doppler approaches

While widely used in routine clinical practice, Doppler methods suffer from some limitations. The main one is that Doppler method is one-dimensional as the velocity can only be measured in the direction of the US beam. To estimate the velocities vectors, an assumption on the direction of the flow must be made. It is common to assume that the flow is parallel to the vessel axis, leading to the Doppler equation (Eq. 2.2) where the notion of beam-to-flow angle appears. This assumption is not always true, especially when complex flow patterns occur, leading to inaccurate flow estimations. The beam-to-flow angle is often manually fixed by the clinician as illustrated by the green line in Figure 2.3. In addition to being imprecise, this increases the variability of measurements both between different clinicians and between two acquisitions (Bolondi, Gaiani, and Barbara 1991). Furthermore, in the case of beam-to-flow angles too close to 90◦, the projection on the speed ultrasound axis is then very faint and the accuracy of the estimation is greatly reduced. It is usually considered that the beam-to-flow angle must be less than 60◦ to have a reliable estimate (Stewart 2001).

Cross-beam methods have been proposed to tackle the beam-to-flow angle ambiguity. The flow vector is obtained by combining Doppler measurements from multiple independent US beams. This

may be accomplished either using several transducers with known position between each other or separate elements of the same transducer. The first cross-beam design consisted of two single-element transducer placed at a 90°angle of each other (Fahrbach 1970). The two Doppler equations obtained with this design provide two independent equations for two unknowns and both the velocity and the real flow direction can be recovered. The difficulty of using two probes and placing them at a known exact angle can be overcome by steering several US beams with one transducer. For example, (Tamura, Cobbold, and Johnston 1991) took advantage of the three steering directions (right, central and left) commonly available on Doppler scanners. Three images of the flow field could be obtained, and the resultant velocity can be recovered wherever at least two images overlapped. The flow is assumed to be constant over three transmissions as the three images used for recovering the velocity are not obtained simultaneously.

A second limitation of Doppler techniques is due to the duplex application of B-mode image with color Doppler. For better Doppler estimation, the accuracy is increased when narrowband signals are used in emission. On the contrary, B-mode image sees its spatial resolution increased using broadband signals. Therefore, there is a compromise to be made between B-mode image resolution and Doppler estimation accuracy.

Doppler approaches tend to introduce a positive bias in the estimated velocities, i.e. the velocities tend to be overestimated. This can be explained through spectral broadening (Tortoli et al. 2015).

2.II Estimation of the optical flow

When we try to estimate the motion, we distinguish two entities: the 2D motion field of 2D motion and the apparent motion or Optical Flow (OF). The 2D motion field is defined as the projection, in the image plane, of the real 3D motion. This 2D motion field then translates the motion in the imaging plane as well as the motion out of the projected plane. On the contrary, optical flow corresponds to the velocity field measured from the spatiotemporal variations of the US image intensity. We thus have access, from the 2D US images to apparent motion information which translates, in a more or less faithful manner, the real 3D motion. The 2D motion field and the optical flow can differ, causing inaccuracy in motion estimation algorithms (Dufaux and Moscheni 1995). An easy example to understand how the 2D motion field and the optical flow can differ is the case of the barber's pole, where the 2D motion field moves laterally and the optical flow moves axially (Figure 2.5).

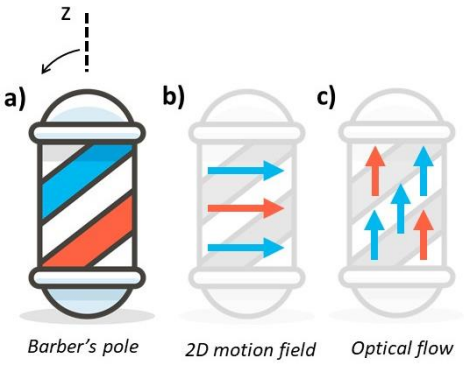

Figure 2.5: Example of the barber's pole illustrating the difference between the 2D motion field and the perceived optical flow: (a)The barber's pole rotates along the z-axis; (b) the 2D motion field is lateral while (c) the optical flow is axial. *[Barber's pole from the Streamline Emoji project]*

Approaches aiming at estimating the optical flow make the assumption of brightness constraint: the pixels gray levels are considered constant over time and motion. Different optical flow algorithms estimates the optical flow assuming different additional conditions. In US motion estimation, the two main approaches based on the optical flow are speckle tracking and differential methods.

2.II.A Speckle tracking approaches

Block-Matching (BM) approaches track the location of macroblocks in video sequences. They have been applied to ultrasound imaging, where they are known as speckle tracking (Bohs and Trahey 1991; F. Yeung et al. 1998). These methods are based on pixels gray levels, with the goal of estimating the motion of a Region Of Interest (ROI) by finding the most similar candidate in the successive image's search window (Figure 2.6). Block matching approaches make two main hypotheses:

- All the pixels of a ROI have the same motion,
- The pixels gray levels do not vary with time (brightness constraint).

Initially, Particle Imaging Velocimetry (PIV) is an optical method of flow visualization that originated from laser speckle velocimetry (Willert and Gharib 1991). This technique has been extended to ultrasound by Trahey *et al*. (Trahey, Allison, and Ramm 1987; Trahey, Hubbard, and Ramm 1988) for velocity vector imaging of the blood flow. Contrast agent can be injected into the patient blood circulation to increase the signal-to-noise ratio of blood imaging: this is called echo-PIV (Kim, Hertzberg, and Shandas 2004; Perrot and Garcia 2018).

Nowadays, most of the speckle tracking algorithms use, as a similarity measure, a Fast Fourier Transform (FFT) based cross-correlation (Garcia, Lantelme, and Saloux 2018; Raffel et al. 2018). If we consider w_1 and w_2 two consecutive ROI windows and their respective 2D-Fourier transforms W_1 and W_2, the FFT-based Normalized Cross-Correlation (NCC) can be written as follows:

$$NCC = \mathcal{F}^{-1}\left\{\frac{W_1 W_2^*}{|W_1 W_2^*|}\right\} \qquad 2.10$$

where, $\mathcal{F}^{-1}$ represents the inverse Fourier transform, * is the conjugate notation and $|\cdot|$ is the absolute value.

The relative displacements are estimated by the position of the NCC peak indicating that the speckle in w_1 is most similar to the speckle in w_2 at the consecutive frame.

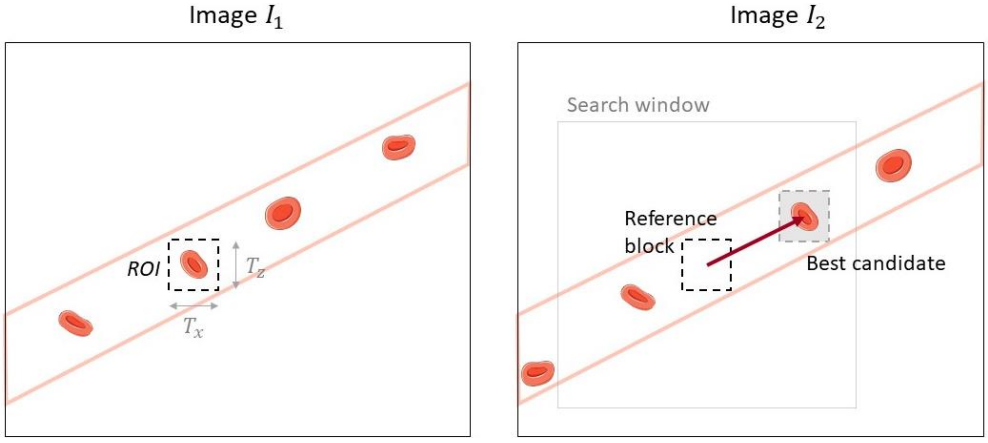

Figure 2.6: General principle of block-matching approaches. A region-of-interest of size $T_x \cdot T_z$ is selected in image I_1 as a reference block. In image I_2, the most similar block in a search window is selected to be the best candidate and to estimate the motion vector. *[Blood cells from Servier Medical Art images]*

In case of large displacements, a multiscale coarse-to-fine approach can be used to refine the estimates: the displacements are iteratively refined by decreasing the size of the ROI windows (Fai Yeung, Levinson, and Parker 1998).

2.II.B Speckle tracking limitation

Block-Matching methods estimate a displacement in pixel. To obtain subpixel estimates, the peak of the cross-correlation can be interpolated using a Gaussian or a parabolic 2D fitting (Raffel et al. 2018). This step further increases the computation time.

False peak detections, where the similarity function is offset from its true position, can also occur. They are often due to sampling issues, and Walker *et al.* tacked this problem in (Walker and Trahey 1994).

Another limit is inherent to the second hypothesis: the assumption of a uniform displacement within each ROI. In practice, this is often a false assumption particularly in blood flow estimation. For example, the speed may be parabolic (laminar flow) and therefore different in each pixel. Deformable blocks can be used as ROI to overcome this problem. These methods, called deformable block matching or generalized block matching (Seferidis 1994), are based on geometrical transformations that are more complex than simple translations. (F. Yeung et al. 1998). This further increases the computational complexity.

Echo-PIV is limited by its need for intravenous administration of microbubbles. Although the introduction of microbubbles has shown no major side effect (Quaia 2007), this procedure is time and staff consuming and thus cannot be recommended in routine clinical practice. (Fadnes et al. 2014) introduced a contrast-free procedure to track the native speckles of blood.

An intrinsic limitation of speckle tracking approaches is the presence of speckle decorrelation leading to inaccurate tracking results. This decorrelation of speckle is mainly due to spatial and temporal velocity changes, non-laminar flow and out-of-plane motions (Friemel et al. 1998). Speckle decorrelation from frame to frame is reduced when ultrafast imaging techniques are used compared to conventional imaging scheme. There is a compromise to be made between a high framerate decreasing the speckle decorrelation effect and US image quality needed for accurate speckle tracking.

2.II.C Differential approaches

Differential approaches aimed to estimate the optical flow using derivates. They were first used in ultrasound in the late 80s and mid 90s (Baraldi et al. 1996; Mailloux et al. 1989), and has been proven to be robust and reliable for *in vivo* applications (Mailloux et al. 1989; Suhling et al. 2005).

Optical flow assumes that the brightness of an object is constant over time even in motion. This is known as the brightness constraint that can be written as:

$$I(x + \Delta x, z + \Delta z, t + \Delta t) = I(x, z, t) \qquad 2.11$$

where I is the brightness of the pixel, and Δx and Δz are the displacements of the pixel during a time Δt.

Differential approaches, contrary to speckle tracking, assume that the displacement is small. Eq 2.11 can be developed with Taylor series:

$$I(x + \Delta x, z + \Delta z, t + \Delta t) = I(x, z, t) + \frac{\partial I}{\partial x}\Delta x + \frac{\partial I}{\partial z}\Delta z + \frac{\partial I}{\partial t}\Delta t + \sigma(\Delta^2) \qquad 2.12$$

where $\sigma(\Delta^2)$ are higher order terms that can be neglected.

From Eq 2.12, the following equation is deduced:

$$\frac{\partial I}{\partial x}\Delta x + \frac{\partial I}{\partial z}\Delta \mathrm{z} + \frac{\partial I}{\partial t}\Delta \mathrm{t} = 0 \qquad 2.13$$

Which can be written as

$$\nabla_{xz} I\ v = -\frac{\partial I}{\partial t}\Delta \mathrm{t} \qquad 2.14$$

where ∇_{xz} is the spatial gradient, v is the velocity components, and $\frac{\partial I}{\partial t}$ is the temporal gradient.

Eq 2.14 highlights the fact that the problem is ill-posed since there are two unknowns (v_x and v_z) for one equation. Therefore, to obtain a solution, a regularization constraint must be considered. Two main constraints are used:

- The global method of Horn and Schunck (Horn and Schunck 1981) which proposes to add a smoothing term to constrain the estimated velocity field.
- The local method of Lucas and Kanade (Lucas and Kanade 1981) which proposes to hypothesize a constant velocity over a neighborhood.

The fundamental difference between differential methods and speckle tracking is the adoption of the Eulerian paradigm (i.e., motion is evaluated through a static window) instead of the Lagrangian scheme (i.e., motion is evaluated by dynamically following a target). Complex motions involving rotations and deformations are usually better captured via OF-based approaches than BM (Hein and O'Brien 1993).

2.II.D Optical flow limitation

Optical flow approaches have the disadvantage of introducing a blurring effect at the edges of the image. This effect, due to the regularization constraint used, introduces an estimation error on the region studied.

The second limitation inherent in optical flow is the inability to estimate large displacements due to the hypothesis of small displacements in Eq 2.12**Error! Reference source not found.**. The most s ignificant measurable displacement with good accuracy is often less than the pixel size in ultrasound imaging. To overcome this issue, an iterative refinement can be used where the resolution of the image is reduced to have a small displacement compared to the pixel size; the process is repeated with a thinner resolution until convergence or until the original resolution is reached. Another more used option is to combined speckle tracking methods and differential approaches (Giachetti 2000): speckle tracking is used for large displacements estimation and differential approaches for small displacements.

As for speckle tracking, the presence of speckle decorrelation leads to inaccurate tracking results. This decorrelation of speckle is mainly due to spatial and temporal velocity changes, non-laminar flow and out-of-plane motions (Friemel et al. 1998).

2.III Transverse oscillations

Methods that estimate the motion from US images are obviously dependent on the quality of these images and, more generally, on the drawback intrinsic with the use of ultrasound. US images are highly anisotropic. Indeed, the radio-frequency (RF) images are oscillating in the US beam direction because

of the impulse response of the transducers' elements. On the contrary, no oscillation is present perpendicular to the US beam, and motion occurring in that direction can thus be quite challenging to estimate. Transverse Oscillation (TO) methods tackle this problem inherent to the US modality by creating a 2D oscillation pattern in US images. As their name suggest, the goal is to introduce an oscillation in the transverse direction. Motion can then be estimated in 2D using phase-based algorithms.

2.III.A Transverse oscillation principle

Transverse oscillation approaches were first developed at the end of 1990s (J. A. Jensen and Munk 1998; Anderson 1998). The idea is to modify the aperture of the probe in transmit or in receive to create the 2D pattern. This 2D pattern is created by interference principle and can be explained by considering two finite plane waves sent by a transducer as represented in Figure 2.7a. These interferences can be obtained either with one transducer using two sub-apertures or with two distinct transducers. By taking a closer look at the 2D pattern (Figure 2.7b), we can extract the new axial and lateral wavelengths. Indeed, by trigonometrical relationships, we can express the axial wavelength as:

$$\lambda_z = \frac{\lambda}{\cos(\theta)} \tag{2.15}$$

where λ_z is the axial wavelength, λ is the ultrasound wavelength, and θ the angle of the transmit plane waves.

The lateral wavelength λ_x can be express as:

$$\lambda_x = \frac{\lambda_z}{\tan(\theta)} \tag{2.16}$$

The two wavelengths can finally be written as:

$$\begin{cases} \lambda_z = {}^{\lambda}/_{\cos(\theta)} \\ \lambda_x = {}^{\lambda}/_{\sin(\theta)} \end{cases} \tag{2.17}$$

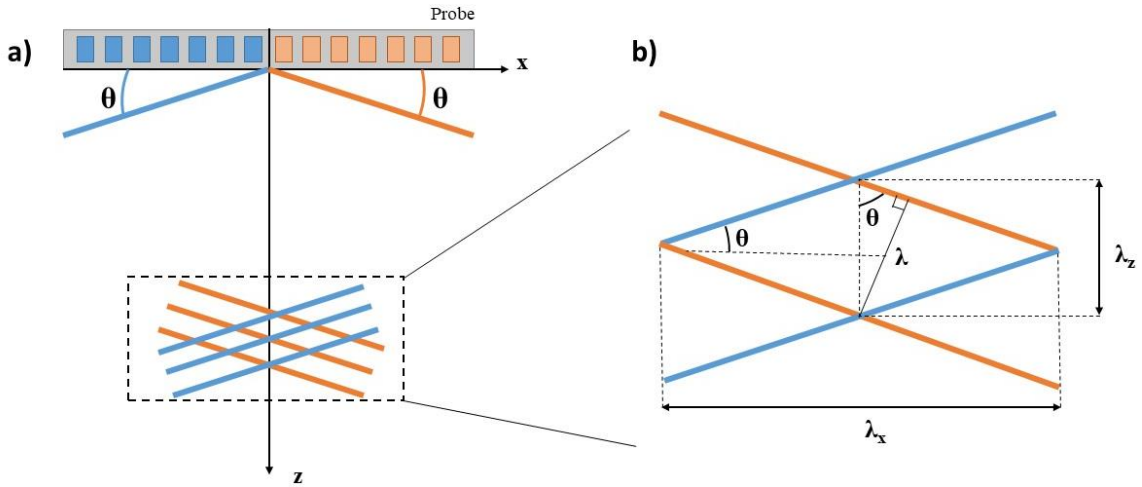

Figure 2.7: a) Crossing of two finite plane waves angulated by θ. When the two plane waves cross each other, they create a 2D oscillation pattern by interference. b) close-up of the 2D oscillation pattern: the final axial and lateral wavelengths are both different from the ultrasound wavelength *[figure adapted from (J. A. Jensen and Munk 1998)]*

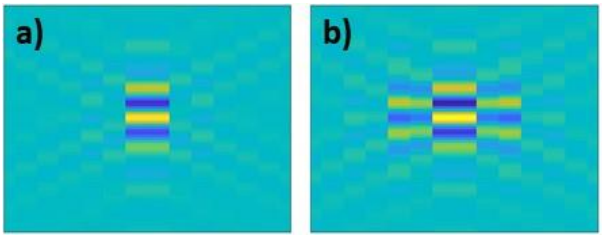

Figure 2.8: Point spread function without a) and with b) transverse oscillation.

This crossing of two finite plane waves is behind the concept of TO. In practice, such perfect plane waves cannot be transmitted by a transducer, but this illustration helps to understand the concept of transverse oscillation.

2.III.B Transverse oscillation by apodization

To introduce TO in an ultrasound image, the Point Spread Function (PSF) of the system needs to present a 2D oscillation pattern (Figure 2.8.). The PSF can be decomposed into the axial and lateral PSF (Lockwood et al. 1996):

$$h(x,z) = h_x(x)\, h_z(z) \tag{2.18}$$

where $h(x,z)$ is the 2D PSF, h_x is the lateral PSF, and h_z the axial PSF.

Supposing the ultrasound transmission as monochromatic, the Fraunhofer assumption can be applied at the focus point (Steward 2004). The Fraunhofer assumption states that the lateral PSF can be approximated as the Fourier transform of the aperture function, which can be written as:

$$h_x(x) = \mathcal{F}\left\{w_{ap}\left(\frac{x}{\lambda_x z_f}\right)\right\} \tag{2.19}$$

where $\mathcal{F}$ is the Fourier transform, w_{ap} is the aperture at the focus depth z_f.

The pulse-echo field of an ultrasound system can be described as the product of two separate fields: the transmit field and the receive field (Szabo 2004). The transmit field depends on the focus depth and on the transmit apodization. The receive field, contrary to the transmit field, can be dynamically adjusted, by adjusting the receive focus and apodization. This flexibility is used by TO approaches to introduce lateral oscillation with a constant frequency over the entire ultrasound image.

Gaussian signal possesses an interesting signal processing property: its Fourier transform is also a Gaussian function. Hence, the field from a Gaussian apodised aperture maintains a Gaussian shape with decreasing amplitude and increasing main lobe width as the depth increases. Based on this property, the receive apodization function is chosen to be Gaussian (Figure 2.10).

Oscillation should be present in the lateral PSF i.e., in the transverse direction, and can be expressed as:

$$h_x(x) = g(x)\cos\left(2\pi\frac{x}{\lambda_x}\right) \tag{2.20}$$

where $g(x)$ is a Gaussian function corresponding to the modulation of the envelope:

$$g(x) = exp\left(\frac{-x^2}{2\sigma_x^2}\right) \tag{2.21}$$

where σ_x is the standard deviation of the Gaussian function.

The corresponding aperture is then expressed as:

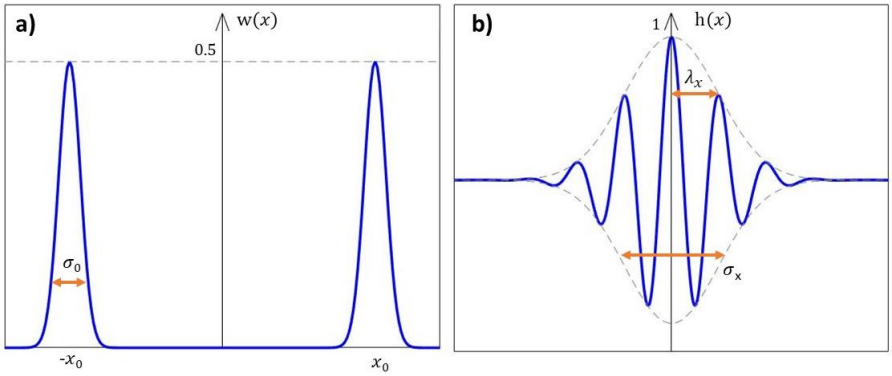

Figure 2.10: Formation of transverse oscillation by apodization: a) $w(x)$ is the specific weighting function applied to each element of the probe and, b) $h(x)$ is the lateral profile of the point spread function containing the transverse oscillation. According to the Fraunhofer approximation $h(x)$ is the Fourier transform of $w(x)$, x being the lateral position of the probe elements.

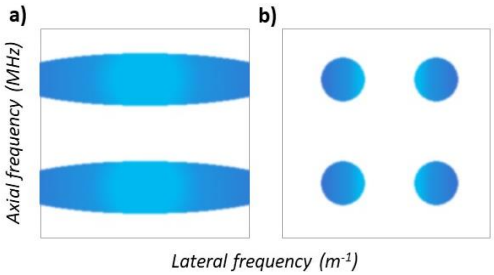

Figure 2.9: Schematic introduction of transverse oscillation in the Fourier domain: (a) f-k spectrum of a B-mode US image without TO; (b) f-k spectrum of a B-mode US image with TO

$$w(x) = \frac{1}{2} exp\left(\frac{-x^2}{2\sigma_0^2}\right) \circledast \left(\delta(x - x_0) + \delta(x + x_0)\right) \qquad 2.22$$

where σ_0 is the standard deviation of the Gaussian function, and x_0 the lateral position of the Gaussian peaks.

The parameters of the aperture are related to those of the PSF:

$$\begin{cases} x_0 = z\dfrac{\lambda_z}{\lambda_x} \\ \sigma_0 = z\dfrac{\sqrt{2}\,\lambda_z}{\sigma_x} \end{cases} \qquad 2.23$$

We note in Eq 2.23 that the TO wavelength λ_x depends on the depth. Therefore, to obtain a constant TO frequency, the weighting function must be dynamically modified as a function of depth. The deeper the depth, the more the Gaussian peaks are spread away from the center of the transducer. This ensures that the 2D oscillation pattern is independent of the depth, and that the velocity components being measured can become spatially uncorrelated.

2.III.C Transverse oscillation by Fourier filtering

Previously, we described TO implementation by modifying the system aperture. Finding a correct TO frequency can be quite challenging, especially in pathological cases where aliasing rapidly occurs. However, if TO is introduced by receive aperture, its frequency can be modified only if the received raw data were saved. It is quite challenging to save this many data, especially if a high frame rate is used. Moreover, due to the poor lateral resolution of TO images, it is still necessary to provide a standard B-mode for clinicians. Hence, two sets of data should be acquired: one using a receive

aperture introducing TO and a classic aperture for visualization purposes. In addition to increasing the data which need processing, the frame rate is decreased during this process.

The f-k spectrum of the image with TO (Figure 2.9.b) contains four signal regions whose positions correspond to the axial and TO frequencies. (Varray and Liebgott 2013) proposed to directly filter the f-k spectrum of beamformed images to select a lateral frequency by selecting these four signal regions. This approach, done in the Fourier domain, is inexpensive in term of data and processing time, and has been described by Salles *et al*. (Salles, Garcia, et al. 2014). By filtering the f-k spectrum of a beamformed image along the lateral axis, only one lateral frequency can be conserved. If a Gaussian filter is used:

$$\Omega(f_x) = exp(-2\sigma_x^2 f_x^2) \circledast \left(\delta\left(f_x - \frac{1}{\lambda_x}\right) + \delta\left(f_x + \frac{1}{\lambda_x}\right) \right) \quad 2.24$$

where $\Omega(f_x)$ is the lateral frequency of the Gaussian filter and σ_x its standard deviation.

This approach has since been investigated by Jensen et al. (J. Jensen, Stuart, and Jensen 2015) for flow imaging and by Salles et al. (Salles et al. 2015) for tissue motion imaging. For both applications, this filtering approach prove to be relevant and provided good *in vitro* and *in vivo* results.

2.III.D 2D-phase-based estimator for transverse oscillation approaches

As described in Section 2.I.D for Doppler approaches, in 1985 Kasai *et al*. proposed (Kasai et al. 1985) a 1D-phase-based estimator still widely used nowadays. Since then, several 1D or 2D phase-based estimators have been proposed for flow and tissue imaging (J. A. Jensen 2001; Sumi 1999; Ebbini 2006; Sumi 2008; Basarab et al. 2009). Specific estimators have been proposed for TO by Jensen (J. A. Jensen 2001) and by Basarab *et al*.(Basarab et al. 2009). The transverse and axial velocity components were assessed independently using a modified version of the complex autocorrelation (J. A. Jensen 2001). While Basarab *et al.* got rid of the phase jumps issue by developing a phase-based block matching technique. A more trivial approach similar to the one developed by Kasai *et al.* (Kasai et al. 1985) has also been used with TO approaches (Salles et al. 2015; Perrot, Ekroll, et al. 2021). An extension of the Hilbert transform to the n-dimensional (Bulow and Sommer 2001; Hahn 1996) case is used to extract analytic signals.

Once TO is introduced into an US image, its f-k spectrum contains four “spots” corresponding to the axial and lateral wavelengths (Figure 2.9). The Hahn’s approach [81] consists of extracting two single quadrants of this spectrum to obtain the corresponding analytic signals(Bulow and Sommer 2001; Hahn 1996). This technique assumes that the 2D oscillation present in the image can be described as the product of two 1D oscillation signals. The two quadrants are extracted using a simple mask multiplication in the Fourier domain:

$$\Omega(f_x) = exp(-2\sigma_x^2 f_x^2) \circledast \left(\delta\left(f_x - \frac{1}{\lambda_x}\right) + \delta\left(f_x + \frac{1}{\lambda_x}\right) \right) \quad 2.25$$

where $\Omega(f_x)$ is the lateral frequency of the Gaussian filter and σ_x its standard deviation. The Dirac delta function is denoted by $\delta(\cdot)$.

Let us consider a spatial point in the TO image, whose signal $s(t)$ can be written as:

$$s(t) = A(t)\cos(2\pi f_x(x + \Delta x(t)))\cos(2\pi f_z(z + \Delta z(t))) \quad 2.26$$

where A is an amplitude term, f_x and f_z are respectively the axial and lateral spatial frequencies, and Δz and Δx are respectively the axial and lateral displacements.

We arbitrarily chose to extract the phase corresponding to the analytical signal of the two top regions i.e. to the negative axial and negative lateral frequencies, and the negative axial and positive lateral frequencies:

$$\begin{cases} \phi^I(t) = 2\pi f_x\big(x + \Delta x(t)\big) + 2\pi f_z(z + \Delta z(t)) \\ \phi^{II}(t) = -2\pi f_x\big(x + \Delta x(t)\big) + 2\pi f_z(z + \Delta z(t)) \end{cases} \quad 2.27$$

where ϕ^I and ϕ^{II} are the phases of the first and second analytic signals, respectively.

The phase shifts can be expressed as:

$$\begin{cases} \Delta\phi^I(t) = \phi^I(t+\tau) - \phi^I(t) \\ \Delta\phi^{II}(t) = \phi^{II}(t+\tau) - \phi^{II}(t) \end{cases} \Rightarrow \begin{cases} \Delta\phi^I(t) = 2\pi f_x \Delta x(t) + 2\pi f_z \Delta z(t) \\ \Delta\phi^{II}(t) = -2\pi f_x \Delta x(t) + 2\pi f_z \Delta z(t) \end{cases} \quad 2.28$$

where $\Delta\phi^I$ and $\Delta\phi^{II}$ are respectively the phase shifts from the first and second analytic signals; τ is an estimation lag and Δx and Δz are the displacement from t to $t+\tau$.

The displacements can then be obtained through:

$$\begin{cases} \Delta\mathrm{z(t)} = \dfrac{\Delta\phi^I(t) + \Delta\phi^{II}(t)}{4\pi f_z} \\ \Delta\mathrm{x(t)} = \dfrac{\Delta\phi^I(t) - \Delta\phi^{II}(t)}{4\pi f_x} \end{cases} \quad 2.29$$

The axial velocity v_z and lateral v_x velocity components will be obtained through the estimation of the phase shifts:

$$\begin{cases} \mathrm{v_z} = \dfrac{PRF\ c}{\tau}\ \dfrac{\Delta\hat{\phi}^I(t) + \Delta\hat{\phi}^{II}(t)}{4\pi f_x} \\ \mathrm{v_x} = \dfrac{PRF\ c}{\tau}\ \dfrac{\Delta\hat{\phi}^I(t) - \Delta\hat{\phi}^{II}(t)}{4\pi f_x} \end{cases} \quad 2.30$$

where $\Delta\hat{\phi}^I$ and $\Delta\hat{\phi}^{II}$ are respectively the estimated phase shifts from the first and second analytic signals.

From now on, we assume a constant velocity in the observation window to get rid of the τ-dependence. Like in the 1D estimation, the velocity as a function of time can be recovered using a sliding window with a fixed ensemble length. The phase shifts can be estimated using the same estimator as Kasai *et al*. (Kasai et al. 1985):

$$\begin{cases} \Delta\hat{\phi}^I(\tau) = \tan^{-1}\left(\dfrac{\Im\{\hat{R}^I(\tau)\}}{\Re\{\hat{R}^I(\tau)\}}\right) \\ \Delta\hat{\phi}^{II}(\tau) = \tan^{-1}\left(\dfrac{\Im\{\hat{R}^{II}(\tau)\}}{\Re\{\hat{R}^{II}(\tau)\}}\right) \end{cases} \quad 2.31$$

where $\hat{R}^I$ and $\hat{R}^{II}$ are respectively the complex autocorrelation of the first and second analytic signals; $\Im$ and $\Re$ respectively the imaginary and real functions. Spatial filtering of the complex autocorrelation estimates can be performed before velocity estimation to reduce noise in the estimated phase shifts (Udesen and Jensen 2006).

To summarize this phase-based estimation is decomposed into three main steps:

- First, analytic signals are recovered from the TO images using Hahn's approach [81].
- Then, the phase shift of each analytic signal is estimated through its complex autocorrelation (Kasai et al. 1985).
- Finally, velocity components are recovered by projection of those phase shifts.

2.III.E Transverse oscillation applications

Historically, TO has first been developed and applied to flow (J. A. Jensen and Munk 1998; J. A. Jensen 2001). Its reliability for vector flow imaging has been studied with bias and standard deviation as small as 10% when the vessel is parallel to the probe (Udesen and Jensen 2006) i.e., in the most challenging case for the US modality. TO approaches were then extended to tissue motion estimation by Liebgott *et al.* (Liebgott et al. 2010; 2007). After the reliability of TO has been studied *in vivo* (Udesen et al. 2007; Lenge et al. 2015), the approach was implemented on a medical ultrasound scanner - BK ProFocus UltraView (Haugaard and Seerup 2014) (BK Medical Holding Company, Peabody, Massachusetts, United States). TO approaches then became the first 2D-flow estimation method available in a clinical scanner (J. A. Jensen et al. 2019) as they were FDA-approved in 2012 (P. M. Hansen et al. 2011).

Optimization of TO parameters has been studied with a linear (J. A. Jensen 2017), phased array (Heyde et al. 2017) and a convex probe (J. A. Jensen, Brandt, and Nielsen 2015). The optimum TO parameters differed from a linear to a convex probe, as the transducer's parameters are different. The main difficulty with TO implementation with a convex probe is the fact that the elements are placed on an arc circle. The elements are then each facing a different direction and the interactive space for creating TO is then reduced. Once optimized, TO with a convex probe has been rapidly caried to *in vivo* study (Brandt et al. 2015; Brandt 2017).

TO can also be introduced directly through filtering the f-k spectrum of beamformed US images as proposed by (Varray and Liebgott 2013). Through this filtering approach, the TO's wavelength can be easily changed without complication in term of data and processing time(Salles, Garcia, et al. 2014).

2.III.F Transverse oscillation limitations

TO methods tend to introduce a negative bias in the extracted velocity, i.e. the estimated velocity is underestimated. This is explained by the averaging of the velocity across all the PSF width. As this bias depends on both depth and beam-to-flow angle, no fixed compensation is possible (J. A. Jensen 2017). This bias can be significantly reduced with an accurate TO optimization, which also reduces the standard deviation (J. A. Jensen et al. 2016).

The sensibility to beam-to-flow angle has been studied and (Udesen et al. 2007) showed that the transverse estimates are suitable when the beam-to-flow angle is higher than 45°.

2.IV Wall motion estimation approaches

Almost all approaches used for flow estimation are suitable for wall motion estimation. However, for readability, the previous sections have focus on flow estimation. We now present methods used for wall estimation in the arteries.

M-mode US images can be used to study the variation of the carotid diameter (Gamble et al. 1994). It was possible to extract parameters on arterial stiffness and distensibility, including the Young's modulus and the distensibility coefficient. Distensibility and more broadly wall motion can also be assessed through RF-data (Hoeks et al. 1990; Luo and Konofagou 2010; Rabben et al. 2002). An entire field of study is the Tissue Doppler imaging, consisting of estimating the Doppler frequency using similarities functions (Price 2000; Kumar V Ramnarine et al. 2003).

Block matching and optical flow techniques have been deployed, sometimes simultaneously, to estimate wall motion on B-mode US images (Golemati et al. 2012; Gastounioti et al. 2013). Transverse Oscillations methods (Liebgott et al. 2010; Salles et al. 2015) have been adapted to tissue motion estimation. These are particularly useful to estimate the longitudinal motion of the walls, that can be difficult to estimate using other approaches, due to its complexity and low amplitude.

The change in an artery's diameter is due to the passage of the systolic pressure wave and to a lesser extent to the pulse wave. However, the low framerate available in previous US scanners did not permit the study of fast motions such as the pulse wave propagation. The developing of ultrafast US has permitted the study of fast wall motions permitting the visualization of pulse wave propagation. These methods are called Pulse Wave Imaging (PWI) and can give a local measurement of the Pulse Wave Velocity (PWV). The (PWV) is related, under several simplifying assumptions, to the vessel's stiffness by the Moens–Korteweg equation (Moens 1878):

$$\mathrm{PWV} = \sqrt{\frac{E_{\mathrm{young}}\, h_v}{2\, R_v\, \rho\, (1-\nu^2)}} \qquad 2.32$$

where R is the internal radius of the vessel, E_{young} the Young's modulus of the wall, ρ the blood density, ν the Poisson's ratio and h_v and R_v are the thickness and the radius of the vessel.

This equation requires three assumptions about the elastic tube in which it is applied i.e. about the blood vessel: (i) the fluid within the tube is incompressible; (ii) the wall thickness is small with respect to the lumen radius; and (iii) the tube is perfectly elastic. At physiological pressures, incompressibility of the blood is considered to be a plausible assumption. Assumptions ii and iii are not always valid in blood vessels, especially in diseased vessels with atherosclerotic plaques.

The idea of local pulse wave velocity estimation was introduced by (Benthin et al. 1991) and was first applied to human arteries in 2002 (Eriksson et al. 2002) . Since then, many studies have been performed on the subject (Luo, Li, and Konofagou 2012; J. Vappou, Luo, and Konofagou 2010; Couade et al. 2011; Hasegawa, Hongo, and Kanai 2013; Kruizinga et al. 2014; Wang et al. 2019; Perrot, Ekroll, et al. 2021). In addition, several clinical studies have shown that pulse wave velocity would be a very good indicator of cardiovascular risk (Luo, Li, and Konofagou 2012; R. X. Li et al. 2013).

2.IV.A Speckle tracking approaches

Speckle tracking approaches for wall motions study are focusing on estimating the motion of a speckle region due to scatterers in the vessel's walls in successive US images. (Cinthio et al. 2005) develop a method especially for the study of the wall longitudinal motion called "echo tracking". The use of a small block size (originally 0.7 x 0.7 mm²) enable the tracking of specific speckle pattern present in the vessel's walls. (Basarab et al. 2008) proposed motion estimators, based on deformable block matching specific for the study of elastography with US imaging. This further increase the complexity inherent for block-matching algorithms. By making an assumption on the wall motion *a priori*, the specificity of wall motion can be taken into account (Zahnd et al. 2012; 2013). The accuracy is then increased by reducing the accumulation of errors when following the wall trajectory. However, making an assumption on wall motion is not a trivial problem especially in the presence of complex motions occurring in diseased vessels. Furthermore, the issue of noisy data rendering impossible classic speckle tracking approaches was tackled by (Gao et al. 2018). Alternatively, salient image regions can be automatically extracted and used as feature for wall motion estimation (Qorchi, Vray, and Orkisz 2021; Zhu and Wang 2020). The robustness of these methods is increased by using only salient points

automatically reselected at each time step. However, the constant re-selection of salient point rends impossible the estimation of a dense-field motion map.

2.IV.B Differential approaches

Differential approaches have been used to estimate wall motion (Salles et al. 2012). Studies have showed that the differential method of (Lucas and Kanade 1981) gives better results than the one from (Horn and Schunck 1981) and other speckle tracking approaches (Golemati et al. 2012). However, the scatterers of a vessel's wall tend to lead to a quite homogenous US image for the wall, decreasing the accuracy of differential approaches (and of speckle tracking approaches). Differential approaches have been used for atherosclerosis diagnosis by directly accessing the strain in the plaques (Huang, Pan, et al. 2016)

2.V State of the art on simultaneous wall and flow measurement

As a reminder, in clinical routine, arteries pathology assessments are done only with 1D-flow estimation, such as obtained with Color Doppler and Doppler spectrum, and with anatomical information through B-modes images. The framerate tends to be quite low with 100 images per second maximum.

For years, research teams have worked on obtaining 2D vector flow measurement at a high frame rates (Udesen et al. 2008; Tanter and Fink 2014) and complex flow patterns can now be accessed (Mehregan et al. 2014). Moreover, tissue motion has been also studied extensively in research, and has been showed to be related to the mechanical and geometric properties of the vascular system (Fujikura et al. 2007). No clinical scanner offers the possibility to estimate simultaneously wall and flow despite the obvious advantage that such an imaging mode could offer to evaluate the health of arteries. Even in research, only a few groups have worked on this simultaneous assessment, and all of them are focusing on shallow vessels, mostly the carotid artery, using a linear probe.

The first paper on simultaneous flow and tissue measurements was published in 2004 and written by Bambi *et al*. (Bambi et al. 2004). An interrogating ultrasound beam was orientated at approximately 20° to the wall of a common healthy carotid artery leading to suitable signals for Doppler analysis. Echoes generated from the wall and from the blood were obtained along this interrogating beam. Data were then independently processed to obtain both blood flow and wall motion in real-time, and to further estimate the wall shear strain and distensibility. In 2006, Tortoli *et al.* (Tortoli et al. 2006) improved the previous system (Bambi et al. 2004) using a dual beam system by dividing a linear array probe into two sub-apertures. One beam was parallel to the wall for better wall motion estimation and the other one was steered for Doppler estimation. This approach gets rid of the unknown beam-to-flow angle and the Doppler measurements can be properly corrected. In 2008, Hasegawa and Kanai (Hasegawa and Kanai 2008) coupled power Doppler for flow measurement and a phase-tracking method for tissue motion estimation. This is the first work managing to access flow and tissue motions *in vivo* at a high frame rate of 3500 images per second using parallel beamforming. Finally, the radial strain of a healthy human carotid arterial wall and blood flow were simultaneously assessed. In 2010, Balocco *et al.* (Balocco et al. 2010) used the blood flow and wall motion data obtained by the previously described system developed by Tortoli *et al.* (Tortoli et al. 2006). Viscoelastic properties

were extracted with the use of a model. The same year, Wan *et al.* (Wan, Liu, and Ebbini 2010) used a phase-coupled speckle tracking approach to obtain the blood flow, wall motion, and strain in phantoms and *in vivo* carotid. They used a medical scanner acquiring RF data at a frame rate of 111 images per second only considering a limited field-of-view. In 2011, with a dual mode spectral Doppler and B-mode image, the WSR and diameter variation of brachial arteries of 15 healthy volunteers were assessed simultaneously (Tortoli 2011). This dual mode was further refined by (Aizawa et al. 2018) and (Ramalli et al. 2019) who managed to simultaneously assessed WRS and the flow-mediated dilation on the brachial artery over a healthy young cohort. It has also been applied to study the link between longitudinal wall motions and WSS (Ahlgren et al. 2015). Luo and Konofagou (Luo and Konofagou 2011) conducted an *in vivo* feasibility study of wall and blood flow motion in the hearts of mice. By using ECG-gating, they were able to obtain a high frame rate (8000 images per second). However, only periodic phenomena are accessible due to the long acquisition time (here 7 minutes) and due to the use of ECG-gating. In 2012, Niu *et al.* (Niu et al. 2012) proposed an 2D normalized CNN approach on B-mode images. Arterial wall displacement and flow pattern were simultaneously obtained and markers such as WSS and circumferential strain were extracted. Later, this method was successfully applied to extract stress phase angle on phantom and on *in vivo* carotids (Niu et al. 2015). In 2013, Ekroll *et al.* (Ekroll et al. 2013) evaluated a quantitative angle-independent 2D vector velocity estimator for both flow and wall motion assessment. However, the achieved frame rate is quite low (63 images per second) due to the complexity of the duplex mode and the use of strong compounding. The technique was evaluated both on simulations and on *in vivo* healthy carotids. Perrot *et al*. developed a plane wave sequence coupled with transverse oscillation able to simultaneously detect flow and wall motion. The sequence was first validated on PolyVinyl Alcohol phantoms of different rigidity (Perrot et al. 2017) and then on *in vivo* carotids (Perrot et al. 2018). A pilot study was later realized on healthy and diseased carotids (Perrot, Ekroll, et al. 2021). In 2018, Fekkes *et al*. (Fekkes et al. 2018) extracted simultaneously the vascular strain and blood vector velocity with both a high-frequency probe and a standard frequency probe in a phantom study. Displacements were estimated using a 2D normalized cross-correlation-based method. In 2019, Goudot *et al.* evaluated WSS in carotid stenosis using vector flow imaging (Goudot et al. 2019). The same year, Karageorgos *et al.* (Karageorgos et al. 2019) were able to extract the PWV with vector Doppler and WSS on stenotic phantoms and carotids *in vivo*. Papadacci *et al.* (Papadacci et al. 2019) extracted, in a single heartbeat, Color Doppler, tissue Doppler, and spectral Doppler in the heart of three volunteers. The data were acquired using a 2D ultrasound probe, at a high frame rate (5 200 volumes per second) and were then processed semi-automatically to obtain several Doppler indices. Recently, Karageorgos *et al.* (Karageorgos et al. 2021) coupled a multi-angle vector Doppler for assessing tissue motion to a cross-correlation-based vector flow imaging method. They were able to extract pulse wave velocity alongside with VFI on phantoms and *in vivo* healthy carotids.

2.VI Thesis approach and goals

In this chapter detailing the current state of the art, several studies have been described showing the increasing interest in simultaneous assessment of flow and wall motion in arteries. Tissues related metrics have been extracted alongside hemodynamics metrics in simulation, in phantoms and on carotids and hearts *in vivo.* In addition to give clinicians additional tools to diagnose and monitor cardiovascular diseases, these studies also permit to better comprehend relation of fluid tissue interaction (Z. Y. Li et al. 2006; Deplano et al. 2013; 2014). However, none of these studies focus on

deep vessels despite the evident clinical interests stated in Chapter 1. In clinics, the abdominal aorta is investigated with convex transducers thanks to their lower center frequency and larger field of view than linear probes. Specific methods and approaches have to be developed for convex probes as their geometry and the elements positions deeply influenced the emitted ultrasound field. The abdominal aorta can also be assessed by endoscopic ultrasound: an ultrasonic probe is inserted inside the body through the esophagus and deep tissue can directly be assessed from the inside. Endoscopic ultrasound is typically performed by gastroenterologists or pulmonologists who have had extensive training. It is less convenient and more time consuming than using a convex probe for abdominal aorta scans, but can be useful in extreme conditions, such as a patient's obesity.

In this chapter, we detailed the current state of the art for transverse oscillation approaches. TO methods have been developed for vectorial flow (J. A. Jensen and Munk 1998) and adapted for tissue motion estimation (Salles, Garcia, et al. 2014) at a high frame rate. TO has been optimized for vectorial flow on a convex probe (J. A. Jensen, Brandt, and Nielsen 2015) but the great number of emission needed lead to a relatively low framerate (<10 Hz *in vivo*). In this thesis, we extended the TO method to convex probes using diverging waves leading to a high frame rate.

In the next chapter, the contributions of this thesis will be detailed. First, we designed an ultrafast ultrasound sequence allowing deep vessel exploration with an optimized compounding scheme. The TO approach was adapted to this emission sequence with our convex probe. With a 2D phase-based estimator, the motion estimation was validated on phantoms of different rigidity.

Chapter 3: Ultrafast imaging sequence for tissue and flow investigation

This third chapter is dedicated to the ultrasound (US) emission scheme used to insonify the medium. First, the US field emitted by the C631 convex probe (Esaote SpA, Italy) was studied using a hydrophone. Knowing the exact US field allows a more accurate understanding of the resulting backscattered echoes. Indeed, it is often considered that the transducer insonifes a perfect thin slice in front of the medium. This is of course a simplification, and a region having some extent in the elevation direction is also insonified, depending on the probe 's characteristics and on the depth of the medium. Knowing the US emission field help to place the probe correctly during acquisition.

Once the emission field of the probe was known, the US emission scheme was tackled. The goal was to get a good image quality while preserving a sufficient framerate. The signal-to-noise ratio is increased with compounding sequences, i.e. by coherently combining sub-images containing different information. The main drawback of compounding is the inherent reduction in framerate: a compromise must be reached between framerate and image quality. An optimal compounding sequence specific to convex probes was then studied. A proceeding at *IEEE International Ultrasonics Symposium 2020* was presented on this work: "Sequence optimization for high frame rate imaging with a convex array" (Ghigo et al. 2020).

At the end of this chapter, image formation is discussed. A common delay-and-sum algorithm was implemented. The position and directivity of the convex probe's elements were considered to only select relevant data during this beamforming.

3.I Probe characterization

3.I.A Acquisition set-up

To characterize the probe's emission field, a hydrophone was submerged in a tank full of water with the CA631 convex probe (Esaote SpA, Italy) barely immerse at the top of the tank. The properties of the probe are reported in Table 3.I.1. A diverging wave without any delay was sent by the 64 middle elements of the probe into the medium. The excitation signal was a 7-cycle sinusoidal burst with a Hanning temporal apodization at a center frequency of 3.5 MHz. The signal received by the hydrophone was then recorded and saved in memory before moving to another known position. This process is then repeated on all the ROI: a rectangular box of dimension 40x10x50 mm^3 beginning at a

depth of 2 cm. This ROI was sampled every 0.5 mm in the lateral and elevation direction, and every 3.3 mm in the axial direction. This leads to a matrix of 81x21x15 for a specific time in the ROI. At each position, the hydrophone recorded for 64 µs with an 8 ns sampling time.

3.I.B Results and conclusion

First, the signal received by the hydrophone when it is aligned with the probe was visualized in order to verify that the US signal sent by the probe is correct with a number of cycles and mean frequency consistent to those we fixed (Figure 3.1).

The maximum amplitude received at each position in the ROI is shown in Figure 3.4. This representation allows to visualize all regions insonified at one time or another. Along the Y-axis (Figure 3.4.a), the US field can be seen diverging with depth as expected, following the natural curvature of the transducer. The more interesting results happened along the X and Z-axis. In Figure 3.4.b, the impact of the geometric focus can be clearly visualized, concentrating the US field toward 6.5 cm. After 5 cm depth, the field is quite narrow with an insonification of around 1 mm in the Y-direction. However, just before this narrowing, destructive interferences happened in front of the probe (at Y=2mm, due to a small misalignment probe/hydrophone). If a region situated at this depth is of interest (Z≈ 4cm), the echoes received by the probe will mostly come from surrounding tissues and not from the ROI. In Figure 3.4.c, it can be seen that at one time or another, a region of 1 cm in elevation will be insonified. However, at the geometric focus, this region insonified in elevation is approximately equal to 1 mm (Figure 3.2.c), highlighting the importance of a good probe/ROI distance placement.

Our study was limited in depth at 7 cm. It can be safely assumed that the US field present a symmetrical shape after the geometrical focus. The elevation insonification will then increase after 6.5 cm, following an hourglass shape.

Table 3.I.1: CA631 Probe parameters

Number of elements	192
Radius of curvature	R = 60.3 mm
Field of view	-30°/30°

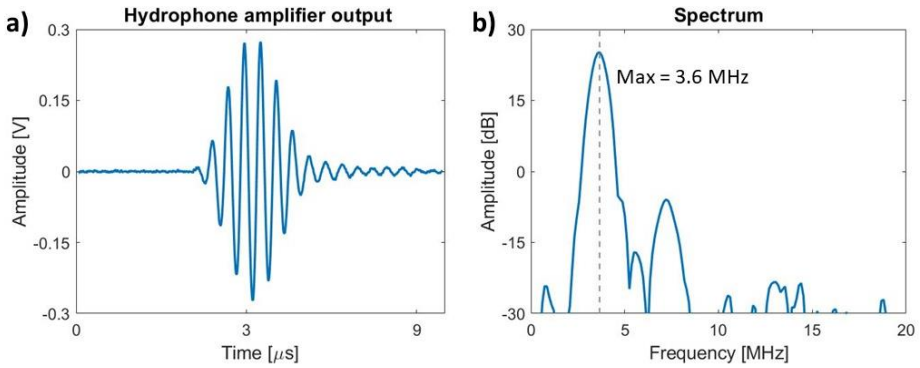

Figure 3.1: a) Ultrasound signal received by the hydrophone when the probe is aligned and its corresponding spectrum. The electronic noise can be visualized before the hydrophone received the signal i.e. before 2 μs. The 7-cycles of the US signal can be visualized and the maximum frequency on the obtained spectrum corresponds to the one sent by the probe (3.6 MHz vs 3.5 MHz).

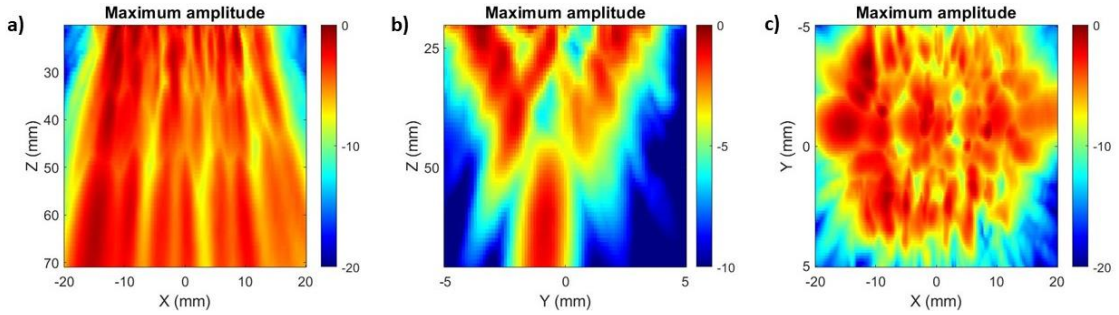

Figure 3.4: Maximum amplitude during time along a) the Y-axis, b) the X-axis, and c) the Z-axis. a) the diverging US wave can be visualized. b) Along the Y-axis, the geometric focus concentrate the US wave in one point (here at Y=2mm because of a misalignment between the probe and the hydrophone. Some destructive interferences can be visualized, such as just before Z = 5 cm in front of the probe (Y=2mm). c) a large region in front of the probe gets insonified at a time or another.

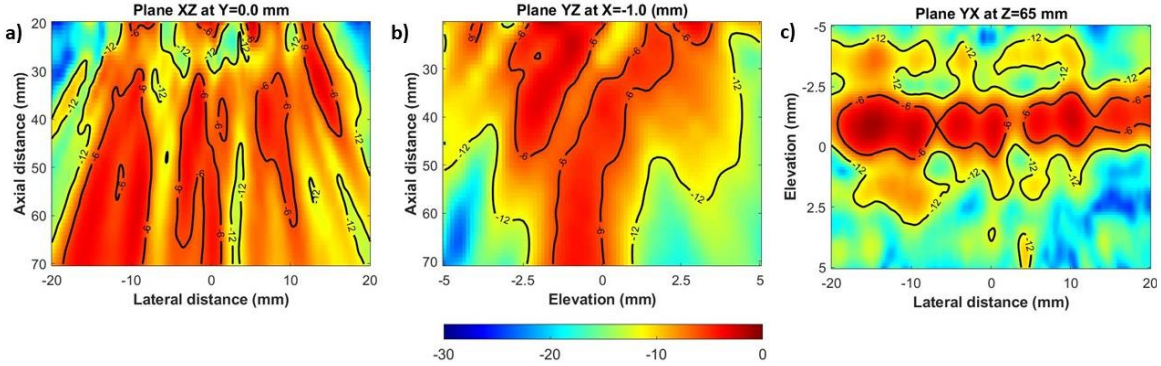

Figure 3.2: Intensity of the emitted ultrasound field a) in the XZ plane, b) in the YZ plane and c) in the YX plane. a) in the XY plane, at Y=0, the field is correctly diverging. Some destructive interferences can be visualized. b) in the YZ plane, the field is represented at X=1 mm because of a slight misalignment between the probe and the hydrophone. A large portion of the medium is insonified in elevation at shallow depth. This is due to the geometrical focus of the probe (65 mm) which makes the field converges in elevation. From 5 cm, the -6 dB insonified field covered around 1 mm in elevation. c) in the YZ plane, the field is represented at the geometrical focus, where the field is the narrower in elevation. At this depth, the medium is mostly insonified over a 1 mm range in elevation in front of the probe.

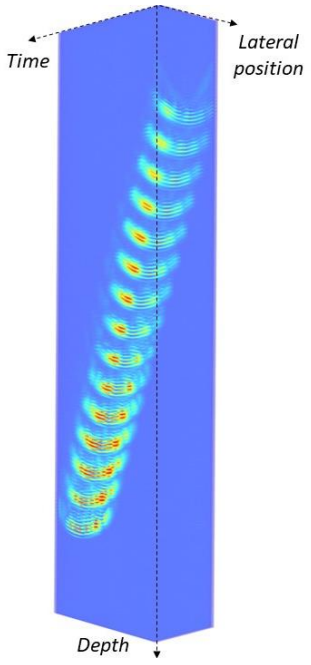

Figure 3.3: Representation of propagation of the front wave recorded by the hydrophone in front of the probe. The front wave is diverging as expected. The intensity of the wave front increases toward the geometric focus point.

This study is particularly useful to understand the acquired data. For example, if an interesting medium is situated at 3 cm from the probe, a slice of around 4 cm in elevation will be insonified at -6dB in front of the probe (Figure 3.2.b). However, the space just in front of the probe will get less energy at this depth than the surrounding medium (Figure 3.4.b). If a motion estimation algorithm was then applied to the data, the large echoes received from the elevation might explain some unexpected results. As expected, the best distance probe-ROI is close to the geometrical focus, where 1 mm in elevation is insonified. This insonification in elevation seems quite constant over a 3 cm range across the geometrical focus. Hence, whenever possible, if using a CA631 probe, one should try to place the probe from 5 to 8 cm of the ROI. In most clinical cases, this is not easily done. For the study of the AA, as its depth increases toward the lower part of the body, it might be possible to select the best segment in function of its depth. For phantom studies, the phantom's depth can be adjusted to fit inside this 3 cm range.

3.II US sequence Emission

High frame rate US imaging based on broad insonification (plane or diverging waves), permits the study and visualization of fast phenomena. However, without compounding, this high framerate comes at the expend of image quality. To overcome this issue, it is possible to combine images obtained from several transmissions. Indeed, by coherently combining beamformed sub-images containing different information, a synthetic transmit focusing is achieved, which improves image quality. The way in which such sub-images are obtained influence deeply the final image quality. While optimal compounding sequences have been extensively studied for linear or phased arrays (Couture, Fink, and Tanter 2012; Poree et al. 2016), way less works have been carried out for convex probes.

(J. M. Hansen and Jensen 2011) have proposed a compounding sequence using synthetic aperture consisting of acquiring an entire data set of the medium. The data set is obtained by emitting spherical wave with a sliding subaperture and receiving with all the probe's elements. This leads to a framerate similar to conventional imaging. Using the acquired data set, transmit and received focus can be realized for compounding by applying different delays and apodizations in post processing. The increase in resolution offered by this technique comes however at the cost of an important increase in RF data processing. (Besson et al. 2020) proposed to send plane waves in the semi-polar plan. Except for the easy mathematical understanding offered by this technique, the physical advantages of such emissions remain unclear. A study of different compounding sequences specific to convex probes is presented in this section.

3.II.A Number of maximum compounded emissions

Depending on the medium of interest characteristics (depth, velocities to estimate), some inherent limitations to both the US modality and the chosen motion estimation algorithm must be considered to properly design an imaging sequence. Specifically, the maximum depth of the medium limits the maximum achievable pulse repetition frequency. However, motion estimation necessities a high framerate if high velocity estimates are required. There is a compromise between facts limiting the PRF (high depth investigation, use of compounding etc.) and requirements to have a high enough PRF (visualizing transient phenomena, estimating high velocities etc.). Before implementing compounding sequence, we need to investigate the limitations on the PRF present in our case.

3.II.A.a Limits inherent with depth

For the study of the AA, its depth is the main limitation in term of framerate. It can vary from 5 to 20 cm depending on the amount of abdominal fat present. Its normal healthy diameter is around 2 cm. The round-trip time of the ultrasound wave leads to a limitation of the pulse repetition frequency given by:

$$PRF_{max} = \frac{c}{2\, r_{AA}} \tag{3.1}$$

where c is the speed of sound in the medium, often considered equal to 1540 m/s, and r_{AA} is the maximum depth necessary to properly image the AA.

The depth of the AA depends on each patient (sex, age, height, weight…), and it is difficult to make a global estimation of r_{AA}. We can consider that the typical patient needing an AA screening is over 60 years old, with some abdominal fat. Assuming that the patient is not obese, the AA's location can be considered as 20 cm from the skin, below abdomen fat and muscle. The normal caliber of the abdominal aorta increases with age and is larger in men than in women. Taking the worst case scenario of a male over 80 years old, the mean diameter of his AA is 2 cm (against 1.5 cm for a female) (Sonesson, Hansen, and Lanne 1993). Then, r_{AA} can be considered equal to 22 cm. Hence, a maximum PRF of 3.5KHz is obtained.

3.II.A.b Limits inherent with flow estimation

Flow phenomena occurring in the AA are fast and transient. For example, the peak systolic velocity (PSV), that will be denoted v_{max} in this section, is around 120 cm/s (Humphrey and Holzapfel 2011),. It is common to assume that when the PSV occurs, blood is flowing parallelly to the vessel's walls. For estimating the blood velocity, the most challenging case occurs when the direction of the blood flow is perpendicular to the US beam. Here this case happens for the center element of the convex probe, when the blood flow is completely tangential, i.e. $|\vec{v}| = |\overrightarrow{v_t}|$. The maximum tangential displacement, denoted Δt°_{max}, that can be estimated between two frames depends on the estimation technique chosen. In this thesis, we implanted the transverse oscillation technique with a convex probe, introducing a tangential oscillation of wavelength λ_t in the medium as will be explained later on in Section 4.I. The maximum displacement then depends on λ_t:

$$\Delta t^{\circ}_{max} = \frac{\lambda_t}{2} \tag{3.2}$$

Leading to:

$$PRF_{min} = \frac{2\, v_{max}}{\lambda_t} \tag{3.3}$$

As

$$v_{max} = \Delta t^{\circ}_{max}\, PRF \tag{3.4}$$

With a convex probe, λ_t is introduced in the medium in degree, its value in meter depends on the radial distance of interest, here equals to that of the AA r_{AA}:

$$\lambda_t(r_{AA}) = \frac{\lambda_{t(°)}\pi}{180}(R + r_{AA}) \tag{3.5}$$

where R is the radius of the convex probe (here R=6.03 cm).

As detailed in the following chapter, the tangential wavelength introduced is $\lambda_{t(°)} = 1.2$, i.e. $\lambda_t(r_{AA}) \approx 5.87$ mm. Using Equation 3.3, we can deduce that the minimum PRF to estimate the PSV flow is $PRF_{min} \approx 400\ Hz$.

3.II.A.c Limits inherent with PWV assessment

To be able to estimate the PWV, the propagation of the pulse wave must be observed in at least two frames. The number of frames where the pulse wave propagates depend on the width of the vessel's wall visible in US imaging, here denoted W_{vessel}:

$$Nb_{frame} = \frac{W_{vessel}}{PWV}\, PRF \qquad 3.6$$

The robustness of a method to estimated PWV depends of course on its PRF, but also on the Field Of View (FOV) provided on the vessel, i.e; W_{vessel}. As convex probes provide FOV larger than linear probes, the PRF needed to estimate PWV with these probes can be lowered. In the literature, PRF lower than 500 Hz has been used (R. X. Li et al. 2013; Jonathan Vappou et al. 2011). Estimating the PWV with a convex probe does not represent a constraint on the PRF as strong as estimating high flow velocities.

If we consider a typical case on the carotid with a linear probe: PWV≈5 m/s, W_{vessel}≈3 cm. PWV estimation have been carried out with linear probes with framerate lower than 1kHz (Huang, Guo, et al. 2016). We obtain a Nb_{frame} value of 6 i.e. six frames where the pulse wave propagates seems to be enough for robust PWV estimation. If we assume that the necessary number of frames are the same with a convex probe, Eq. 4) is still valid and can be used to find the minimum PRF necessary to estimate the PWV. Convex probes offer a large FOV, here we assume $W_{vessel} \approx 5$ cm. Supposing a stiff AA, the PWV can be assumed to be around 9 m/s (R. X. Li, Qaqish, and Konofagou 2015). We then obtain a PRF_{min} of 1 kHz.

3.II.A.d Maximum number of sub-images

The number of possible sub-images to be compounded depends on the imaging depth and the final image quality needed but also on the velocities to be estimated and the estimation methods chosen. In our case, the PRF is limited to 3.5 kHz by the imaging depth, while a minimum PRF of 400 Hz and 1 kHz are necessary for flow and PWV estimations, respectively. With these constraints on the PRF, we can deduce that only three emissions, i.e. three sub-images, can be compounded. To the best of our knowledge, no previous work has studied the compounding sequence using a convex probe with such stringent constraints.

3.II.B Virtual sources disposition

Very few studies have been carried out on compounding sequences using a convex probe while preserving a high framerate (J. M. Hansen and Jensen 2011; Besson et al. 2020). In this work, five different configurations (CFGs) of Virtual Sources (VS) spatial distributions were investigated. The natural center of the probe, i.e. the center of the circle on which the probe's elements are placed is taken as a reference point and denoted O. The radius of the probe is denoted R.

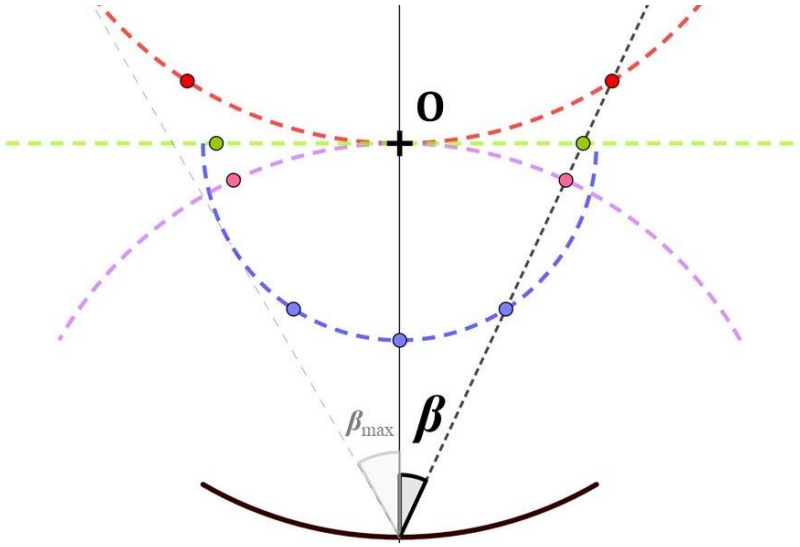

Figure 3.5: The different configurations are illustrated (blue: haR CFG, red: rad CFG, green: hoL CFG, pink: anR CFG). Their corresponding VS are pictured as color dots. β is the angle setting the spacing between VS, varying from 5 to 40° in 5° steps (except for CFG haR and rad, where β is limited to 30° as represented by β_{max}). The probe is represented by the black line and its center O by a black cross. The location of the center of the probe is the location of a VS for all CFGs expect CFG haR.

All these different CFG were chosen in regard to standard distributions used for compounding with a linear probe (Salles et al. 2019) as explained in the following list. VS were evenly distributed on each of the CFG.

1. half-radius configuration (haR CFG). VS are distributed on a circle of center O and of radius $R/2$. The aperture is chosen to be a sliding sub-aperture of 128 elements.
2. radius configuration (rad CFG). VS are distributed on a circle of center $(0, -2R)$ and of radius R. It corresponds to steering diverging waves with the full aperture of the probe.
3. horizontal line through the array pivot configuration (hoL CFG). VS are distributed on a horizontal line passing through O. It consists in placing VS on a straight line as often done with a linear probe.
4. anti-radius configuration (anR CFG). VS are distributed on a circle of center the middle element of the probe and of radius R. It consists in placing the VS equidistant to the center of the probe.

All VS distributions are represented in Figure 3.5. Different spacing of the VS positions were tested by changing their corresponding angles $(-\beta, 0, \beta)$. Different values for β, ranging from 5 to 40° in 5° steps, were tested. For CFG haR and rad, the maximum possible β_{max} value is 30° being limited by the tangent, as illustrated in Figure 3.5. Apodizations in emission and reception were given by a Hanning window over all elements of the probe, expect for the haR CFG where a sliding Hanning window of 128 elements was used.

Finally, diverging waves (DWs) achieved by linear delays with a steering angle of β were also implemented. These CFG were compared to a single diverging wave following the array curvature (1DW) i.e. with no delays.

3.II.C Experimental set-up

Experiments to determine the best compounding sequence were realized using the ULA-OP 256 scanner (Boni et al. 2016) and the CA631 convex probe (Esaote SpA, Italy) – whose parameters are given in Table 3.I.1– on a Gammex Sono403™ phantom. We focus our attention on the scatterer and

Table 3.II.1: Acquisition parameters

Transmit frequency	f_0 = 3.5 MHz
Sampling frequency	39 MHz
Transmit burst	3-cycle sinusoidal burst
Speed of sound	c = 1540 m/s
Pulse repetition frequency	PRF = 3000 Hz
Transmit apodization	Hanning CFG haR: Sliding Hanning on 128 elements
Receive apodization	Hanning

on the anechoic cyst located at 6 cm highlighted by yellow arrows on Figure 3.6. Experiment parameters are shown in Table 3.II.1.

The resolution, measured as the width of the point spread function (PSF) at -6 dB, is assessed in polar coordinates, leading to a resolution in radian or degree. This is done to evaluate the resolution in the correct orientation of the PSF. The following equation is used to convert the resolution in radian $reso_{rad}$ to meter $reso_m$ knowing the radial distance r_s:

$$reso_m = reso_{rad}(R + r_s) \tag{3.7}$$

Contrast-to-Noise Ratio (CNR) is computed on the final compounded B-mode image in polar coordinates to avoid the influence of interpolation.

$$CNR = 20\ log_{10}\left(\frac{|\mu_{cyst} - \mu_{bg}|}{\sqrt{\sigma_{cyst}^2 + \sigma_{bg}^2/2}}\right) \tag{3.8}$$

where μ_{cyst} and μ_{bg} (σ_{cyst}^2 and σ_{bg}^2) are the means (variances) pixel values, after log compression, of the cyst and the background regions, respectively.

3.II.D Results and conclusion

The resolution and CNR values obtained are reported in Figure 3.7 a) and b) respectively.

In terms of resolution, CFG DWs gives poor results, showing the great difference between the use of a linear and convex probe. Cfg rad, hoL and anR all give pretty similar results, as expected as their VS are near to each other. The best β angle for theses CFG is 15°, with a resolution<1.1° at a depth of 6 cm i.e. 2.3 mm (Eq.3.7) The CFG giving the best resolution is haR with its minimum resolution of 0.95° (2 mm) obtained at $\beta = 25°$.

The CFG behave similarly for the CNR. Cfg DWs gives the poorest results. Cfg rad, hoL and anR have similar behavior with a CNR as high as 12 dB at $\beta = 5°$. The CFG haR gives the best CNR (12.4 dB at $\beta = 20°$).

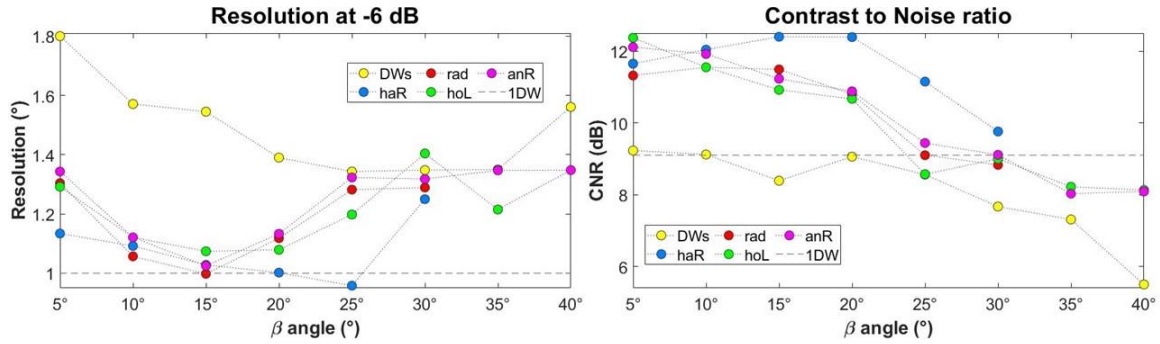

Figure 3.7: The resolution in degree a), and contrast-to-noise ratio b), obtained at 6 cm-depth for all CFGs and β angles are displayed.

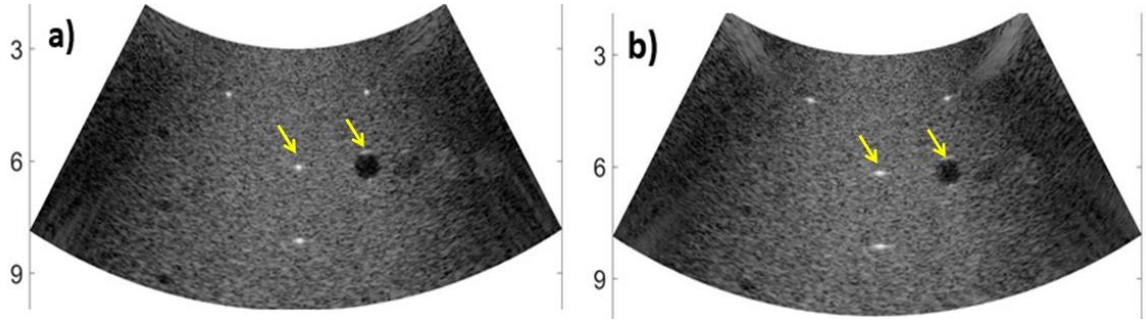

Figure 3.6: a) the best B-mode images in terms of contrast and resolution obtained with the sliding window (CFG haR, β =20°) b) shows the B-mode image of a wave without any delays (CFG 1DW) (without compounding). All B-modes images are displayed in dB [-60 0]. The yellow arrows points to the considered scatterer and anechoic cyst.

The CNR and resolution obtained with only one diverging wave (1DW) are 9.1 dB and 1°, respectively. All CFG manages to get a higher CNR than without any compounding in at least one value for β, showing the interest of compounding. Nevertheless, in term of resolution, only CFG haR and rad manage to perform better than 1DW for at least one value for β.

For the CFG haR (the best one), if we both consider resolution and CNR, the best angles are 25° and 20° respectively. For $\beta = 25°$, the CNR decreased rather heavily at 11.15 dB. For $\beta = 20°$, the resolution increased by less than 0.05° leading to a resolution of 1° (2.1 mm). The best compromise between resolution and CNR seems then to be the sliding CFG haR at $\beta = 20°$ displayed in Figure 3.6.a. For comparison purposes, the image obtained without any compounding (CFG 1DW) is displayed in Figure 3.6 b.

3.III Image formation

Beamforming is performed with a Delay-And-Sum (DAS) algorithm. In this thesis, the directivity and position of the elements were considered to select only relevant data during DAS summation. With a linear probe it is usually done by correctly fixing a f-number (Perrot, Polichetti, et al. 2021). However, the very notion of f-number is not directly transferable to a convex probe utilization.

Assuming monochromatic transmission, the directivity diagram of an element of width w can be expressed as a function of the angle ϑ. For a piston-like element in a soft baffle, which is a current assumption, it is given by (Selfridge, Kino, and Khuri-Yakub 1980):

$$D(\vartheta) = cos(\vartheta)\ sinc(\pi \frac{w}{\lambda} sin(\vartheta)) \qquad 3.9$$

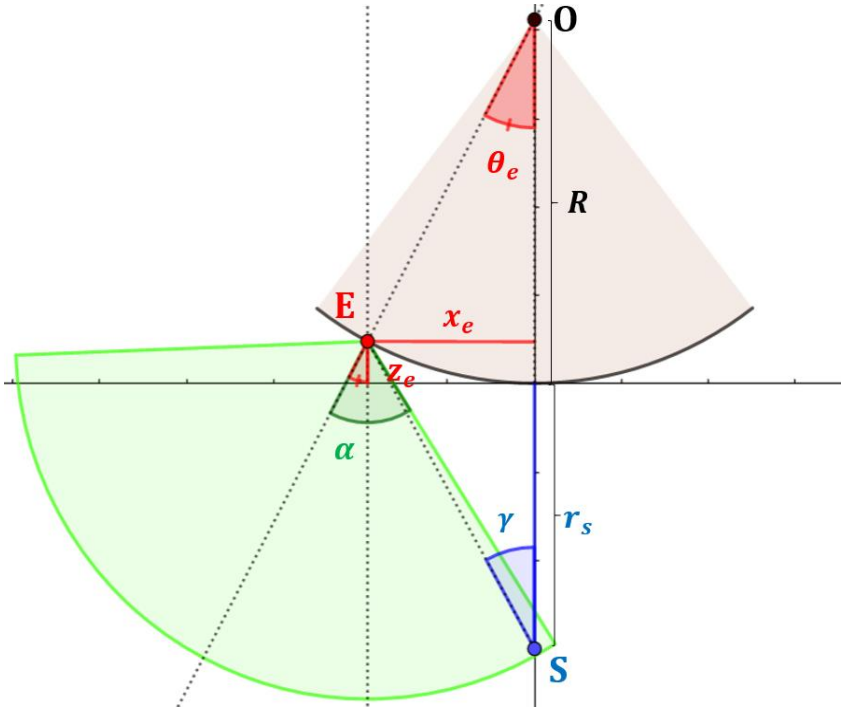

Figure 3.8: Representation of the notion of directivity α with a convex probe of center O and radius R. E is an element of the probe and S a scatterer.

where λ is the US wavelength, in our case $\lambda \approx 0.5$ mm. Heuristically we consider the backscattered echoes only if $D(\vartheta) > 3\ dB$, leading to an opening angle α of approximatively 27° in our case.

In Figure 3.8, we represent the convex probe of center O and radius R. An element E of polar coordinates (R, θ_e) and of cartesian coordinates (x_e, z_e) is displayed. Its directivity at -3dB is represented by the green cone of angle α. For clarity, α is here larger than typical directivity. For calculus purpose, the angle γ is defined between a scatterer S located on the z-axis and the element E. The backscattered echoes from S need to be considered only if they are visible by the element E i.e. only if:

$$|\alpha - \theta_e| > \gamma \tag{3.10}$$

We can compute γ by:

$$\gamma = tan^{-1}\left(\frac{x_e}{r_s + R - z_e}\right) \tag{3.11}$$

It is easily possible to go from cartesian to polar coordinates through:

$$\begin{cases} x_e = R\ sin(\theta_e) \\ z_e = R\ cos(\theta_e) \end{cases} \tag{3.12}$$

Eq. 3.12 then becomes:

$$\gamma = tan^{-1}\left(\frac{sin(\theta_e)}{r_s/_R + 1 - cos(\theta_e)}\right) \tag{3.13}$$

As $|\alpha - \theta_e|$ is known for each element of the probe, it is possible to determine for every point of interest in the medium if it should be considered or not.

Figure 3.9 illustrates the importance of using accurate beamforming parameters. On the Gammex phantom, the tangential resolution at -6 dB is evaluated without (a) and with (b) the use of Equation 3.10, i.e. without and with taking into account the elements directivity and position. Two specific strings are targeted, one located on the probe's center axis at (0 cm ,6 cm) and another one angulated

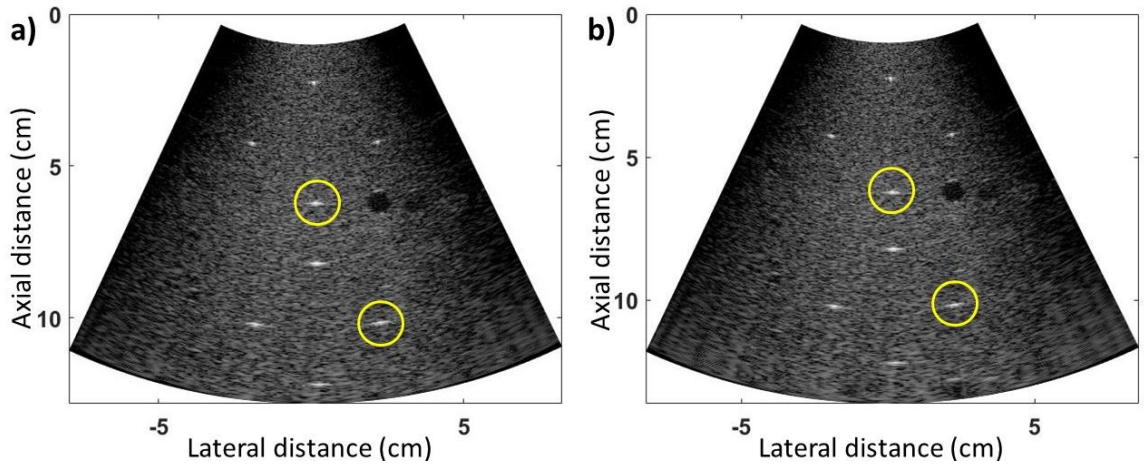

Figure 3.9: IQ images obtained on the Gammex phantom with a dynamic of -40 dB: a) without any consideration on elements position and directivity; b) with the use of Equation 3.10.

at (2cm ,10cm) highlighted by yellow circles in Figure 3.9. The axial resolution at -6 dB can be considered constant for both strings and both beamforming parameters at 0.49 mm. The tangential resolution at -6 dB is improved by correctly implementing the DAS algorithm: the width of the PSF decreases from 0.94° to 0.74° for the non-angulated string and from 1.04° to 0.9° for the angulated string. Using Equation 3.7, we obtain that the tangential resolution is improved by 0.21 mm (0.99-0.78) for the non-angulated string and 0.25 mm (1.82-1.57) for the angulated string.

3.IV Chapter conclusion

In this chapter, the emission/reception was studied with the CA631 convex probe. First, the US emission field was assessed using a hydrophone. Knowing the exact US emission field gives an accurate understanding of the echoes recorded and hence of all future results obtained with this data. A compounding sequence allowing to conserve a sufficient framerate was then studied. The best compounding scheme, haR CFG with β 20°, was determined between several possible configurations. This sliding-window emission scheme will then be implemented for all the rest of this thesis. Once the recorded data are acquired, beamforming is needed to obtain US images. This image formation step is not to be neglected and the directivity and position of the elements were taken into account in the delay-and-sum algorithm. Now that the emission, reception, and beamforming were discussed, motion estimation will be discussed in the following chapter.

Chapter 4: Flow and tissue motion estimation with a convex probe

In this chapter, the motion estimation algorithm based on the transverse oscillation (TO) technique is detailed. This technique was then validated in simulation and the TO parameters were optimized for flow measurement. A proceeding at *IEEE International Ultrasonics Symposium 2019* was presented on this work: “High Frame Rate Vector Flow Imaging with a Convex Array in a Simulated Vessel Phantom” (Ghigo et al. 2019).

Once the motion estimation algorithm was validated on the flow in simulation, an experimental set-up was developed where tissue and flow motion could be assessed simultaneously; Several phantoms with different stiffnesses were realized to validate the potential of our approach for assessing both the flow and the tissue motion simultaneously.

4.I TO with a convex probe

As described in Chapter 2 Section 2.III, TO methods are already used for simultaneous flow and tissue motion estimation with a linear probe. With the use of a convex probe, previous teams have manage to introduce TO using received apodization as in Section 2.III.B. To the best of our knowledge, TO have never been implemented using Fourier filtering on a convex probe(Section 2.III.C). Furthermore, convex implementation of TO were only focused on flow estimation at low framerate (J. A. Jensen 2013; 2014; J. A. Jensen, Brandt, and Nielsen 2014; Brandt et al. 2015; J. A. Jensen, Brandt, and Nielsen 2015).

4.I.A Implementation

4.I.A.a TO introduction

When using a linear probe, a natural oscillation is present in the axial direction. TO methods then introduce an oscillation in the lateral direction. The axial and lateral motions can then be observed and recovered. When a convex probe is used, the natural oscillation is present in the radial direction. If TO are introduced without any pre-processing step, the introduced oscillations will be present in the tangential direction. However, if before TO introduction, US data are interpolated onto a cartesian grid, the introduced oscillations will be in the lateral direction. The resulting PSF will then present an angulation as displayed in Figure 4.1, and this will affect the estimated velocities. That is why all

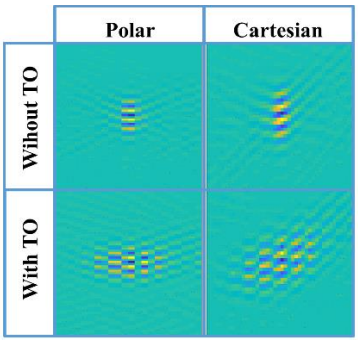

Figure 4.1: PSFs obtained on a scatterer position at (5 cm, 5°), before and after transverse oscillation (TO) filtering, in polar and Cartesian coordinates; 2D oscillations can be seen after TO filtering; PSF orientations are visible in Cartesian coordinates.

following operations are carried out in the polar coordinate system as the PSF is invariant with angle in this domain. Interpolation over a Cartesian grid was used for visualization purpose only.

To create this tangential oscillation, we choose to use a filtering approach, as employed in (Salles et al. 2015). (Salles et al. 2015). In this technique, the 2D Fourier spectrum of each US image is multiplied by a mask consisting of two Gaussians to preserve only the four distinctives spots present in the amplitude spectra of the TO images. The parameters of these Gaussians are the key parameters to control the oscillations' properties. We use a similar approach where the 2D-Fourier transform of each RF image is filtered. Note that since the data are in polar coordinate system, instead of speaking about lateral wave number direction, we speak instead of tangential direction. The mask used can be expressed as:

$$\Omega(k_t) = exp(-2\sigma_t^2 k_t^2) * \left(\delta\left(k_t - {}^{1}/_{\lambda_t}\right) + \delta\left(k_t + {}^{1}/_{\lambda_t}\right) \right) \qquad 4.1$$

where $\Omega(k_t)$ is the mask of the Gaussian filter at the tangential wave number k_t, σ_t its standard deviation, λ_t the tangential wavelength introduced and $*$ the convolution operator.

After TO filtering, the modulus of the resulting Fourier spectrum is composed of only four spots aligned at the US frequency and at the TO tangential spatial frequencies (introduced with mask multiplication). The barycenter of each spot is situated at $\left(\pm f_0, \pm \frac{1}{\lambda_t}\right)$. Note that λ_t is a spatial oscillation introduced in the tangential direction of the image: it is hence an angle expressed in degree. The tangential spatial frequency then obtained, denoted f_t, is equal to ${}^{1}/_{\lambda_t}$ and expressed in degree^{-1}.

This filtering technique can produce theoretically TO with any tangential spatial frequency. In practice the frequency content of the initial image is limited and λ_t should be chosen accordingly. If $\lambda_t$is chosen too small compared to the frequency content of the initial image, the TO filtering will only conserve noise as with λ_t=0.9° in Figure 4.2. On the contrary, if λ_t is fixed too large, the two Gaussians present in the TO filter will overlap. The resulting Fourier filtering will not result in the characteristic spots of a TO's spectrum, and no TO will be introduced (as with λ_t=2.5° in Figure 4.2). By studying the content of the US image, a correct interval of possible $\lambda_t$values can be deduced.

Similarly, the value of the standard deviation σ_t of the gaussians used for TO filtering have an impact on the 2D PSF obtained after TO introduction. As illustrated in Figure 4.3, if σ_t is chosen too small, the two Gaussians present in the TO filter will overlap. The resulting Fourier filtering will not result in the characteristic spots of a TO's spectrum, and no TO will be introduced. On the contrary, if σ_t is fixed too large (as with σ_t=2.5° in Figure 4.3), the two Gaussians will be very narrow, and not a lot of signal will be preserved after TO filtering. TO will be introduced but with a low intensity, rendering motion

estimation not feasible. In conclusion, the Gaussian's standard deviation should be chosen according to the desired TO wavelength and the frequency content of the initial image.

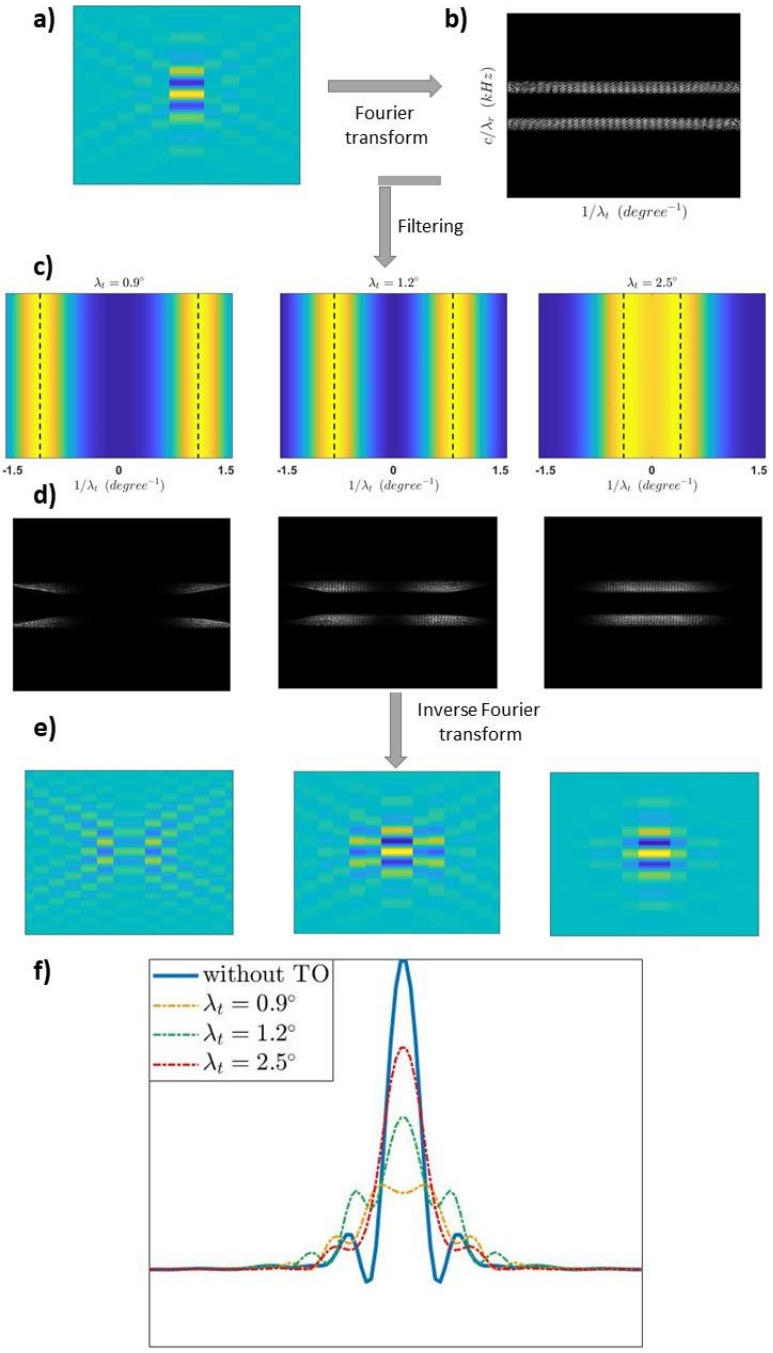

Figure 4.2: Pipeline of TO introduction by filtering in the Fourier domain showing the influence of λ_t, an example on a point spread function (PSF) a) simulated with Field II (J.A. Jensen and Svendsen 1992; J.A. Jensen 1996) positioned at (5cm,0°). First 2D Fourier transform is applied to the US image b). In c), three TO filters are displayed. The location of the two Gaussians depends on the TO desired wavelength. For education purpose three filters introducing different TO wavelengths are presented: λ_t equals form left to right $0.9°, 1.2°, 2.5°$. The spectrum resulting from b) and c) are displayed in d). The inverse Fourier transform is finally applied to obtain the TO US image. In e), the PSF are displayed. The tangential profiles of all the TO PSF are displayed in f). If the value of the TO wavelength is chosen too small, a high amount of noise is preserved after TO filtering and the lateral profile does not exhibit TO, as shown with $\lambda_t = 0.9°$. On the contrary, if the value of λ_t is too high ($\lambda_t = 2.5°$ in our example), the two Gaussians overlap in the TO filter and no TO is introduced. The TO wavelength should then be smartly chosen to lead to correct TO introduction, as shown by $\lambda_t = 1.2°$ in our case.

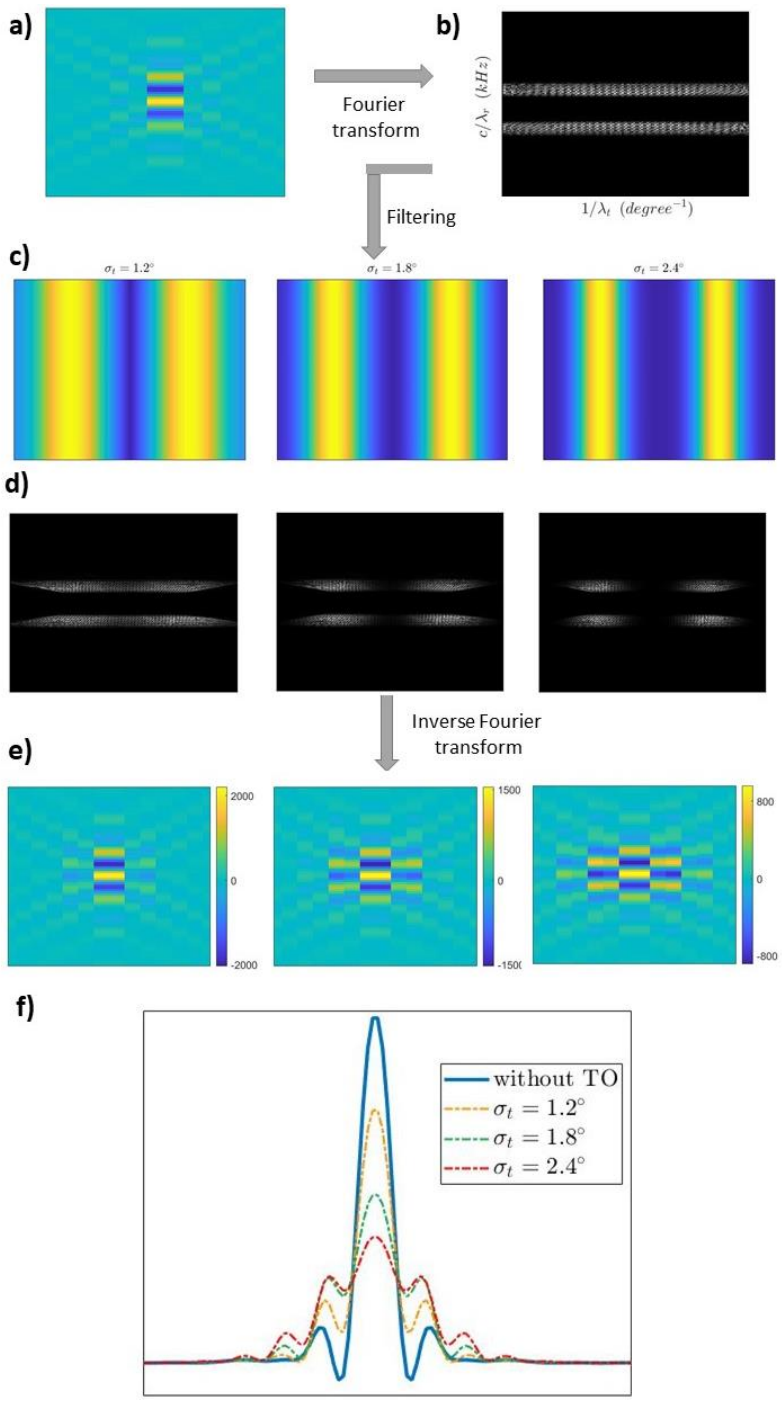

Figure 4.3: Pipeline of TO introduction by filtering in the Fourier domain showing the influence of σ_t, an example on a point spread function (PSF) a) simulated with Field II (J.A. Jensen and Svendsen 1992; J.A. Jensen 1996) positioned at (5cm,0°). First 2D Fourier transform is applied to the US image b). In c), three TO filters are displayed. The location of the two Gaussians depends on the TO desired wavelength, fixed here at 1.2°. The standard deviation σ_t of the two Gaussians affect how close they are to each other and how much signal is kept after TO filtering. For education purpose three filters introducing different σ_t are presented: σ_t equals form left to right 1.2°, 1.8°, 2.4°. The spectrum resulting from b) and c) are displayed in d). The inverse Fourier transform is finally applied to obtain the TO US image. In e), the PSF are displayed. The tangential profiles of all the TO PSF are displayed in f). If σ_t is chosen too small, the two Gaussians overlap in the TO filter and no TO is introduced. On the contrary, if the value of σ_t is too high ($\sigma_t = 2.4°$ in our example), a very small amount of the signal is preserved. TO will be present but with a low intensity. The standard deviation of the Gaussians should then be smartly chosen to lead to correct TO introduction with enough intensity for motion estimation, as shown by $\sigma_t = 1.8°$ in our case.

4.I.A.b Motion estimation algorithm

In Section 2.III.D, a 2D phase-based motion estimator was described for TO linear approaches. We use a similar approach applied to TO introduced in tangential with the use of a convex probe.

Let us consider a spatial point of polar coordinates $(t°, r)$ in the TO image, whose signal $s(t)$ can be written as:

$$s(t) = A(t)\cos(2\pi f_{t°}(t° + \Delta t°(t)))\cos(2\pi f_r(r + \Delta r(t))) \quad 4.2$$

where A is an amplitude term, $f_{t°}$ and f_r are respectively the tangential and radial spatial frequencies, and $\Delta t°$ and Δr are respectively the tangential and radial displacements.

Using the Hahn approach, we arbitrarily chose to extract the phase corresponding to the analytical signal of the two top regions i.e. to the negative axial and negative lateral frequencies, and the negative axial and positive lateral frequencies:

$$\begin{cases} \phi^I(t) = 2\pi f_{t°}\big(t° + \Delta t°(t)\big) + 2\pi f_r(r + \Delta r(t)) \\ \phi^{II}(t) = -2\pi f_{t°}\big(t° + \Delta t°(t)\big) + 2\pi f_r(r + \Delta r(t)) \end{cases} \quad 4.3$$

where ϕ^I and ϕ^{II} are the phases of the first and second analytic signals, respectively.

The phase shifts can be expressed as:

$$\begin{cases} \Delta\phi^I(t) = \phi^I(t+\tau) - \phi^I(t) \\ \Delta\phi^{II}(t) = \phi^{II}(t+\tau) - \phi^{II}(t) \end{cases} \Rightarrow \begin{cases} \Delta\phi^I(t) = 2\pi f_{t°}\Delta t°(t) + 2\pi f_r\Delta r(t) \\ \Delta\phi^{II}(t) = -2\pi f_{t°}\Delta t°(t) + 2\pi f_r\Delta r(t) \end{cases} \quad 4.4$$

where $\Delta\phi^I$ and $\Delta\phi^{II}$ are respectively the phase shifts from the first and second analytic signals; τ is an estimation lag and $\Delta t°$ and Δr are the displacement from t to $t + \tau$.

The displacements can then be obtained through:

$$\begin{cases} \Delta\mathrm{r(t)} = \dfrac{\Delta\phi^I(t) + \Delta\phi^{II}(t)}{4\pi f_r} \\ \Delta t°\mathrm{(t)} = \dfrac{\Delta\phi^I(t) - \Delta\phi^{II}(t)}{4\pi f_{t°}} \end{cases} \quad 4.5$$

The radial velocity v_r and tangential $v_{t°}$ velocity components will be obtained through the estimation of the phase shifts:

$$\begin{cases} \mathrm{v}_r = \dfrac{PRF\ c}{\tau}\ \dfrac{\Delta\hat{\phi}^I(t) + \Delta\hat{\phi}^{II}(t)}{4\pi f_r} \\ \mathrm{v}_{t°} = \dfrac{PRF\ c}{\tau}\ \dfrac{\Delta\hat{\phi}^I(t) - \Delta\hat{\phi}^{II}(t)}{4\pi f_{t°}} \end{cases} \quad 4.6$$

where $\Delta\hat{\phi}^I$ and $\Delta\hat{\phi}^{II}$ are respectively the estimated phase shifts from the first and second analytic signals.

Like in the 1D estimation, the velocity as a function of time can be recovered using a sliding window with a fixed ensemble length. The phase shifts can be estimated using the same estimator as Kasai *et al*. (Kasai et al. 1985):

$$\begin{cases} \Delta\hat{\phi}^I(\tau) = \tan^{-1}\left(\dfrac{\Im\{\hat{R}^I(\tau)\}}{\Re\{\hat{R}^I(\tau)\}}\right) \\ \Delta\hat{\phi}^{II}(\tau) = \tan^{-1}\left(\dfrac{\Im\{\hat{R}^{II}(\tau)\}}{\Re\{\hat{R}^{II}(\tau)\}}\right) \end{cases} \quad 4.7$$

where $\hat{R}^I$ and $\hat{R}^{II}$ are respectively the complex autocorrelation of the first and second analytic signals; $\Im$ and $\Re$ respectively the imaginary and real functions. Spatial filtering of the complex autocorrelation estimates can be performed before velocity estimation to reduce noise in the estimated phase shifts (Udesen and Jensen 2006).

The radial velocity v_r and the tangential velocity v_θ thus obtained are expressed in m/s and degree/s. The tangential motion is converted into m/s:

$$v_\theta(i,j)_{m/s} = sin\left(\frac{v_\theta(i,j)_{\circ/s}}{PRF}\right)(R + r_{i,j})\,PRF \qquad 4.8$$

where (i,j) denotes pixel coordinates and $r_{i,j}$ the radial distance of such pixel (as illustrated in Figure 1.19). R is the radius of the convex probe.

The tangential and radial velocities are projected into axial v_x and lateral v_z velocities:

$$\begin{cases} v_x(i,j) = v_r(i,j) \times \sin\left(\theta_{(i,j)}\right) + v_\theta(i,j)_{m/s} \times \cos\left(\theta_{(i,j)}\right) \\ v_z(i,j) = v_r(i,j) \times \sin\left(\theta_{(i,j)}\right) - v_\theta(i,j)_{m/s} \times \cos\left(\theta_{(i,j)}\right) \end{cases} \qquad 4.9$$

where $\theta_{i,j}$ denotes the polar angle of the pixel of coordinates (i,j).

After the axial and lateral velocities are recovered, an interpolation over a cartesian grid can be performed for visualization.

4.I.B Validation in Flow Simulation

Flow and tissue interaction is a particularly complex phenomenon still not perfectly understood. Simulation of both pulse wave propagation and flow is, hence, not a trivial matter. We decided to only consider flow motion for simulation validation. Tissue and flow motion estimation will be simultaneously validated *in vitro* in the following section 4.II.

A preliminary flow simulation has been conducted at the beginning of this thesis, resulting in a proceeding at *IEEE International Ultrasonics Symposium 2019* (Ghigo et al. 2019). The goal of this first simulation was a rough validation of TO introduction by Fourier filtering on a convex probe. A single diverging US wave was emitted by applying no delays to the probe's elements and a low Peak Systolic Velocity (PSV) was considered. The repeatability of the method was evaluated on several short simulations.

After the TO introduction was validated for a simple flow simulation, the optimized US sequence presented in Chapter 3 was implemented on a more advanced simulation. The PSV was here increased to a more realistic value of 140 cm/s.

For both simulations, a straight vessel of 2 cm radius at 7 cm depth was simulated with Field II (J. A. Jensen and Svendsen 1992; J. A. Jensen 1996b). The 7 cm depth has been chosen both in consistency with a mean descending AA depth and the conclusion of Section 3.II.

The vessel was set perpendicular to the probe axis. TO was then introduced as explained in Section 4.I.A, and motion was recovered with the 2D-phase based algorithm described in Section 4.I.A2.III.D. A spatial filtering of 1 mm (≈2 λ_0) in the radial direction and 1.8° ($^3/_2\,\lambda_t$) in the tangential direction was performed on the complex autocorrelation used to recover the phase shift (Eq. 4.7).

4.I.B.a Preliminary validation

The goal of this first simulation was a rough validation of TO introduction by Fourier filtering on a convex probe. The optimized US sequence presented in Chapter 3 is not implemented here, and only one diverging wave was emitted without any delays on the probe's elements with a PRF of 4kHz. Beamforming was achieved using a conventional DAS algorithm considering the elements positions and directivity (see Section 3.III). The simulation was performed 20 times over different set of scatterers for repeatability evaluation. For visualization purpose, the estimated velocities were finally interpolated over a Cartesian grid.

Table 4.I.1: Acquisition parameters - preliminary validation

Probe number of elements	128
Probe radius of curvature	R = 41.2 mm
Field of view	-37°/37°
Transmit frequency	f_0 = 3.125 MHz
Sampling frequency	12.5 MHz
Transmit burst	5-cycles
Pulse repetition frequency	PRF = 4000 Hz
Frame per second	FPS = 4000 Hz
Transmit apodization	Rectangular
Receive apodization	Rectangular
Transmit delays	None
Number of simulations	20
Number of frames per simulation	20
Number of scatterers per mm²	$\frac{1}{\lambda} \approx 2000$

Table 4.I.2: Acquisition parameters – secondary validation

Probe number of elements	192
Probe radius of curvature	R = 60.3 mm
Field of view	-30°/30°
Transmit frequency	f_0 = 3.5 MHz
Sampling frequency	14 MHz
Transmit burst	3-cycles
Pulse repetition frequency	PRF = 3000 Hz
Frame per second	FPS = 1000 Hz
Transmit apodization	Sliding Hanning on 128 elements
Receive apodization	Hanning
Transmit delays	Virtual sources placed on the half-radius
Number of simulations	1
Number of frames per simulation	60
Number of scatterers per mm²	$\frac{1}{\lambda} \approx 2200$

The convex probe simulated in this preliminary study was the C5-2 probe (Philips Healthcare, Andover, MA, USA), available on the PILoT platform using a Verasonics Vantage™ 256 system (Vantage 128, Verasonics Inc., Redmond, WA, US). The acquisition and probe parameters are detailed in Table 4.I.1.

4.I.B.b Secondary validation

The objective of this secondary validation is quite different from the first one. The goals were here to:

- simulate the compounding sequence described in the Chapter 3,
- simulate the CA631 probe (described in Table 3.I.1),
- assess a higher PSV more consistent with typical parameters observed when screening the AA.

A PRF of 3 kHz was used, in consistency with the inherent limit that will be faced during AA screenings as detailed in Section 3.II.A. This leads to a frame rate of 1 kHz due to the three sub-images used in compounding (Eq. 1.3). A PSV of 140 cm/s corresponding to a large PSV of an AA is simulated. One data set of 60 frames (i.e. 20 final compounded images) was simulated. The acquisition and simulation parameters are reported in Table 4.I.2.

4.I.B.a Transverse Oscillation parameters

Simulations are a good environment to test the influence of a method's parameters. Here, a study of the influence of the introduced spatial tangential frequency (f_t) and of the standard deviation of the Gaussian TO filter (σ_t) is presented in Figure 4.6. In this study, the tangential wavelength λ_t was fixed from 1° to 1.5° while σ_t varied from 1.6° to 2.2°, both in 0.1° steps. Flow velocity was estimated on the preliminary simulation. The Normal Root Mean Square Error (NRMSE) of the peak velocity was used as an accuracy marker. The minimum NRMSE (≈4%) is obtained when f_t=1.2° and.σ_t=1.8°, therefore these values are used in the following of this thesis. The obtained TO-PSF is displayed in the middle panel of Figure 4.2.b.

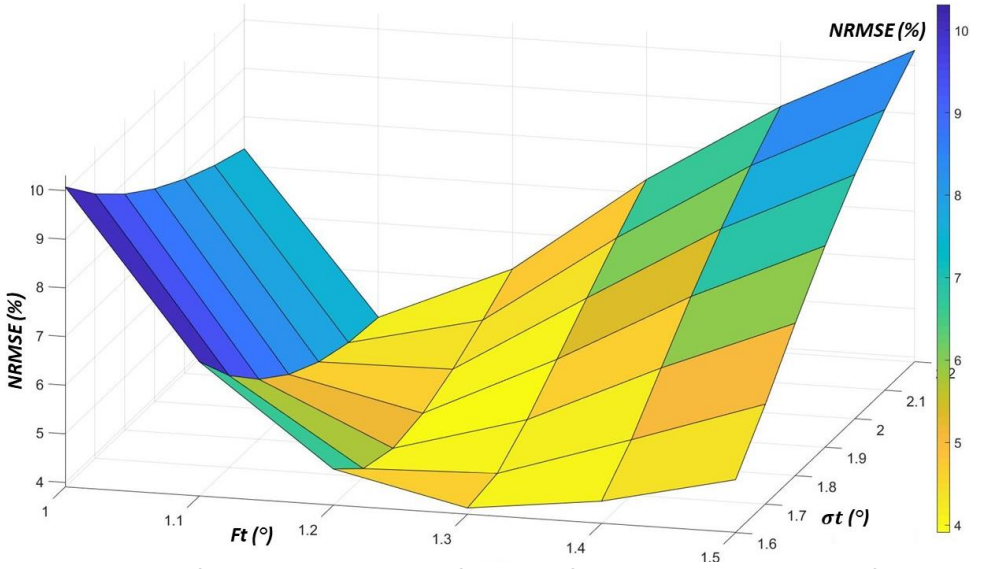

Figure 4.6: NRMSE error of the peak velocity as a function of the introduced tangential frequency (f_t) and the standard deviation (σ_t) of the Gaussian TO filter. The minimum NRMSE is obtained when f_t=1.2°

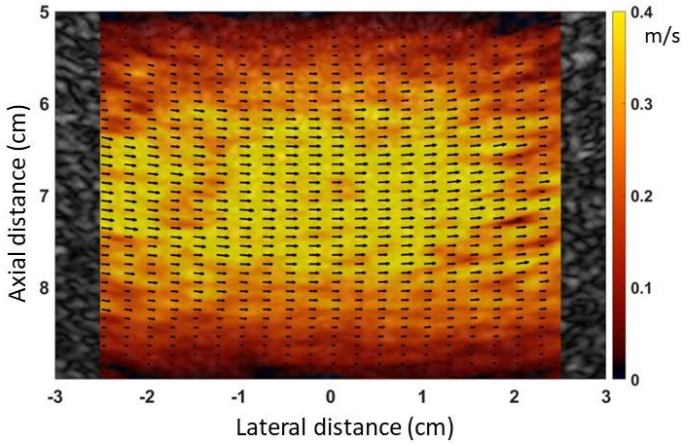

Figure 4.4: 2D flow velocity map of one of the simulated phantom superimposed on its B-mode image

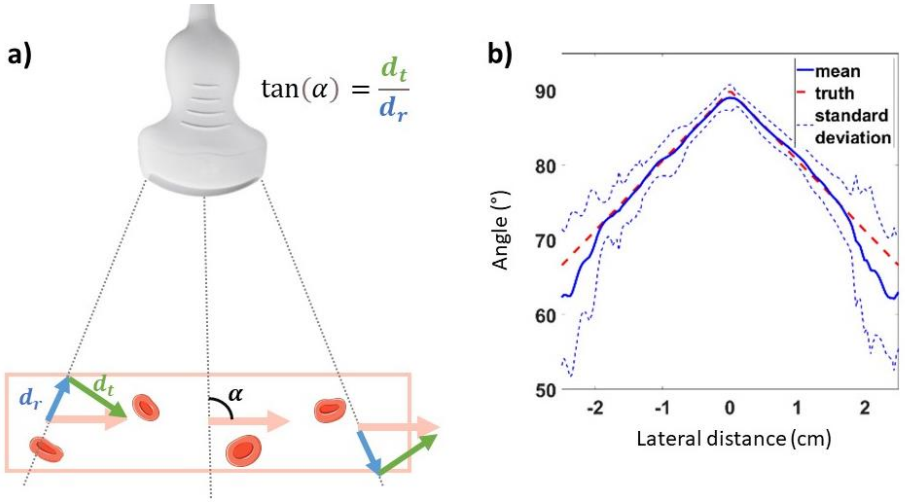

Figure 4.5: Mean absolute angle denoted α between the ultrasound beam and the blood flow: a) a schematic view and b) the estimated α for one simulation over the entire vessel height

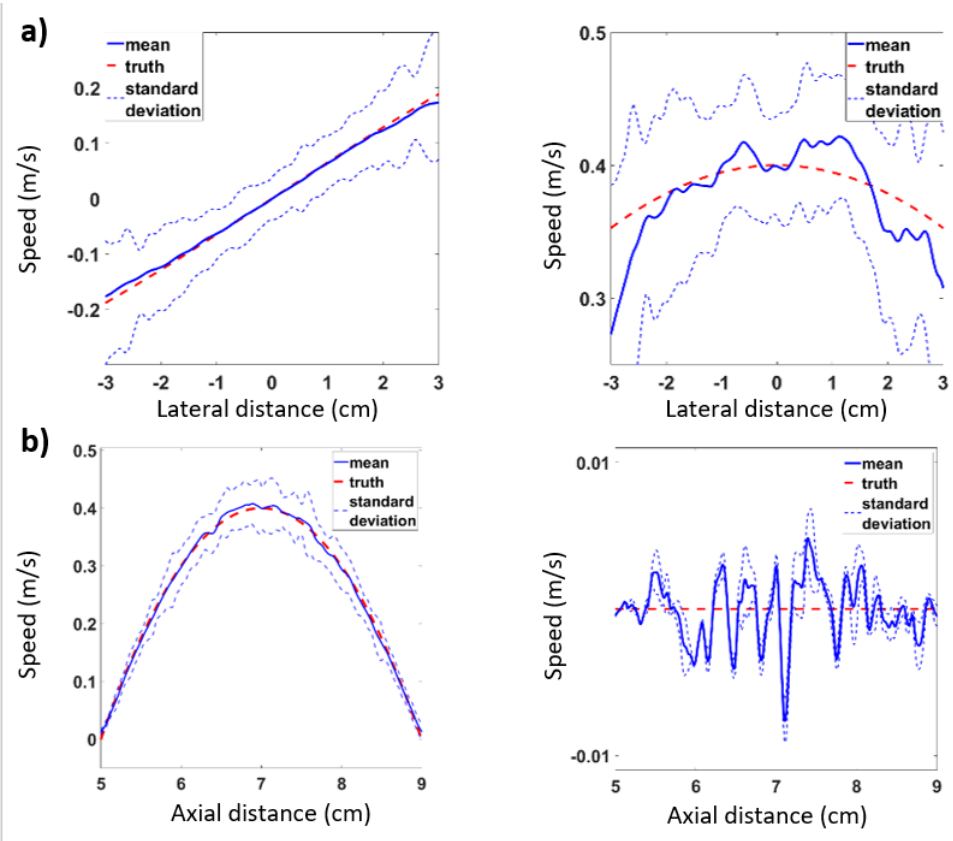

Figure 4.8: (a) radial (left) and tangential (right) velocities at the middle of the phantom (z = 7 cm) averaged on all simulations, the estimation loses in accuracy with the lateral distance due to loss of signals intensity and PSF orientation; (b) lateral (left) and axial (right) velocities inside the axial cut of the vessel phantom averaged on all simulations, the axial estimate has a maximum absolute value lower than 0.01 m/s, the lateral velocity is estimated with an NRMSE lower than 5%.

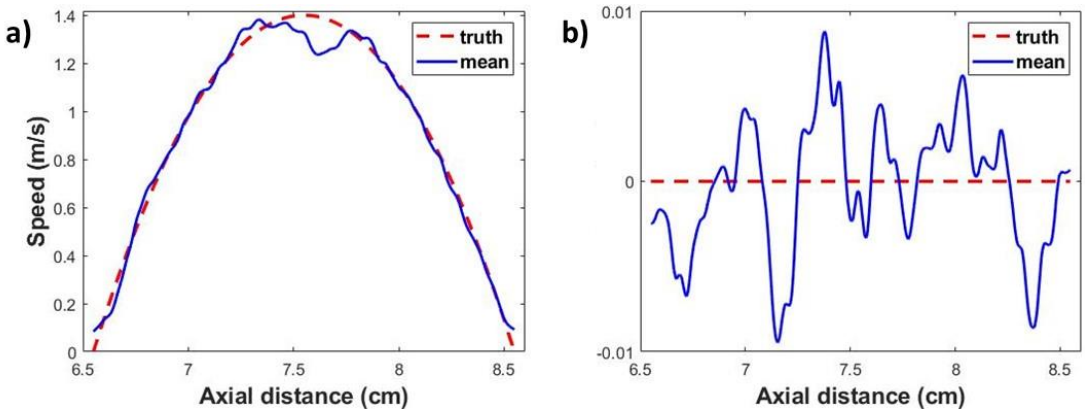

Figure 4.7: instantaneous (a) lateral and (b) axial velocities inside the axial cut of the second vessel phantom simulated. The axial estimate has a maximum absolute value lower than 0.01 m/s; the lateral velocity is estimated with an NRMSE lower than 4%.

4.I.B.b Results

Once the axial and lateral velocities are recovered for each frame (Eq. 4.9), the velocity field can be visualized as vectors that are typically superimposed to a color-coded velocities map. Figure 4.4 displays such a map for a frame of one simulation. Even if the results appear quite visually, small errors can be spotted. A temporal averaging is often performed to smooth the data.

Figure 4.8.a) shows the estimated radial (left) and tangential velocities (right) in the middle of the vessel average over all simulations. As expected, the estimation is more accurate alongside the propagation of the ultrasound beam (radial direction) where the oscillations are naturally present. The estimation accuracy is lower near the image edges due to a lack of signal and to the increase deformation of the PSF with the lateral distance. The FOV in which the tangential velocity can be estimated with a Normal Root Mean Square Error (NRMSE) lower than 8% of the peak velocity is equal to 5 cm. Radial and tangential velocities are important to study separately as the final axial and lateral velocities will depend on both values (Eq. 4.9). However, axial and lateral velocities are easier to understand as flow motion in the vessels tends to be mostly lateral.

Figure 4.8 b) shows the axial (left) and lateral (right) velocities over a 5 cm FOV averaged on all simulations. The lateral blood velocity is correctly recovered with an NRMSE lower than 5% of the peak velocity. The axial estimate has a maximum absolute value lower than 0.01 m/s.

Recovering the direction of the blood flow is of clinical importance and can be useful for detecting turbulent flow, assessing the vulnerability of the plaque (Stefanadis et al. 2017) etc. Figure 4.5 shows the absolute angle between the ultrasound beam and the estimated blood flow for one simulation The NRMSE is lower than 8% of the peak velocity over a 5 cm wide FOV.

The second simulation validates motion estimation with the use of our compounding sequence. In Figure 4.7, the lateral and axial velocities in the middle section of the phantom are displayed. The lateral velocity is recovered with a NRMSE lower than 4% of the PSV: large flow velocity can be recovered with good accuracy.

4.II In Vitro Experimentations

4.II.A Experimental set-up

Several PolyVinyl Alcohol (PVA) phantoms have been molded to mimic the AA using a 3D-printed mold. Pictures of the 3D-printed mold are shown in Figure 4.10. The dimension of the phantom (reported in Table 4.II.1 with the experiment conditions) approximate the real dimension of the visible part of the aorta during an ultrasound scan. (Lutz and Buscarini 2011). The phantom preparation was composed of PVA, silica and distilled water (10 %, 1 % and 89 % in weight, respectively). PVA acquires its mechanical properties by freeze-thaw cycles process: the higher the number of cycles, the higher the stiffness. One freeze-thaw cycle consists of a 12h freezing process during which the freezer is powered,

Table 4.II.1: Experimental conditions

Phantom length	15 cm
Phantom lumen diameter	14 mm
Wall thickness	2 mm
Valve opening duration	300 ms
Solenoid valve frequency	1 Hz
Number of freeze-thaw cycles	2, 3, 4, 5
Column height	1 m

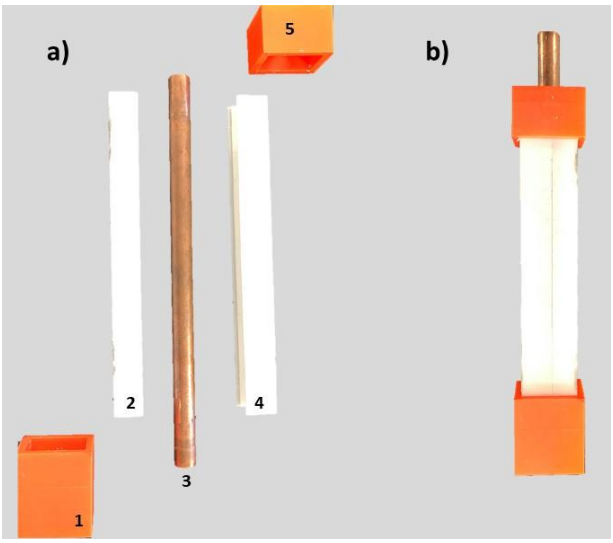

Figure 4.10: Pictures of a 3D-printed mold for phantom creation: a) disassembled: the mold is composed of a base (1) in which a metal bar (3) can be inserted. This bar corresponds to the vessel lumen Two printed parts, one female (2) and one (male) can be connected around the metal bar. The top part (5) is used to hold firmly in place the metal bar during the freeze-thaw process. b) the final assembled mold: the phantom preparation is gently poured in the gaps between the metal bar and the rest of the mold. The final phantom will have a lumen equal to the outer diameter of the metal bar and a walls thickness depending on the size of the gaps between the metal bar and the rest of the mold. Its length depends on the quantity of phantom

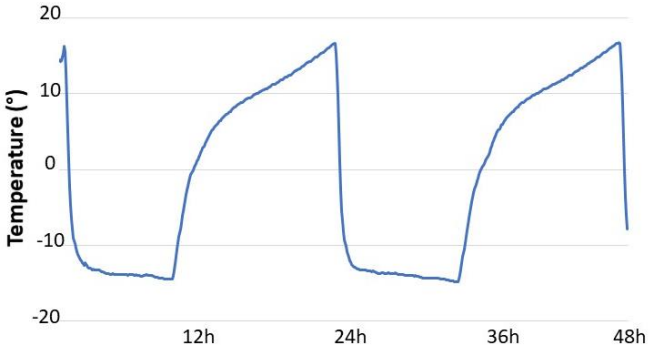

Figure 4.9: Change of temperature during two freeze-thaw cycles. One freeze-thaw cycle consists of a 12h freezing process during which the freezer is powered, and a 12h thawing process during which the freezer is unpowered.

and a 12h thawing process during which the freezer is unpowered. A temperature sensor has been placed inside the freezer for two freeze-thaw cycles to check its repeatability (Figure 4.9). Silica provides scatterers in the vessel wall and is responsible for the phantom echogenicity. The resulting phantoms are very close to biological tissues in terms of acoustic and mechanical characteristics (Fromageau et al. 2007). Finally, phantoms with four different number of freeze-thaw cycles (from 2 to 5) have been investigated. Two phantoms were produced for each freeze-thaw cycle for reproducibility measurements.

Blood Mimicking Fluid (BMF) was made with 5 µm Orgasol®, glycerol, surfactant and distilled water (2 %, 10 %, 1 % and 87 % in weight, respectively). Orgasol® provides scatterers, glycerol sets viscosity and surfactant ensures that the scattering particles are well dispersed into the fluid. The resulting BMF is in accordance with the standard physical and acoustic properties of blood (K. V. Ramnarine et al. 1998).

The presence of both a pulsatile flow and a pulse wave propagating along the phantom walls are needed for this experiment. A column filled with BMF is connected to the inlet of the phantom. A pump is used to keep constant the quantity (height) of BMF present in the column in order to obtain identical flow velocities during all experiments. The output of the phantom is connected to an open

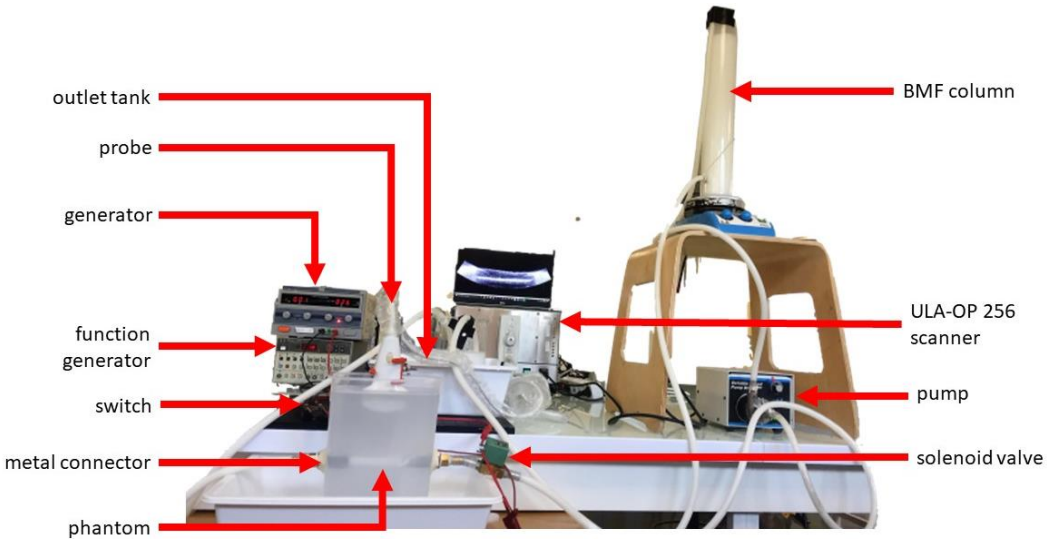

Figure 4.11: Picture of the experimental set-up: The column filled with BMF (blood mimicking fluid) is placed in height. The solenoid valve brutally opens due to the function generator alimenting the switch with a rectangular function. A pulse wave then propagates along the walls of the phantom, which is held in place by metal connectors. The BMF flows freely inside the outlet tank until the valve closes again. The height of the BFM is kept constant with a pump pumping back BMF from the tank outlet inside the column.

tank where BMF flows freely. A solenoid-valve, controlled by a function generator, is placed between the inlet and the pressure column to set the flow cycles. While the solenoid-valve is closed, no BMF is flowing through the set-up. The sudden opening of the valve creates a pulse wave that propagates along the phantom walls. While the valve is open, the flow runs freely inside the phantom until the valve closes again. The entire set-up is displayed in Figure 4.11.

The function generator controls the solenoid valve with two keys parameters: the repetition cycle and the duty cycle. The repetition cycle fixes at which frequency the solenoid valve opens. The duty cycle is the ratio of the high period to the total period of the rectangular wave sent by the function generator. The higher the duty cycle, the longer the opening duration of the valve will be.

This experimental set-up leads to flow motion and pulse wave propagation. First, flow estimation is validated. while keeping the solenoid valve open for quite long duration (1s) and the repetition cycle quite high (0.5 Hz). This allows for the flow to stabilize and be more easily validated. To demonstrate that our technique is suitable even when the vessel is angulated, acquisitions were made with a beam-to-flow angle of 90; 80, 70 and 30°. The resulting estimated flow is compared with a Doppler spectrum obtained in the same conditions with the clinical mode of an Ultrasonix MDP system. Then, the repetition cycle of the solenoid valve was set to 1 Hz, close to the frequency of a healthy beating heart. The solenoid valve was kept open during 100 ms. To validate more thoroughly our wall motion estimation technique, a linear probe (LA523 Esaote SpA, Italy) was used to acquired data in one phantom for each cycle. The PWV obtained with the linear probe, using the method described by Perrot et al. (Perrot et al. 2017; 2018), was then compared to those obtained on the data acquired with the convex probe.

The complexity of both flow and wall motion is quite high. Indeed, wave reflections tend to happen at the end of the phantom where metal connectors are placed. These reflections cause the movement of walls to be more complex, making wall velocity maps harder to interpret. Furthermore, strong backflow occurs, which is consistent with the strong backflow present in a human AA (Moore et al. 1994). This leads to complex flow patterns, such as the creation of vortices. Being able to visualize such phenomena is of medical interest but can be quite difficult to interpret.

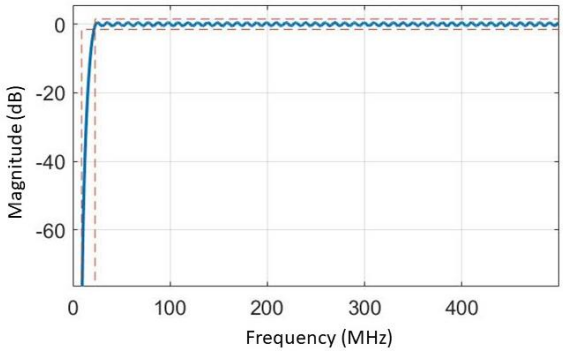

Figure 4.13: Magnitude spectrum of the Clutter filter used in this thesis.

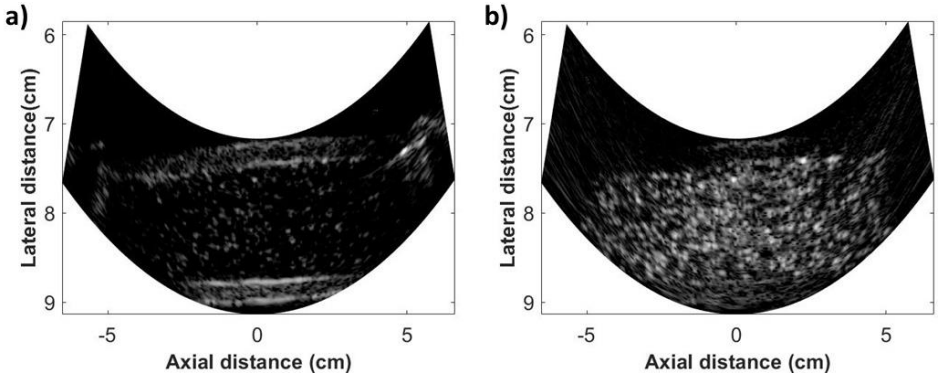

Figure 4.12: Effect of clutter filter on an US image before clutter filter a) and after b) both with a -20dB dynamic range. The scatterers are visually enhanced while the intensity of the walls is decreased. Flow estimation algorithm are usually used after clutter filter.

4.II.B Data Acquisition and processing pipeline

Data were acquired with the same material and parameters as in the compounding study (Section 3.II): a ULA-OP 256 scanner (Boni et al. 2016) and a CA631 Esaote SpA convex probe (Table 3.I.1). The phantom was immersed in water and imaged by the probe along its longitudinal axis at a depth of around 7 cm. Data were acquired during a total time of 3 s to save at least two entire opening/closing valve cycles. This procedure is repeated three times for each phantom. As two phantoms of each freeze/thaw cycles (2, 3, 4, 5) are investigated, a total of 24 acquisitions were realized. The pulse wave propagation happens at the very beginning of a cycle when the solenoid-valve brutally opens. Therefore, the entire propagation of at least two pulse waves is captured during each acquisition.

After data acquisition, TO was first introduced for tissue motion assessment. A clutter filter was then applied to the acquired beamformed data, before TO was introduced for flow estimation. An equiripple FIR clutter filter of order 200 was applied to the beamformed data to separate flow from tissue signal (Figure 4.13). The effect of clutter filter is displayed in Figure 4.12.

The radial oscillation due to ultrasound has a wavelength of $\lambda_r \approx 0$ 5 mm. Transverse oscillation was introduced with a wavelength of $\lambda_t = 1.2°$. The ensemble length was set to 128 frames. Spatial averaging was performed onto the complex autocorrelation estimates to reduce noise in the velocity estimation, a 2D rectangular window of size 2 mm per 1.8° was used.

Once the 2D velocity map is obtained, the velocity of the upper wall is extracted by manually selecting its position on the first frame. No tracking of the wall position was performed here as the maximum displacement of the wall is less than half its thickness. Wall and flow velocities can then be displayed and analyzed. An illustration of the entire pipeline is available in Figure 4.14.

For assessing the pulse wave velocity (PWV), the wall velocity map is first estimated displaying the estimated velocities inside of the wall as a function of time. The pulse wave propagation can be directly visualized on this map, as the pic of motion tissue will first reach the left side of the vessel's walls before the right side (or vice versa). The estimation of the pulse wave velocity (PWV) was performed on the acceleration of the wall for increased robustness. By linear regression on the maximum of acceleration, the PWV can be recovered. A first regression was performed, and outliers were then identified if their distance to the initial fit was higher than the standard deviation (Figure 4.15). Another linear regression is performed without the outliers. The slope of this line gives PWV.

Strong reflections tend to occur on the metal connectors holding the phantom in place. These reflections make the assessment of the PWV very complex. However, as strong reflections are also known to occur *in vivo* in the AA, specifically at the bifurcation of AA and other blood vessels, such as the renal arteries. Being able to extract PWV in complex conditions in phantoms is then a good indicator of transferability of the technique *in vivo.* The radon transform, here denoted R, can be used to reduce the impact of such reflections:

$$R\big(a_w(w,t)\big) = \int_{-\infty}^{+\infty} a_w(w(k), t(k))\, dk \qquad 4.10$$

where a_w is the acceleration in the vessel's wall, a function depending on the position along the wall w and on the time t. The radon transform is then truncated to conserve only the forward propagating waves, as illustrated in Figure 4.16. If the forward wave is coming from the left, the first half of the columns of R are preserved while a decreasing weight function is used to lower the presence of waves propagating from the right; and vice versa if the forward wave is coming from the right. The inverse radon transform is then applied to obtain an acceleration map where backward propagating waves are less apparent. It is on this acceleration map that the final PWV will be estimated.

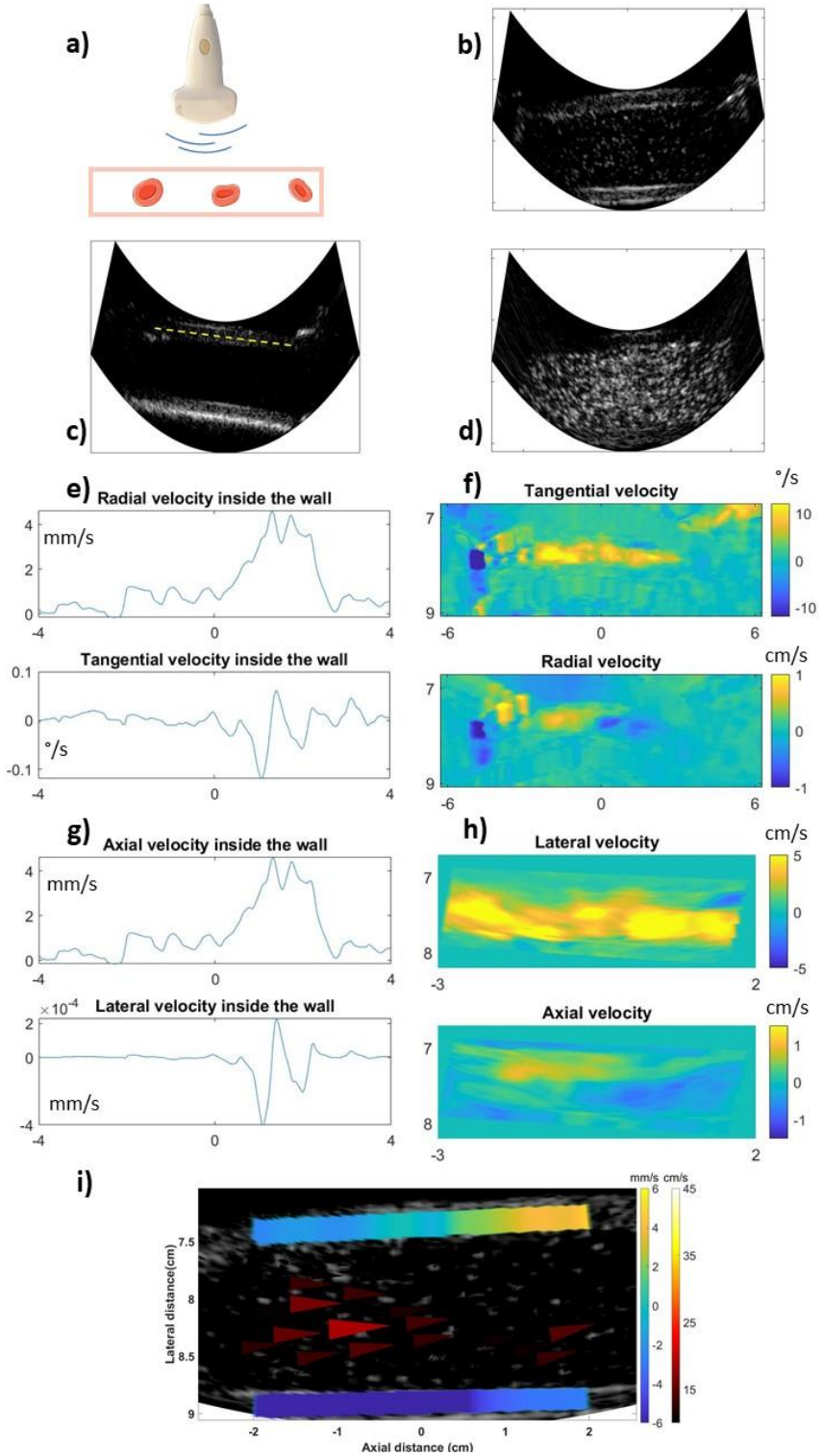

Figure 4.14: Illustration of the entire pipeline for simultaneous flow and tissue motion estimations. First, the ultrasound sequence developed in chapter 3 is used to acquire the data a). Then beamforming is performed to obtain the ultrasound images c).

For tissue motion estimation, the position of the wall is first manually fixed d). The radial and tangential velocities inside the wall can then be estimated e) and converted into axial and lateral velocities g).

For flow estimation, clutter filter is applied before motion estimation d). Tangential and radial velocities are then estimated f) and can then be converted into axial and lateral velocities h). A mask is manually drawn and applied to only display the velocities inside the lumen.

Finally, flow and tissue information are superimposed onto a B-mode image i).

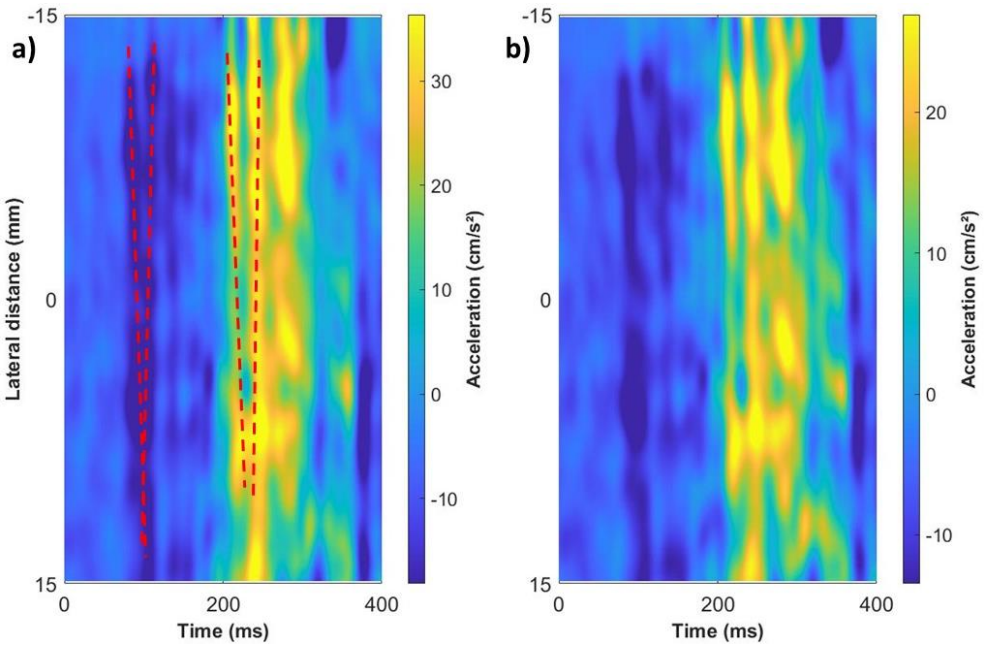

Figure 4.16: Illustration of the influence of reflected waves occurring at the phantom's connectors. In a), V-shape structures can be observed corresponding to the forward propagating wave first followed by its reflected wave propagating in the other direction. After a careful Radon transform b), only the forward propagating waves can be preserved and later use for PWV estimation.

4.II.C Results

4.II.C.a Flow assessment

First, the flow assessment was validated with different beam-to-flow angle on a 5-freeze-thaw cycles phantom. The solenoid valve was kept open during one second and kept close during one second also (i.e. set-up repetition cycle of 2 Hz). This long open/close time allows for the flow to well stabilize inside the phantom, making the study of the flow easier. The angle between the flow direction (considered parallel to the vessel's walls) and the US beam of the middle element of the probe was set to 90°, 80°, 70° and 30° by tilting the convex probe. A spectrum Doppler acquired with a linear probe L14-5W on a Ultrasonix MDP clinical scanner was use as reference (Figure 4.17.a). The same ROI used for the clinical spectrum Doppler (in blue) was considered and the minimum and maximum flow patterns in this ROI are displayed in Figure 4.17.b,c,d,e. The shape of the flow is well extracted with all beam-to-flow angles. The peak systolic flow velocity magnitude, i.e. the maximum velocity estimated in the ROI, was of 41.2, 48.8, 45.6 and 43.3 cm/s for 90, 80, 70 and 30° beam-to-flow respectively, which was in good agreement with the one obtained by the clinical scanner (48.2 cm/s). One of the main issues was the strong backscattered echoes due to the phantom's metal connector. When the beam-to-flow angle is of 0°, the connectors are out of the field of view of the probe, but when the probe is tilted the connectors become apparent and deteriorate greatly the image quality. As TO have been developed for estimating transverse motion. It is hence recommended not to increase the beam-to-flow angle more than 60°.

4.II.C.b Pulse wave velocity according to phantom's stiffness

An example of PWV estimation is displayed in Figure 4.15. Here the same set-up condition as the flow study was used (solenoid valve opened for one second, closed for one second i.e. set-up repetition cycle of 2 Hz) in order for the multiple wave reflections to stabilize. All PWV extracted with our method are presented in Figure 4.18. The PWV median are 1.26, 1.94, 2.47, 3.61 m/s for respectively the 2, 3,

4 and 5 freeze-thaw cycles. This tendency of increasing PWV with the number of freeze-thaw cycles and hence, phantom rigidity was expected. To further validate our results, PWV were also estimated with a linear probe. The PWV medians obtained a with a linear probe are 1.42, 2.30, 2.47 and 3.81 for respectively the 2, 3, 4 and 5 freeze-thaw cycle m/s. The resulting PWV estimated with a convex and linear probe are in good accordance, validating our estimating tissue motion algorithm.

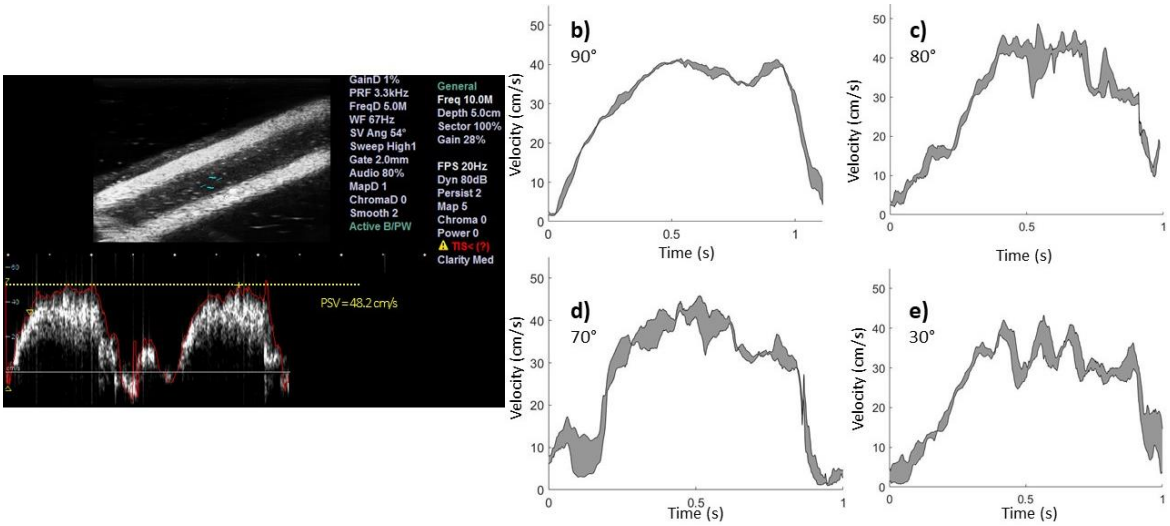

Figure 4.17: a) Doppler spectrum obtained with a linear probe on a Ultrasonix MDP clinical scanner; Minimum and maximum estimated velocity in the same ROI as in a) with varying beam-to-flow angle of 90°, 80°, 70° and 30° respectively displayed in b), c), d) and e). The beam-to-flow angle with the convex probe is defined between the central ultrasound beam and the vessel.

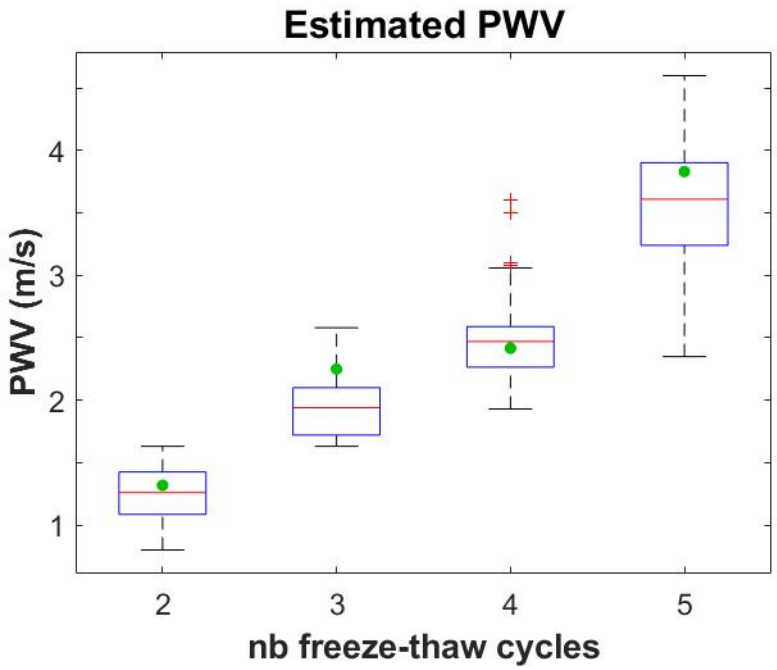

Figure 4.18: Boxplots of the estimated PWV according to the number of freeze-thaw cycles of the phantoms using a convex probe. The median is represented by the red line. The blue box contains the data from the 25th to the 75th percentile. The maximum and minimum PWV are represented by the black lines. Data considered as outliers (outside of 99.3% coverage) are displayed as red crosses. The median PWV estimated with a linear probe is represented by green dots. As expected, the estimated PWV increases with the phantom's rigidity (freeze-thaw cycles). The PWV obtained with a convex and a linear probe are in accordance, proving that the PWV estimation in convex geometry is correct.

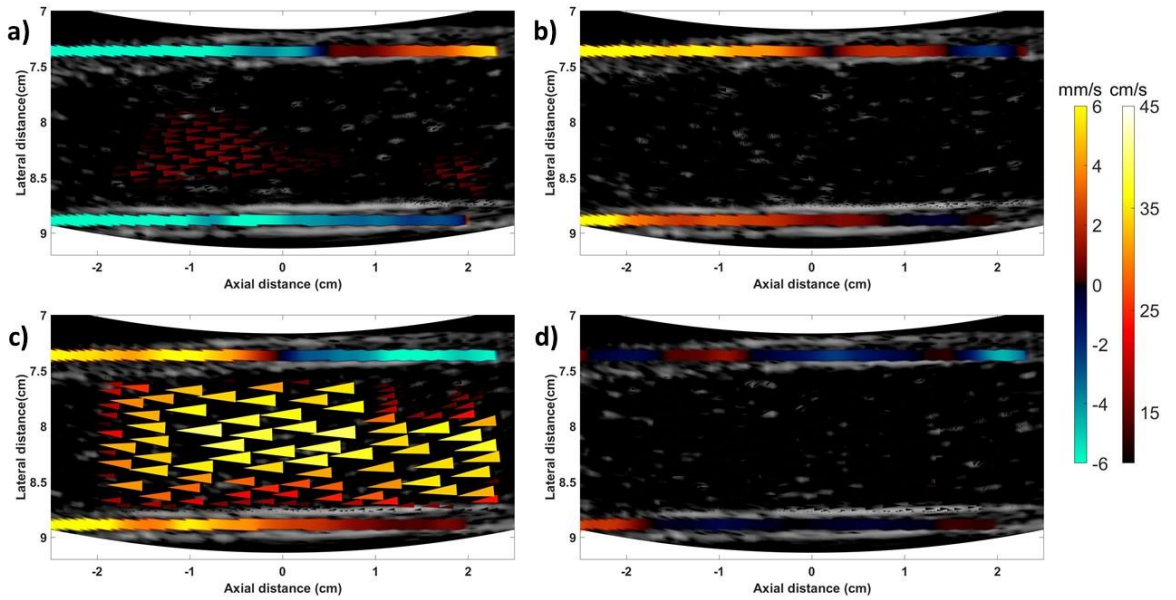

Figure 4.19: Four snapshots of the wall and flow velocities at 100 ms (a), 108 ms (b), 530 ms (c) and 1410 ms (d) after the beginning of an acquisition. Wall velocity is expressed in mm/s while flow velocity is displayed in cm/s. (a), (b) show the pulse wave arriving from the right part of the phantom. (c) corresponds to the time when the flow is maximum at the center of the lumen. (d) corresponds to the return to calm where no flow is occurring. Some wave reflections are still propagating along the phantom's walls but with very low intensity. Here the solenoid valve was kept open during one second.

4.II.C.c Flow and tissue motion

The method allows to directly visualize flow and tissue motion simultaneously as displayed in Figure 4.19. Here, the goal was to place ourselves in the most physiological condition possible in our set-up. The repetition cycle of the set-up was set to 1 Hz, close to a healthy heartbeat cycle. The solenoid valve was kept opened during 100 ms. The propagation of the pulse wave can be visualized in Figure 4.19.a.b. As expected, the wall and flow have different properties. Concerning the velocities, the wall is subject to a maximum velocity of around 6 mm/s while the maximum flow velocity is around 40 cm/s. The maximum wall velocity and the maximum flow velocity are delayed in time. In fact, the maximum wall velocity can be seen at the beginning of the acquisition when the solenoid valve opens, and the pulse wave crosses the phantom (Figure 4.19.a b). During the propagation of the pulse wave the backflow from the previous cycle is still occurring at low velocity. Indeed, the maximum estimated velocity profile is noticeable at 530 ms (Figure 4.19.c). The algorithm can extract a large range of velocities which is vital for simultaneously quantifying wall and flow. In addition, the method extracts vector velocities as required for wall and flow study.

4.II.D Discussion and *in vivo* perspectives

In this chapter, an approach permitting to introduce TO in the f-k spectrum with a convex probe has been described. The flow and tissue motion were extracted simultaneously, and lateral and axial velocities could be recovered for visualization and better understanding of flow patterns. The propagation of the pulse wave and vector flow imaging can be assessed and visualized. The developed imaging modality is expected to provide additional insight in studying abdominal aorta biomechanics and other vessels imaged with convex probes.

Validation on *in vitro* phantoms can be quite tricky. The method's performance was investigated through experiments on several phantoms mimicking the geometry of a large vessel with different

elasticities. Different beam-to-flow angles were investigated for flow estimation, with the use of clinical Doppler spectrum as a gold standard. The method has been validated for both tissue and flow motion imaging.

Some technical limitations occurred in the experimental set-up. Using a solenoid valve creates a strong pulse wave propagating along the vessel's walls. However, when the solenoid valve is closed, no flow propagates in the phantom. One solution may be to use a programmable pump furnishing a large range of available velocities, but this option is quite costly. The use of a simple water column generates lower flow velocity values as compared to those in a physiological abdominal aorta. Theoretically, it is always possible to place the water column higher to increase the pressure on the solenoid valve and obtain higher PSV. However, this is highly impractical. In the future of the set-up, we plan to apply a pressure at the top of the water's column to obtain higher PSV.

In our set-up, the phantoms were only immersed in water. This is particularly useful when several phantoms need to be investigated as it facilitates placement of another phantom on the set-up. However, strong pulse wave reflections are generated at the outlet of the phantom and greatly complicates pulse wave velocity assessment. Surrounding the phantoms with mimicking tissue would attenuate such reflections. Nevertheless, on an *in vivo* abdominal aorta, strong reflections are known to occur typically at the renal arteries. Being able to extract a pulse wave velocity in complex conditions is needed for *in vivo* extraction.

Since the method is now validated, the next stage is to validate the approach *in vivo* and to determine the feasibility in a clinical environment. For *in vivo* experiments, safety parameters assessment is necessary in order to protect the patient from possible side effects of US, such as a burn of the superficial skin or even deeper tissues. In the next chapter, some safety parameters of the developed compounding scheme (Section 3.II) are assessed. A preliminary *in vivo* study is also performed on a healthy volunteer.

Chapter 5: *In vivo* preliminary study

When a novel ultrasound technique is developed, it cannot be directly applied to patients before several safety parameters are assessed and approved by the regulation authorities. The entire validation process is quite time consuming and requires numerous measurements and administrative processes. In this chapter, only preliminary safety parameters were measured to ensure that no bubble cavitation will occur during the ultrasound acquisition.

In this chapter, the technique developed in Chapter 4 is applied to a healthy volunteer. The flow patterns along with the motions of the walls were successfully extracted and visualized. The method is hence validated for a clinical study where the abdominal aortas of patients and healthy volunteers should be screened.

5.I Safety parameters

Two safety parameters were assessed using a hydrophone Onda HGL-0200. The ULA-OP 256, when emitting, was triggering an oscilloscope that recovered the acoustic signal received by the hydrophone. The CA631 convex probe's elements were barely immersed in a water tank. The hydrophone was inside the water tank and could be mechanically displaced by a DC motor-driven translation bench (Owis, Germany). The water was neither filtered nor degassed but was left stagnant for 4 hours prior to measurements in order to limit the amount of bubbles present. A picture of the set-up is shown in Figure 5.1, and was developed by (Bernard et al. 2020).

We decided to focus on the acquisition of two main safety parameters:

1. The Spatial Peak Temporal Average Intensity, denoted I_{spta}, is the temporal average intensity, calculated at the position of the spatial maximum,
2. The Mechanical Index denoted MI, gives an estimation of the likelihood of inertial cavitation.

In our case, we do not want any cavitation to occur, and the intensity received at any point should not be harmful. We decided to perform the safety measurement only on the central wave of our compounding emission described in Section 3.II:

- A Hanning window was applied only on the 128 center elements of the probe.
- The delays were calculated with the use of a virtual source located at $(0, -{}^{R}/_{2})$ with R being the radius of the probe.

The Pulse Repetition Frequency PRF was kept equal to 3 kHz. The excitation signal was composed of 3 cycles at a 3.5 MHz frequency.

The safety parameters were assessed following the guidelines of (Rodriguez-Molares 2017).
Before any measurement, the alignment between the probe and the hydrophone was checked and corrected using the scanner and oscilloscope displays. Then, the axial region in front of the probe was scanned with a 0.5 mm resolution step. For each point along the beam axis, the Pulse Pressure squared Integral, denoted PPI, was calculated with:

$$PPI(z) = \int_0^T p^2(z,t)\, dt \qquad 5.1$$

Where $p(z,t)$ is the instantaneous acoustic pressure measured at a depth z along the US beam (in our case, in front of the probe), and T is a time larger than the sum of the time-of-flight and the pulse duration to ensure that the whole acoustic signal is considered.
The derated Pulse Intensity Integral PII can then be computed:

$$PII(z) = \frac{PPI(z)}{\rho\, c} 10^{\left(-\alpha\, z\, f_0 / 10\right)} \qquad 5.2$$

Where ρ is the water's density, c is the speed of sound in water, α is the acoustic attenuation coefficient of our tank's water, and f_0 is the frequency of the emitted acoustic wave. The acoustic attenuation coefficient depends on the water's temperature T_w. In our case, $T_w = 22°$ leading to $\alpha = 3.10^{-5}\ dB/(m.Hz)$. The speed of sound in water is usually considered as equal to 1540 m/s. ρ is taken equal to 997 kg/m³.

We can finally access the derated time-averaged intensity integral using:

$$I_{spta}(z) = PRF\ PII \qquad 5.3$$

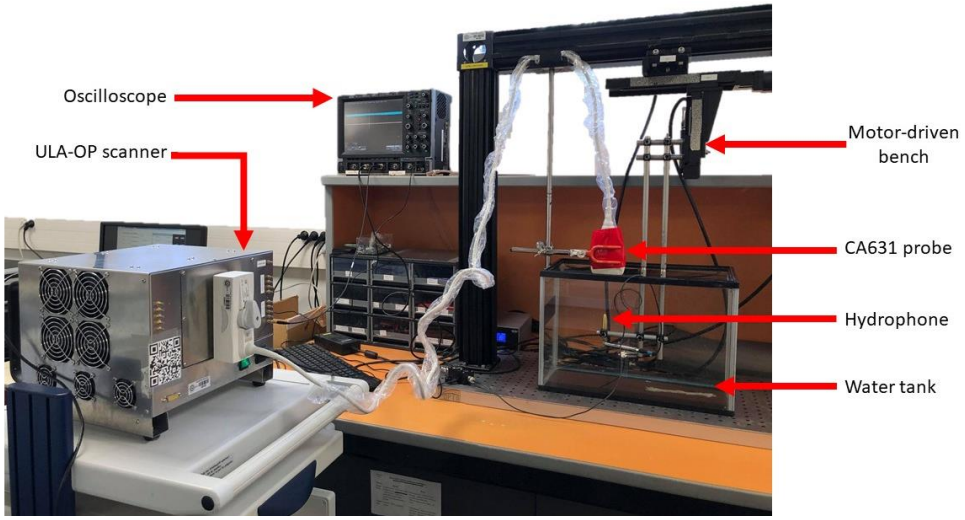

Figure 5.1: Experimental set-up for safety parameters measurement.

The maximum pressure recorded by the hydrophone in front of the probe is obtained at a 8 cm depth, denoted z_{max}, and is pictured in Figure 5.2. Finding z_{max} equal to 8 cm seems coherent with the use of our delays and the geometrical focus at 6.5 cm on the probe. At this depth, the PPI of approximately 8.46.105 Pa²/s with Eq. 5.1, leading to PII of 0.12 J.m^{-2} (Eq. 5.2). We therefore obtain a I_{stpa} approximately equal to 37.3 mW.cm $^{-2}$.

To assess the Mechanical Index, first the derated peak-rarefactional pressure, denoted p_r, must be recovered with:

$$p_r = \min\big(p(z_{max}, t)\big)\ 10^{\left(-\alpha\, z_{max}\, f_0/_{20}\right)} \qquad 5.4$$

MI was then obtained as stated in Section GG.2.2 of ("Particular Requirements for the Safety of Ultrasonic Medical Diagnostic and Monitoring Equipment" 2015):

$$MI = \begin{cases} abs(p_r)/\sqrt{f_0}, & f_0 < 4\ MHz \\ abs(p_r)/2, & f_0 \geq 4\ MHz \end{cases} \qquad 5.5$$

Using Eq. 5.4 and the signal $p(z_{max}, t)$ displayed in Figure 5.2, we found a derated peak-rarefactional pressure approximately equal to -0.365 Pa. As, in our case, $f_0 < 4MHz$, we obtain a Mechanical Index $MI \approx 0.18$.

Following the guidelines of the US Food and Drug Administration (FDA) (O'Leary and Vaezy 2019), for an ultrasound abdominal application, the derated time-averaged intensity integral I_{spta} should not exceed 94 mW.cm^{-2}, while the Mechanical Index should not exceed 1.9 for all non-ophthalmic use.

As in our case, $I_{spta} \approx 37.3\ \mathrm{mW.cm^{-2}}$ and $MI \approx 0.18$, we are well below the safety limits recommended by the FDA. An acquisition *in vivo* can be performed on a healthy volunteer without risk.

In this case, temperature measurements were not performed. As the AA of the volunteer is first localized using a conventional B-mode sequence, the safety is assured for this step. Then, the US sequence is changed to the one described in Chapter 3 and data are recorded for two seconds. As soon as those two seconds are over, the probe is lifted from the volunteer's body. For such a limited amount of time, the temperature rise can be considered negligible and not dangerous for the volunteer.

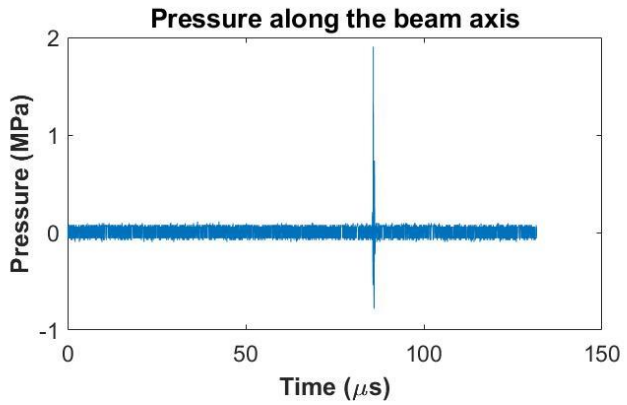

Figure 5.2: Maximum pressure recorded by the hydrophone in front of the probe, at a 8 cm depth.

5.II *In vivo* acquisition

5.II.A Material and methods

The ULA-OP 256 scanner (Boni et al. 2016) and the CA631 convex probe (Esaote SpA, Italy) (Table 3.I.1) were used for the *in vivo* acquisition. The written consent of the healthy volunteer participating in the study has been obtained before the examination. Using the compounding sequence described in chapter 3, the abdominal aorta was screened, and data were recorded for a total of 2 seconds with a PRF of 3 kHz. The volunteer was asked to hold their breath for the duration of the scan. The acquisition parameters are displayed in Table 5.II.2.

The pipeline used for the extraction of both tissue motion and flow is the one presented in chapter 4 (Figure 4.14) with the estimation parameters in Table 5.II.1.

A B-mode image of the volunteer's AA is displayed in Figure 5.3. The AA can be seen as being quite shallow, compared to the strong assumption made for the typical depth of an AA considered as 20 cm deep in Eq 3.1. This can be explained as the volunteer is young (25 years old), and slim with a minor amount of abdominal fat. In this case, it could be possible to increase either the framerate or the number of frames to be compounded. Nevertheless, it is necessary to keep in mind, that typical screenings of the AA in clinics are performed on patients around 65 years old that tend to have a non-negligeable amount of abdominal fat. The US sequence and method, presented in this thesis, were purposefully developed with the objective to study those patients.

Table 5.II.2: Acquisition parameters

Probe	Table 3.I.1
Transmit frequency	3.5 MHz
Sampling frequency	19.5 MHz
Valve opening duration	300 ms
Transmit pulse	3 cycles
PRF	1000 kHz
Acquisition duration	2 s
F-number	Figure 3.8

Table 5.II.1: Estimation parameters

TO wavelength	1.2°
FWHM of TO	1.8°
Ensemble length	128 frames
Valve opening duration	300 ms
Transmit pulse	3 cycles
PRF	1000 kHz
Spatial window	Rectangular
Spatial window size	2 mm × 1.8°

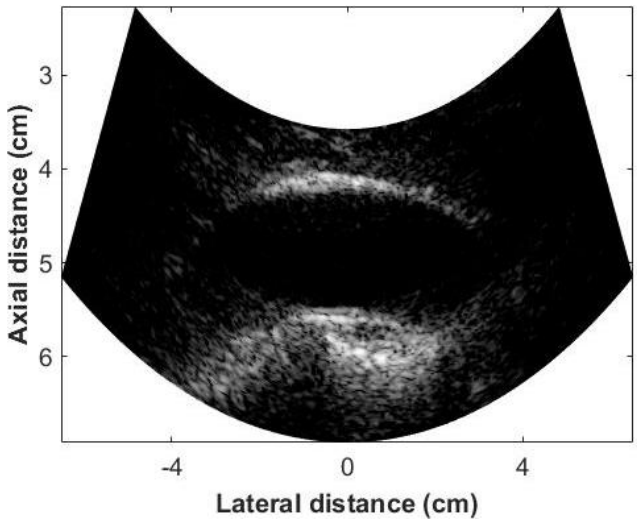

Figure 5.3: B-mode image of the Abdominal Aorta (AA). Below the AA, the presence of the spine can be seen causing some shadowing in the image.

5.II.B Results

The approach permits to do qualitative inspection due to the simultaneous wall and flow velocity measurements. Indeed, it becomes possible to study and visualize both characteristics at the same time. An example of visualization is showed in Figure 5.4. Flow is mainly parabolic during the systolic phase and the presence of strong backflow can be observed as expected in the lower part of the AA. The upper wall presents strong motion, both in dilatation and compression, whereas the lower wall is limited in its motion by the presence of the spine.

The PWV can then be extracted from the upper wall motion as illustrated in Figure 5.5. The velocity of the upper wall was extracted (Figure 5.5.a) by manual selection. The acceleration was then obtained (Figure 5.5.b) before applying the Radon transform to reduce the influence of reflected waves (Figure 5.5.c). The PWV was estimated by linear regression (Figure 5.5.d.e). In Figure 5.5.f, the velocity, acceleration, and relative displacement of the middle point of the upper wall are displayed. The PWV were estimated when the vessel was either fully dilated or during its compression, leading to PWV of 2.9 and 2.6 m/s respectively. It is coherent to find a higher PWV when the vessel was fully dilated than during compression. These PWV values are in the lower range of those typically found in the literature:

- On 5 healthy volunteers of 29±2 years old: 3.73±0.19 m/s (Luo et al. 2008)
- On 11 healthy volunteers of 28.9±3.3 years old: 4.4±0.6 m/s (J. Vappou, Luo, and Konofagou 2010)
- On 15 healthy volunteers of 32.5±10.2 years old: 6.03±1.68 m/s (R. X. Li et al. 2013)
- On 10 healthy volunteers of 24.8±3.3 years old: 5.43±1.78 m/s (R. X. Li, Qaqish, and Konofagou 2015)
- On 76 healthy volunteers between 23 and 71 years old: 4.58±1.38 m/s (Huang, Guo, et al. 2016)

Several potential factors can explain why the estimated PWV is lower than could be expected with the literature. First, the volunteer was female, and it has been shown that sex hormones play a non-negligible role on arterial stiffness (DuPont et al. 2019). Premenopausal women tend to have lower PWV than men of the same age. Furthermore, the volunteer was 25 years old, and as arterial rigidity increases with age, the PWV of the volunteer was expected to be quite low.

The axial displacement of the middle of the upper wall is illustrated in Figure 5.6.a and is fairly reproducible in three cardiac cycles displayed. The velocity in the lumen is also displayed in Figure 5.6.b for one cardiac cycle. The PSV can be assessed and is here of around 120 cm/s. Strong backflow of around 60 cm/s also occurs as expected.

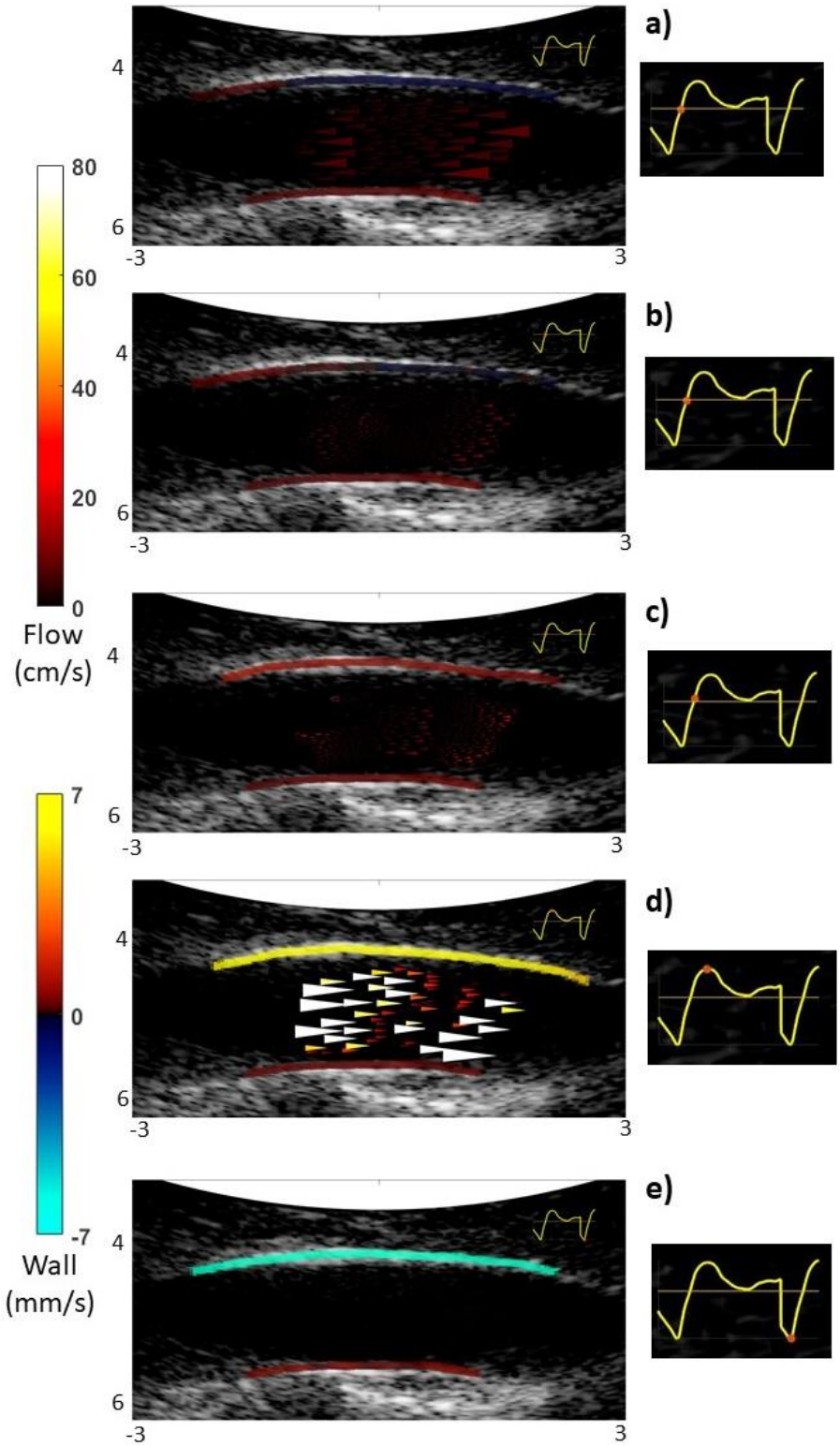

Figure 5.4: Flow and tissue velocity estimates superimposed onto B-mode images with the axial and lateral distance in cm. In (a,b,c), the pulse wave can be seen propagating form the left to the right of the upper wall (148,150,155 ms). During the pulse wave propagation, backflow is present. At the systolic peak d) (230 ms), both the upper wall motion and flow are maximal. When the upper wall motion is minimum e) (620 ms), flow is present at a very low intensity (< 10 cm/s). On the right of each B-mode images, the velocity at the middle of the upper wall is displayed as a function of time, with the horizontal line as a reference for 0.

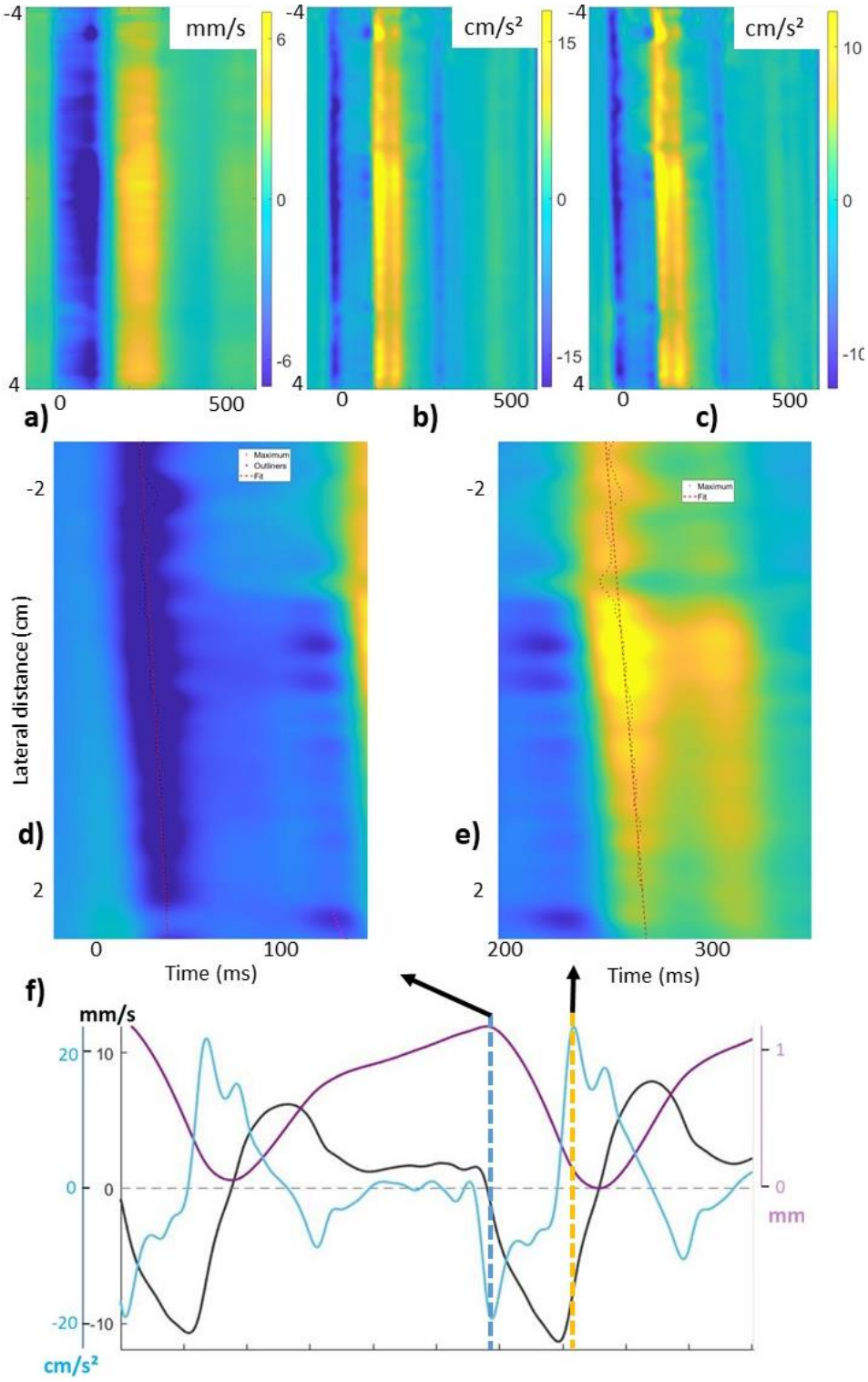

Figure 5.5: Study of the motion of the upper wall. a) Velocity at the middle point of the upper wall during a cardiac cycle, and b) its acceleration. After a Radon transform to preserve only the forward waves c), the PWV can be estimated on two distinct acceleration signs: a negative d) and positive one a).
The values of the PWV are of 2.89 and 2.59 m/s with a coefficient of determination of 0.94 and 0.89 for the negative and positive acceleration respectively.
In f), the velocity, acceleration, and relative displacement of the middle point of the upper wall are displayed in black, blue, and purple respectively. The time corresponding to the minimum and maximum of acceleration used in d) and e) are highlighted by a blue and a yellow dotted line. The PWV are easier to extract at those instants when the vessel is fully dilated d) and during the compression of the vessel e).

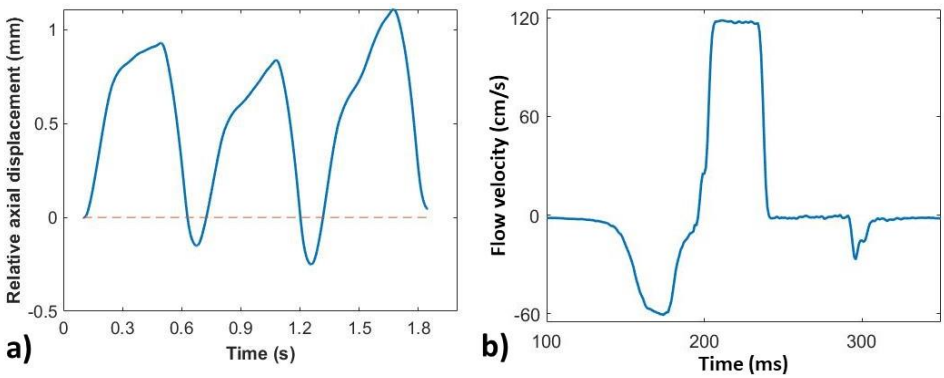

Figure 5.6: a) Relative axial displacement of the middle point of the upper wall during three cardiac cycles. b) Profile of the flow velocity in the middle of the lumen during one cardiac cycle. The Peak Systolic velocity is around 120 m /s, while the maximum velocity of the backflow is around 60 cm/s.

5.II.A Discussion and opportunities

The feasibility of simultaneous measurement of the vessel wall and blood flow velocities was investigated in one healthy volunteer at a high frame rate. Displaying 2D-vectors allow visualizing flow patterns with more details compared to conventional color Doppler imaging where only one component of the velocity can be extracted. The technique could also be used for the detection of unusual wall motion. Indeed, the method was able to highlight the behavior of the lower wall, which is blocked by the spine. The peak systolic velocity and the pulse wave velocity were successfully extracted on an *in vivo* AA.

Several aspects can be criticized. First, due to a lack of time, only one acquisition on one volunteer was processed. For reproducibility aspects, several acquisitions on the same volunteer should be acquired in the same conditions to show the consistency of the extracted flow and wall parameters. Further advanced parameters could be extracted, particularly on the flow, such as the Wall Shear Rate. A constant clutter filter was used in this study. An adaptative clutter filter whose cut-off adapts to the intensity of the tissue motion during the heart cycle could lead to better results, especially on a diseased patient.

Overall, this study has shown the feasibility of the investigated methods on an *in vivo* healthy AA using a research scanner. Future work should include more acquisitions on both healthy and diseased patients to precisely evaluate the potential clinical benefits. Indeed, the next stage is to evaluate if combining flow and wall motion estimates will lead to better detection of high-risk profiles and assist the clinician in the vulnerability assessment of the aneurysm to decide if a surgical treatment is appropriate. Depending on the benefits, closer collaborations with clinicians must be established to evaluate the feasibility of a potential application of this technique in clinical routine.

Conclusion and Perspectives

The cardiovascular system has a complex behavior and can be subject to pathologies such as aneurysms or plaques. The formation of such diseases is still not entirely understood, and they can stay asymptomatic until they result in sudden death. Detecting these diseases at an early stage greatly improves the patient's welfare and survival rate. If the disease is declared and visible, continuous monitoring is needed, and clinical intervention might be performed if judged necessary. Ultrasound is a good modality to detect, monitor and assess the severity of vascular pathologies, as it is non-invasive, non-ionizing, and ultrasound images are obtained in real-time at a relatively low-cost. Pathological markers can be extracted based on, on one hand, the aspect of the ultrasound images and, on the other hand, the velocity information estimated from these images. Being able to simultaneously extract both flow and tissue velocity seems highly relevant to better understand, detect and monitor vascular diseases. A good temporal resolution gives access to advanced parameters, such as pulse wave velocity, and captures fast and complex phenomena that can occur in arteries.

In this thesis, a technique able to provide high frame rate ultrasound imaging with both vectorial flow and wall motion estimates of deep vessels imaged with a convex probe was presented. An ultrasound sequence was specifically designed to assess deep tissues with a high frame rate, and was presented at the conference IEEE IUS 2020 (Ghigo et al. 2020). A transverse oscillations approach working in the Fourier domain was then adapted to the use of a convex probe, allowing the extraction of 2D-velocity maps. A validation of this method on the blood flow in simulation was presented at the conference IEEE IUS 2019 (Ghigo et al. 2019). An experimental set-up where a pulse wave was generated along with flow motion was developed. Validation was performed on several phantoms of abdominal aortas with different rigidities. Flow patterns and pulse wave velocities were in accordance with the expected values. A journal article on these results is currently being drafted. To further validate this work, an acquisition was realized on a healthy volunteer's abdominal aorta. Even *in vivo*, the flow and tissue motions were successfully extracted.

Like any research work, this thesis has certain limitations and points that could have been further developed. First, during this work, only the transverse oscillation technique was used, and no comparison with other estimation techniques was performed. The choice of the transverse oscillation technique was guided by the laboratory's past work and the fact that the method had already been validated for tissue and flow simultaneously with a linear probe. However, it does not mean that other methods could not have similar or even better results. Furthermore, TO parameters should be carefully chosen as they have a deep impact on the estimates' quality. For each convex probe of different parameters, an optimal range of introduced transverse frequencies should be studied. For the CA631 probe of Esaote SpA, we advise to use a TO frequency between 1 and 1.3°. As flow and wall motion have different properties, it could be useful to use two different TO frequencies to extract both motions, as sometimes done with a linear probe (Perrot, Ekroll, et al. 2021). Here, the same TO frequency of 1.2° has been used and has resulted in relevant estimations both on flow and wall motion. In this study, the TO wavelength was chosen manually trying to keep the most energetic part

of the frequency spectrum. The influences of the TO wavelength and the standard deviation of the Gaussian TO filter were studied on a flow simulation. This can be considered as a limitation of the presented method.

Validation of simultaneous wall and flow assessment have been performed *in vitro* without prior use of simulation validation. Indeed, flow/wall interactions are extremely complex, and no available simulation methods seemed to be easily available.

The study of an optimal compounding emission scheme described in Chapter 3 responded specifically to the issue of improving the final image quality using only three sub-images to compound with the CA631 probe. The best compounded emission in our case was to send three diverging waves with delays fixed by virtual sources (VS) placed on the half-radius of the probe and using for transmit apodization a 128-sliding Hanning window. If another convex probe needs to be used, the space between the VS leading to the best final image will probably change.

In Chapter 5, some preliminary safety measurements with our proposed emission scheme were realized. This safety test is not complete, and some safety indexes were purposefully not measured, such as temperature measurements due to a lack of time. Furthermore, the time needed for acquisition is limited to two seconds in this case, and the temperature rise can be considered negligible for such a limited time.

In this thesis, the same clutter filter was used for the entire heart cycle. An adaptative clutter filter whose cut-off changes in function of the tissue's intensity could lead to better results, especially on a diseased patient.

Perspectives include a more extensive study of safety parameters that could lead to a clinical proof of concept, where healthy and diseased abdominal aorta should be considered. Advanced parameters accessible by our method (such as pulse wave velocity, mean wall shear rate, peak wall shear rate) should be extracted. Coupled with statistical tests, it will make it possible to accurately measure the interest and contribution of the method for the detection of pathologies.

The use of a 1D-probe generates several limitations and issues. The placement of the probe is particularly crucial for a conventional probe, and this increases drastically the inter and intra operator inconsistency. The use of a matrix probe for 3D ultrasound imaging would permit to get rid of these placement issues and of out-of-plane motion. However, 3D ultrasound is still confronted to some major technical issues: the size of the elements makes it difficult to get a good signal-to-noise ratio and the high number of elements gives a high computation cost for signal and image processing. Furthermore, their small footprint does not seem appropriate for abdominal scans.

In the future, we hope this thesis can give precious information on the formation process of vascular diseases in deep vessels, which remain unclear nowadays. New information on flow and tissue interaction might be useful for theoretical behavior of the artery model, in order to predict the evolution of the artery.

Personal contribution

Published article

B. Harbaoui, N. Ghigo, L. Boussel, H. Liebgott, G. Souteyrand, E. Durand, H. Eltchaninoff, T. Lefevre, PY Courand and P. Lantelme, “Prognostic significance of vascular and valvular calcifications in low- and high-gradient aortic stenosis”. Eur Heart J Cardiovasc Imaging. 2021. doi: 10.1093/ehjci/jeab039. Epub ahead of print. PMID: 33693609.

Article in progress

“Simultaneous pulse wave and flow velocity estimation with high frame rate ultrasound imaging with based on a convex array: a phantom study” – currently being written

International poster presentations with proceedings

N. Ghigo, A. Ramalli, S. Ricci, P. Tortoli, D. Vray and H. Liebgott, "Sequence optimization for high frame rate imaging with a convex array," *2020 IEEE International Ultrasonics Symposium (IUS)*, 2020, pp. 1-4, doi: 10.1109/IUS46767.2020.9251286.

N. Ghigo, V. Perrot, B. Harbaoui, A. Long, S. Ricci, P. Tortoli, D. Vray and H. Liebgott, "High Frame Rate Vector Flow Imaging with a Convex Array in a simulated vessel phantom," *2019 IEEE International Ultrasonics Symposium (IUS)*, 2019, pp. 356-359, doi: 10.1109/ULTSYM.2019.8925612.

International oral presentations without proceedings

N. Ghigo, V. Perrot, S. Ricci, P. Tortoli, D. Vray and H. Liebgott, “Ultrafast ultrasound imaging of the flow and tissues motions in the abdominal aorta using a convex probe”, Artimino conference, Nijmegen Netherlands, 2019

International invited talk without proceedings

H. Liebgott, V. Perrot, N. Ghigo, S. Salles, I. K. Ekroll, A. Ramalli, J. Avdal, E. Boni, F. Varray, L. Petrusca, A. Bernard, A. Long, B. Harbaoui, P. Tortoli, L. Løvstakken, and D. Vray, “High frame rate ultrasound imaging of the arteries,” in 2019 International Congress on Ultrasonics (ICU), Sep. 2019.

National oral presentations without proceedings

V. Perrot, N. Ghigo, L. Petrusca, A. Bernard, S. Salles, A. Long, B. Harbaoui, F. Varray, D. Vray, and H. Liebgott, “Imagerie ultrasonore ultra-rapide de l’artère carotide,” in 2019 Recherche en Imagerie et Technologies pour la Santé (RITS), Oct. 2019.

N. Ghigo, H. Liebgott, D. Vray, “Ultrafast Ultrasound Imaging for Simultaneous 2D Wall and Flow Motion of the Abdominal Aorta”, Team building day LabTAU, Lyon, Jun. 2020.

N. Ghigo, “Un diagnostic en 10 millisecondes : ce que votre cœur dit de vous en 8 battements”, Journée d’étude organisée par le projet junior “Effets de temps”, Maison International de la Langue et de la Culture, Lyon, janvier 2020.

Bibliography

Ahlgren, A. R., S. Steen, S. Segstedt, T. Erlöv, K. Lindström, T. Sjöberg, H. W. Persson, S. Ricci, P. Tortoli, and M. Cinthio. 2015. "Profound Increase in Longitudinal Displacements of the Porcine Carotid Artery Wall Can Take Place Independently of Wall Shear Stress: A Continuation Report." *Ultrasound in Medicine & Biology* 41 (5): 1342–53. https://doi.org/10.1016/j.ultrasmedbio.2015.01.005.

Aizawa, K., S. Sbragi, A. Ramalli, P. Tortoli, F. Casanova, C. Morizzo, C. E. Thorn, A. C. Shore, P. E. Gates, and C. Palombo. 2018. "Brachial Artery Vasodilatory Response and Wall Shear Rate Determined by Multigate Doppler in a Healthy Young Cohort." *Journal of Applied Physiology* 124 (1): 150–59. https://doi.org/10.1152/japplphysiol.00310.2017.

Amirbekian, V., M. Lipinski, J. Frias, S. Amirbekian, K. Briley, V. Mani, D. Samber, et al. 2009. "MR Imaging of Human Atherosclerosis Using Immunomicelles Molecularly Targeted to Macrophages." *Journal of Cardiovascular Magnetic Resonance* 11 (S1): 151–52. https://doi.org/10.1186/1532-429X-11-S1-O3.

Anderson, M.E. 1998. "Multi-Dimensional Velocity Estimation with Ultrasound Using Spatial Quadrature." *IEEE Transactions on Ultrasonics, Ferroelectrics and Frequency Control* 45 (3): 852–61. https://doi.org/10.1109/58.677757.

Apostolakis, I. Z., P. Nauleau, C. Papadacci, M. D. McGarry, and E. E. Konofagou. 2017. "Feasibility and Validation of 4-D Pulse Wave Imaging in Phantoms and In Vivo." *IEEE Transactions on Ultrasonics, Ferroelectrics, and Frequency Control* 64 (9): 1305–17. https://doi.org/10.1109/TUFFC.2017.2735381.

Azimi, M., and A. C. Kak. 1985. "An Analytical Study of Doppler Ultrasound Systems." *Ultrasonic Imaging* 7 (1): 1–48. https://doi.org/10.1016/0161-7346(85)90014-8.

Badescu, E., H. Liebgott, D. Garcia, P. Joos, Adeline Bernard, L. Augeul, R. Ferrera, M. Viallon, L. Petrusca, and D. Friboulet. 2019. "Comparison Between Multiline Transmission and Diverging Wave Imaging: Assessment of Image Quality and Motion Estimation Accuracy." *IEEE Transactions on Ultrasonics, Ferroelectrics, and Frequency Control* 66 (10): 1560–72. https://doi.org/10.1109/TUFFC.2019.2925581.

Baker, C. 1970. "Pulsed Ultrasonic Doppler Blood-Flow Sensing." *IEEE Transactions on Sonics and Ultrasonics* SU-17 (3): 170–85. https://doi.org/10.1016/0041-624x(70)91188-1.

Balocco, S., O. Basset, G. Courbebaisse, E. Boni, A. F. Frangi, P. Tortoli, and C. Cachard. 2010. "Estimation of the Viscoelastic Properties of Vessel Walls Using a Computational Model and Doppler Ultrasound." *Physics in Medicine and Biology* 55 (12): 3557–75. https://doi.org/10.1088/0031-9155/55/12/019.

Bambi, G., T. Morganti, S. Ricci, E. Boni, F. Guidi, C. Palombo, and P. Tortoli. 2004. "A Novel Ultrasound Instrument for Investigation of Arterial Mechanics." *Ultrasonics* 42 (1–9): 731–37. https://doi.org/10.1016/j.ultras.2003.11.008.

Baraldi, P., A. Sarti, C. Lamberti, A. Prandini, and F. Sgallari. 1996. "Evaluation of Differential Optical Flow Techniques on Synthesized Echo Images." *IEEE Transactions on Biomedical Engineering* 43 (3): 259–72. https://doi.org/10.1109/10.486283.

Basarab, A., P. Gueth, H. Liebgott, and P. Delachartre. 2009. "Phase-Based Block Matching Applied to Motion Estimation with Unconventional Beamforming Strategies." *IEEE Transactions on*

Ultrasonics, Ferroelectrics and Frequency Control 56 (5): 945–57. https://doi.org/10.1109/TUFFC.2009.1127.

Basarab, A., H. Liebgott, F. Morestin, A. Lyshchik, T. Higashi, R. Asato, and P. Delachartre. 2008. "A Method for Vector Displacement Estimation with Ultrasound Imaging and Its Application for Thyroid Nodular Disease." *Medical Image Analysis* 12 (3): 259–74. https://doi.org/10.1016/j.media.2007.10.007.

Benthin, M., P. Dahl, R. Ruzicka, and K. Lindström. 1991. "Calculation of Pulse-Wave Velocity Using Cross Correlation—Effects of Reflexes in the Arterial Tree." *Ultrasound in Medicine & Biology* 17 (5): 461–69. https://doi.org/10.1016/0301-5629(91)90182-V.

Bernard, A., L. Petrusca, D. Vray, H. Liebgott, P. Muleki Seya, and G. Grenier. 2020. "Development of an Experimental Setup for Safety Assessments of New Ultrasound Imaging Modes," 8 pages. https://doi.org/10.48465/FA.2020.0248.

Besson, A., F. Wintzenrieth, B. Heriard-Dubreuil, and C. Cohen-Bacrie. 2020. "On Archimedean-Spiral-Based Imaging." In *2020 IEEE International Ultrasonics Symposium (IUS)*, 1–4. Las Vegas, NV, USA: IEEE. https://doi.org/10.1109/IUS46767.2020.9251833.

Bohs, L. N., and G. E. Trahey. 1991. "A Novel Method for Angle Independent Ultrasonic Imaging of Blood Flow and Tissue Motion." *IEEE Transactions on Biomedical Engineering* 38 (3): 280–86. https://doi.org/10.1109/10.133210.

Bolondi, L., S. Gaiani, and L. Barbara. 1991. "Accuracy and Reproducibility of Portal Flow Measurement by Doppler US." *Journal of Hepatology* 13 (3): 269–73. https://doi.org/10.1016/0168-8278(91)90067-L.

Boni, Enrico, Luca Bassi, Alessandro Dallai, Francesco Guidi, Valentino Meacci, Alessandro Ramalli, Stefano Ricci, and Piero Tortoli. 2016. "ULA-OP 256: A 256-Channel Open Scanner for Development and Real-Time Implementation of New Ultrasound Methods." *IEEE Transactions on Ultrasonics, Ferroelectrics, and Frequency Control* 63 (10): 1488–95. https://doi.org/10.1109/TUFFC.2016.2566920.

Bonnefous, O., and P. Pesqué. 1986. "Time Domain Formulation of Pulse-Doppler Ultrasound and Blood Velocity Estimation by Cross Correlation." *Ultrasonic Imaging* 8 (2): 73–85. https://doi.org/10.1016/0161-7346(86)90001-5.

Brandt, A. H. 2017. "Evaluation of New Ultrasound Techniques for Clinical Imaging in Selected Liver and Vascular Applications." University of Copenhagen.

Brandt, A. H., K. L. Hansen, M. B. Nielsen, and J. A. Jensen. 2015. "Velocity Estimation of the Main Portal Vein with Transverse Oscillation." In *2015 IEEE International Ultrasonics Symposium (IUS)*, 1–4. Taipei, Taiwan: IEEE. https://doi.org/10.1109/ULTSYM.2015.0068.

Bruneel, C., R. Torguet, K. M. Rouvaen, E. Bridoux, and B. Nongaillard. 1977. "Ultrafast Echotomographic System Using Optical Processing of Ultrasonic Signals." *Appl. Phys. Lett.* 30 (8): 371–73. https://doi.org/10.1063/1.89436.

Buck, T., R. A. Mucci, J. L. Guerrero, G. Holmvang, M. D. Handschumacher, and R. A. Levine. 2000. "Flow Quantification in Valvular Heart Disease Based on the Integral of Backscattered Acoustic Power Using Doppler Ultrasound." *Proceedings of the IEEE* 88 (3): 307–30. https://doi.org/10.1109/5.838068.

Bulow, T., and G. Sommer. 2001. "Hypercomplex Signals-a Novel Extension of the Analytic Signal to the Multidimensional Case." *IEEE Transactions on Signal Processing* 49 (11): 2844–52. https://doi.org/10.1109/78.960432.

Chen, Y., J. D'hooge, and J. Luo. 2018. "Doppler-Based Motion Compensation Strategies for 3-D Diverging Wave Compounding and Multiplane-Transmit Beamforming: A Simulation Study." *IEEE Transactions on Ultrasonics, Ferroelectrics, and Frequency Control* 65 (9): 1631–42. https://doi.org/10.1109/TUFFC.2018.2851310.

Chong, T., L. Nguyen, C. D. Owens, M. S. Conte, and M. Belkin. 2009. "Suprarenal Aortic Cross-Clamp Position: A Reappraisal of Its Effects on Outcomes for Open Abdominal Aortic Aneurysm

Repair." *Journal of Vascular Surgery* 49 (4): 873–80. https://doi.org/10.1016/j.jvs.2008.10.057.

Chun, K. C., K. J. Dolan, H. C. Smothers, Z. T. Irwin, R. C. Anderson, A. L. Gonzalves, and E. S. Lee. 2019. "The 10-Year Outcomes of a Regional Abdominal Aortic Aneurysm Screening Program." *Journal of Vascular Surgery* 70 (4): 1123–29. https://doi.org/10.1016/j.jvs.2019.01.053.

Cinthio, M, A.R. Ahlgren, T. Jansson, A Eriksson, H.W. Persson, and K. Lindström. 2005. "Evaluation of an Ultrasonic Echo-Tracking Method for Measurements of Arterial Wall Movements in Two Dimensions." *IEEE Transactions on Ultrasonics, Ferroelectrics, and Frequency Control* 52 (8): 1300–1311. https://doi.org/10.1109/TUFFC.2005.1509788.

Couade, M., M. Pernot, E. Messas, J. Emmerich, A. Hagège, M. Fink, and M. Tanter. 2011. "Ultrafast Imaging of the Arterial Pulse Wave." *IRBM* 32 (2): 106–8. https://doi.org/10.1016/j.irbm.2011.01.012.

Couture, O., M. Fink, and M. Tanter. 2012. "Ultrasound Contrast Plane Wave Imaging." *IEEE Transactions on Ultrasonics, Ferroelectrics and Frequency Control* 59 (12): 6373790. https://doi.org/10.1109/TUFFC.2012.2508.

Deplano, V., Y. Knapp, L. Bailly, and E. Bertrand. 2014. "Flow of a Blood Analogue Fluid in a Compliant Abdominal Aortic Aneurysm Model_ Experimental Modelling." *Journal of Biomechanics* 47 (6): 1262–69.

Deplano, V., C. Meyer, C. Guivier-Curien, and E. Bertrand. 2013. "New Insights into the Understanding of Flow Dynamics in an in Vitro Model for Abdominal Aortic Aneurysms." *Medical Engineering & Physics* 35 (6): 800–809. https://doi.org/10.1016/j.medengphy.2012.08.010.

Dufaux, F., and F. Moscheni. 1995. "Motion Estimation Techniques for Digital TV : A Review and a New Contribution." *Proceedings of the IEEE* 83 (6): 858–76. https://doi.org/10.1109/5.387089.

DuPont, J.J, R. M. Kenney, A. R. Patel, and I. Z. Jaffe. 2019. "Sex Differences in Mechanisms of Arterial Stiffness." *British Journal of Pharmacology* 176 (21): 4208–25. https://doi.org/10.1111/bph.14624.

Dussik, K. 1942. "Über Die Möglichkeit Hochfrequente Mechanische Schwingungen Als Diagnostisches Hilfsmittel Zu Verwenden." *Z Gezamte Neurol Psych*, 153–68. https://doi.org/10.1007/BF02877929.

Ebbini, E. S. 2006. "Phase-Coupled Two-Dimensional Speckle Tracking Algorithm." *IEEE Transactions on Ultrasonics, Ferroelectrics and Frequency Control* 53 (5): 972–90. https://doi.org/10.1109/TUFFC.2006.1632687.

Ekroll, I. K., A. Swillens, P. Segers, T. Dahl, H. Torp, and L. Lovstakken. 2013. "Simultaneous Quantification of Flow and Tissue Velocities Based on Multi-Angle Plane Wave Imaging." *IEEE Transactions on Ultrasonics, Ferroelectrics and Frequency Control* 60 (4): 727–38. https://doi.org/10.1109/TUFFC.2013.2621.

Eriksson, A., E. Greiff, T. Loupas, M. Persson, and P. Pesque. 2002. "Arterial Pulse Wave Velocity with Tissue Doppler Imaging." *Ultrasound in Medicine & Biology* 28 (5): 571–80. https://doi.org/10.1016/S0301-5629(02)00495-7.

Fadnes, S., S. A. Nyrnes, H. Torp, and L. Lovstakken. 2014. "Shunt Flow Evaluation in Congenital Heart Disease Based on Two-Dimensional Speckle Tracking." *Ultrasound in Medicine & Biology* 40 (10): 2379–91. https://doi.org/10.1016/j.ultrasmedbio.2014.03.029.

Fahrbach, K. 1970. "Ein Beitrag Zur Blutgeschwindigkeitsmessung Unter Anwendung Des Dopplereffektes." *Biomedizinische Technik/Biomedical Engineering* 15 (1): 26–36. https://doi.org/10.1515/bmte.1970.15.1.26.

Fekkes, S., A. E. C. M. Saris, M. M. Nillesen, J. Menssen, H. H. G. Hansen, and C. L. de Korte. 2018. "Simultaneous Vascular Strain and Blood Vector Velocity Imaging Using High-Frequency Versus Conventional-Frequency Plane Wave Ultrasound: A Phantom Study." *IEEE Transactions on Ultrasonics, Ferroelectrics, and Frequency Control* 65 (7): 1166–81. https://doi.org/10.1109/TUFFC.2018.2834724.

Ferrara, K. W., and R. Algazi. 1991. “A New Wideband Spread Target Maximum Likelihood Estimator for Blood Velocity Estimation-Part I: Theory.” *IEEE Transactions on Ultrasonics, Ferroelectrics and Frequency Control* 38 (1): 16. https://doi.org/10.1109/58.67829.

Foster, S. G., P. M. Embree, and W. D. O’Brien. 1990. “Flow Velocity Profile via Time-Domain Correlation: Error Analysis and Computer Simulation.” *IEEE Transactions on Ultrasonics, Ferroelectrics, and Frequency Control* 37 (3): 164–75. https://doi.org/10.1109/58.55306.

Friemel, B. H., L. N. Bohs, K. Nightingale, and G. E. Trahey. 1998. “Speckle Decorrelation Due to Two-Dimensional Flow Gradients.” *IEEE Transactions on Ultrasonics, Ferroelectrics and Frequency Control* 45 (2): 317–27. https://doi.org/10.1109/58.660142.

Fromageau, J., J.-L. Gennisson, C. Schmitt, R.L. Maurice, R. Mongrain, and G. Cloutier. 2007. “Estimation of Polyvinyl Alcohol Cryogel Mechanical Properties with Four Ultrasound Elastography Methods and Comparison with Gold Standard Testings.” *IEEE Transactions on Ultrasonics, Ferroelectrics and Frequency Control* 54 (3): 498–509. https://doi.org/10.1109/TUFFC.2007.273.

Fujikura, K., J. Luo, V. Gamarnik, M. Pernot, R. Fukumoto, M. D. Tilson, and E. E. Konofagou. 2007. “A Novel Noninvasive Technique for Pulse-Wave Imaging and Characterization of Clinically-Significant Vascular Mechanical Properties *In Vivo*.” *Ultrasonic Imaging* 29 (3): 137–54. https://doi.org/10.1177/016173460702900301.

Gamble, G., J. Zorn, G. Sanders, S. MacMahon, and N. Sharpe. 1994. “Estimation of Arterial Stiffness, Compliance, and Distensibility from M-Mode Ultrasound Measurements of the Common Carotid Artery.” *Stroke* 25 (1): 11–16. https://doi.org/10.1161/01.STR.25.1.11.

Gao, Z., Y. Li, Y. Y. Sun, J. Yang, H. Xiong, H. Zhang, X. Liu, W. Wu, D. Liang, and S. Li. 2018. “Motion Tracking of the Carotid Artery Wall From Ultrasound Image Sequences: A Nonlinear State-Space Approach.” *IEEE Transactions on Medical Imaging* 37 (1): 273–83. https://doi.org/10.1109/TMI.2017.2746879.

Garcia, D., P. Lantelme, and E. Saloux. 2018. “Introduction to Speckle Tracking in Cardiac Ultrasound Imaging.” In *Handbook of Speckle Filtering and Tracking in Cardiovascular Ultrasound Imaging and Video*, edited by C. P. Loizou, C. S. Pattichis, and J. D’hooge, 571–98. Institution of Engineering and Technology. https://doi.org/10.1049/PBHE013E_ch26.

Gasse, M., F. Millioz, E. Roux, D. Garcia, H. Liebgott, and D. Friboulet. 2017. “High-Quality Plane Wave Compounding Using Convolutional Neural Networks.” *IEEE Transactions on Ultrasonics, Ferroelectrics, and Frequency Control* 64 (10): 1637–39. https://doi.org/10.1109/TUFFC.2017.2736890.

Gastounioti, A, S Golemati, J S Stoitsis, and K S Nikita. 2013. “Carotid Artery Wall Motion Analysis from B-Mode Ultrasound Using Adaptive Block Matching: *In Silico* Evaluation and *in Vivo* Application.” *Physics in Medicine and Biology* 58 (24): 8647–61. https://doi.org/10.1088/0031-9155/58/24/8647.

Ghigo, N., V. Perrot, B. Harbaoui, A. Long, S. Ricci, P. Tortoli, D. Vray, and H. Liebgott. 2019. “High Frame Rate Vector Flow Imaging with a Convex Array in a Simulated Vessel Phantom.” In *2019 IEEE International Ultrasonics Symposium (IUS)*, 1–4. Glasgow, UK: IEEE. https://doi.org/10.1109/ULTSYM.2019.8925612.

Ghigo, N., A. Ramalli, S. Ricci, P. Tortoli, D. Vray, and H. Liebgott. 2020. “Sequence Optimization for High Frame Rate Imaging with a Convex Array.” In *2020 IEEE International Ultrasonics Symposium (IUS)*, 1–4. Las Vegas, NV, USA: IEEE. https://doi.org/10.1109/IUS46767.2020.9251286.

Giachetti, A. 2000. “Matching Techniques to Compute Image Motion.” *Image and Vision Computing* 18 (3): 247–60. https://doi.org/10.1016/S0262-8856(99)00018-9.

Golemati, S., J. S. Stoitsis, A. Gastounioti, A. C. Dimopoulos, V. Koropouli, and K. S. Nikita. 2012. “Comparison of Block Matching and Differential Methods for Motion Analysis of the Carotid Artery Wall From Ultrasound Images.” *IEEE Transactions on Information Technology in Biomedicine* 16 (5): 852–58. https://doi.org/10.1109/TITB.2012.2193411.

Goudot, G., O. Pedreira, J. Poree, L. Khider, T. Mirault, P. Julia, J.M. Alsac, M. Pernot, and E. Messas. 2019. “Assessment of Wall Shear Stress by Ultrafast Vector Flow Imaging in Carotid Atheromatous Stenosis.” *Archives of Cardiovascular Diseases Supplements* 11 (1): 96–97. https://doi.org/10.1016/j.acvdsp.2018.10.216.

Greenhalgh, R. M. 2004. “Comparison of Endovascular Aneurysm Repair with Open Repair in Patients with Abdominal Aortic Aneurysm (EVAR Trial 1), 30-Day Operative Mortality Results: Randomised Controlled Trial.” *The Lancet* 364 (9437): 843–48. https://doi.org/10.1016/S0140-6736(04)16979-1.

Greenhalgh, R. M., and J. T. Powell. 2008. “Endovascular Repair of Abdominal Aortic Aneurysm.” *New England Journal of Medicine* 358 (5): 494–501.

Hahn, S. L. 1996. *Hilbert Transforms in Signal Processing*. Boston : Artech House. Artech House Signal Processing Library.

Hansen, J. M., and J. A. Jensen. 2011. “Performance of Synthetic Aperture Compounding for In-Invo Imaging.” In *2011 IEEE International Ultrasonics Symposium*, 1148–51. Orlando, FL, USA: IEEE. https://doi.org/10.1109/ULTSYM.2011.0282.

Hansen, P. M., M.M. Pedersen, K. L. Hansen, M. B. Nielsen, and J. A. Jensen. 2011. “New Technology – Demonstration of a Vector Velocity Technique.” *Ultraschall in Der Medizin - European Journal of Ultrasound* 32 (02): 213–15. https://doi.org/10.1055/s-0031-1274628.

Hasegawa, H., K. Hongo, and H. Kanai. 2013. “Measurement of Regional Pulse Wave Velocity Using Very High Frame Rate Ultrasound.” *Journal of Medical Ultrasonics* 40 (2): 91–98. https://doi.org/10.1007/s10396-012-0400-9.

Hasegawa, H., and H. Kanai. 2008. “Simultaneous Imaging of Artery-Wall Strain and Blood Flow Realized by High Frame Rate Acquisition of RF Echoes.” In *2008 IEEE Ultrasonics Symposium*, 225–28. Beijing, China: IEEE. https://doi.org/10.1109/ULTSYM.2008.0055.

Haugaard, P., and G. Seerup. 2014. Vector flow ultrasound imaging. 8,911,373, filed 2012, and issued 2014.

Hein, I. A., and W. D. O’Brien. 1993. “Current Time-Domain Methods for Assessing Tissue Motion by Analysis from Reflected Ultrasound Echoes-a Review.” *IEEE Transactions on Ultrasonics, Ferroelectrics and Frequency Control* 40 (2): 84–102. https://doi.org/10.1109/58.212556.

Hertzer, N. R., E. J. Mascha, M. T. Karafa, P. J. O’Hara, L. P. Krajewski, and E. G. Beven. 2002. “Open Infrarenal Abdominal Aortic Aneurysm Repair: The Cleveland Clinic Experience from 1989 to 1998.” *Journal of Vascular Surgery* 35 (6): 1145–54. https://doi.org/10.1067/mva.2002.123686.

Heyde, B., N. Bottenus, J. D’hooge, and G. E. Trahey. 2017. “Evaluation of the Transverse Oscillation Technique for Cardiac Phased Array Imaging: A Theoretical Study.” *IEEE Transactions on Ultrasonics, Ferroelectrics, and Frequency Control* 64 (2): 320–34. https://doi.org/10.1109/TUFFC.2016.2622818.

Hoeks, A.P.G., P.J. Brands, F.A.M. Smeets, and R.S. Reneman. 1990. “Assessment of the Distensibility of Superficial Arteries.” *Ultrasound in Medicine & Biology* 16 (2): 121–28. https://doi.org/10.1016/0301-5629(90)90139-4.

Hong, Y. M. 2010. “Atherosclerotic Cardiovascular Disease Beginning in Childhood.” *Korean Circulation Journal* 40 (1): 1. https://doi.org/10.4070/kcj.2010.40.1.1.

Horn, B. K. P., and B. G. Schunck. 1981. “Determining Optical Flow.” *Artificial Intelligence* 17 (1–3): 185–203. https://doi.org/10.1016/0004-3702(81)90024-2.

Hoskins, P.R. 2019. “Principles of Doppler Ultrasound.” In *Diagnostic Ultrasound*, CRC Press, 143–58.

Huang, C., D. Guo, F. Lan, H. Zhang, and J. Luo. 2016. “Noninvasive Measurement of Regional Pulse Wave Velocity in Human Ascending Aorta with Ultrasound Imaging: An in-Vivo Feasibility Study.” *Journal of Hypertension* 34 (10): 2026–37. https://doi.org/10.1097/HJH.0000000000001060.

Huang, C., X. Pan, Q. He, M. Huang, L. Huang, X. Zhao, C. Yuan, J. Bai, and J. Luo. 2016. “Ultrasound-Based Carotid Elastography for Detection of Vulnerable Atherosclerotic Plaques Validated by

Magnetic Resonance Imaging." *Ultrasound in Medicine & Biology* 42 (2): 365–77. https://doi.org/10.1016/j.ultrasmedbio.2015.09.023.

Humphrey, J. D., and G. A. Holzapfel. 2011. "Mechanics, Mechanobiology, and Modeling of Human Abdominal Aorta and Aneurysms." *Journal of Biomechanics* 45 (5): 805–14. https://doi.org/10.1016/j.jbiomech.2011.11.021.

Jawien, A., B. Formankiewicz, T. Derezinski, A. Migdalski, P. Brazis, and L. Woda. 2014. "Abdominal Aortic Aneurysm Screening Program in Poland." *Gefässchirurgie* 19 (6): 545–48. https://doi.org/10.1007/s00772-014-1348-4.

Jensen, J. A. 1996a. *Estimation of Blood Velocities Using Ultrasound: A Signal Processing Approach*. Cambridge ; New York, USA: Cambridge University Press.

———. 2001. "A New Estimator for Vector Velocity Estimation." *IEEE Transactions on Ultrasonics, Ferroelectrics, and Frequency Control* 48 (4): 886–94. https://doi.org/10.1109/58.935705.

———. 2013. "Optimization of Transverse Oscillating Fields for Vector Velocity Estimation with Convex Arrays." In *2013 IEEE International Ultrasonics Symposium (IUS)*, 1753–56. Prague, Czech Republic: IEEE. https://doi.org/10.1109/ULTSYM.2013.0447.

———. 2014. "Comparison of Vector Velocity Imaging Using Directional Beamforming and Transverse Oscillation for a Convex Array Transducer." In . Vol. 9040. USA. https://doi.org/10.1117/12.2043701.

———. 2017. "Directional Transverse Oscillation Vector Flow Estimation." *IEEE Transactions on Ultrasonics, Ferroelectrics, and Frequency Control* 64 (8): 1194–1204. https://doi.org/10.1109/TUFFC.2017.2710361.

Jensen, J. A., A. H. Brandt, and M. B. Nielsen. 2015. "Convex Array Vector Velocity Imaging Using Transverse Oscillation and Its Optimization." *IEEE Transactions on Ultrasonics, Ferroelectrics, and Frequency Control* 62 (12): 2043–53. https://doi.org/10.1109/TUFFC.2015.006970.

Jensen, J. A., A. H. Brandt, and M.B Nielsen. 2014. "In-Vivo Convex Array Vector Flow Imaging." In *2014 IEEE International Ultrasonics Symposium*, 333–36. Chicago, IL, USA: IEEE. https://doi.org/10.1109/ULTSYM.2014.0082.

Jensen, J. A., and P. Munk. 1998. "A New Method for Estimation of Velocity Vectors." *IEEE Transactions on Ultrasonics, Ferroelectrics and Frequency Control* 45 (3): 837–51. https://doi.org/10.1109/58.677749.

Jensen, J. A., S. Nikolov, K. L. Hansen, M. B. Stuart, C. A. Villagomez, M. Schou, M. L. Ommen, et al. 2019. "History and Latest Advances in Flow Estimation Technology: From 1-D in 2-D to 3-D in 4-D." In , 1041–50. Glasgow, UK. https://doi.org/10.1109/ULTSYM.2019.8926210.

Jensen, J. A., S. I. Nikolov, K .L. Gammelmark, and M. H. Pedersen. 2006. "Synthetic Aperture Ultrasound Imaging." *Ultrasonics* 44 (December): e5–15. https://doi.org/10.1016/j.ultras.2006.07.017.

Jensen, J. A., S. Nikolov, A. C. H. Yu, and D. Garcia. 2016. "Ultrasound Vector Flow Imaging: I: Sequential Systems." *IEEE Transactions on Ultrasonics, Ferroelectrics, and Frequency Control*, 1–1. https://doi.org/10.1109/TUFFC.2016.2600763.

Jensen, J., M. B. Stuart, and J. A. Jensen. 2015. "High Frame Rate Vector Velocity Estimation Using Plane Waves and Transverse Oscillation." In *2015 IEEE International Ultrasonics Symposium (IUS)*, 1–4. Taipei, Taiwan: IEEE. https://doi.org/10.1109/ULTSYM.2015.0423.

Jensen, J.A. 1996b. "Field: A Program for Simulating Ultrasound Systems." In , 34:351–53. Medical & Biological Engineering & Computing.

Jensen, J.A., and N.B. Svendsen. 1992. "Calculation of Pressure Fields from Arbitrarily Shaped, Apodized, and Excited Ultrasound Transducers." *IEEE Transactions on Ultrasonics, Ferroelectrics and Frequency Control* 39 (2): 262–67. https://doi.org/10.1109/58.139123.

Kang, J., D. Go, I. Song, and Y. Yoo. 2020. "Wide Field-of-View Ultrafast Curved Array Imaging Using Diverging Waves." *IEEE Transactions on Biomedical Engineering* 67 (6): 1638–49. https://doi.org/10.1109/TBME.2019.2942164.

Karageorgos, G. M., I. Z. Apostolakis, P. Nauleau, V. Gatti, R. Weber, and E. E. Konofagou. 2021. "Pulse Wave Imaging Coupled with Vector Flow Mapping: A Phantom, Simulation and in Vivo Study." *IEEE Transactions on Ultrasonics, Ferroelectrics, and Frequency Control* 68 (7): 16–2531. https://doi.org/10.1109/TUFFC.2021.3074113.

Karageorgos, G. M., I. Zacharias Apostolakis, P. Nauleau, V. Gatti, R. Weber, J. Grondin, and E. E. Konofagou. 2019. "Imaging of Pulse Wave Propagation Coupled with Vector Flow and Wall Shear Stress Mapping in Atherosclerotic Plaque Phantoms and in Vivo." In *2019 IEEE International Ultrasonics Symposium (IUS)*, 243–46. Glasgow, United Kingdom: IEEE. https://doi.org/10.1109/ULTSYM.2019.8925888.

Kasai, C., K. Namekawa, A. Koyano, and R. Omoto. 1985. "Real-Time Two-Dimensional Blood Flow Imaging Using an Autocorrelation Technique." *IEEE Transactions on Sonics and Ultrasonics* 32 (3): 458–64. https://doi.org/10.1109/T-SU.1985.31615.

Keisler, B., and C. Carter. 2015. "Abdominal Aortic Aneurysm." *American Family Physician* 91 (8): 538–43.

Kent, K.C. 2014. "Abdominal Aortic Aneurysms." *The New England Journal of Medicine* 371 (22): 2101–8. https://doi.org/10.1056/NEJMcp1401430.

Kim, H. B., J. R. Hertzberg, and R. Shandas. 2004. "Development and Validation of Echo PIV." *Experiments in Fluids* 36 (3): 455–62. https://doi.org/10.1007/s00348-003-0743-5.

Kouame, D., J. M. Girault, J. P. Remenieras, J. P. Chemla, and M. Lethiecq. 2003. "High Resolution Processing Techniques for Ultrasound Doppler Velocimetry in the Presence of Colored Noise. Part II: Multiplephase Pipe-Flow Velocity Measurement." *IEEE Transactions on Ultrasonics, Ferroelectrics, and Frequency Control* 50 (3): 267–78. https://doi.org/10.1109/TUFFC.2003.1193620.

Kruizinga, P., F. Mastik, S. C. H. van den Oord, A. F. L. Schinkel, J. G. Bosch, N. de Jong, G. van Soest, and A. F. W. van der Steen. 2014. "High-Definition Imaging of Carotid Artery Wall Dynamics." *Ultrasound in Medicine & Biology* 40 (10): 2392–2403. https://doi.org/10.1016/j.ultrasmedbio.2014.03.009.

Lackland, D. T., and M. A. Weber. 2015. "Global Burden of Cardiovascular Disease and Stroke: Hypertension at the Core." *Canadian Journal of Cardiology* 31 (5): 569–71. https://doi.org/10.1016/j.cjca.2015.01.009.

Lenge, M., A. Ramalli, P. Tortoli, C. Cachard, and H. Liebgott. 2015. "Plane-Wave Transverse Oscillation for High-Frame-Rate 2-D Vector Flow Imaging." *IEEE Transactions on Ultrasonics, Ferroelectrics, and Frequency Control* 62 (12): 2126–37. https://doi.org/10.1109/TUFFC.2015.007320.

Leow, C. H., and M. X. Tang. 2018. "Spatio-Temporal Flow and Wall Shear Stress Mapping Based on Incoherent Ensemble-Correlation of Ultrafast Contrast Enhanced Ultrasound Images." *Ultrasound in Medicine & Biology* 44 (1): 134–52. https://doi.org/10.1016/j.ultrasmedbio.2017.08.930.

Li, R. X., J. Luo, S. K. Balaram, F. A. Chaudhry, D. Shahmirzadi, and E. E. Konofagou. 2013. "Pulse Wave Imaging in Normal, Hypertensive and Aneurysmal Human Aortas *in Vivo* : A Feasibility Study." *Physics in Medicine and Biology* 58 (13): 4549–62. https://doi.org/10.1088/0031-9155/58/13/4549.

Li, R. X., W. Qaqish, and E. E. Konofagou. 2015. "Performance Assessment of Pulse Wave Imaging Using Conventional Ultrasound in Canine Aortas Ex Vivo and Normal Human Arteries in Vivo." *Artery Research* 11 (September): 19–28. https://doi.org/10.1016/j.artres.2015.06.001.

Li, Z. Y., S. P. S. Howarth, T. Tang, and J. H. Gillard. 2006. "How Critical Is Fibrous Cap Thickness to Carotid Plaque Stability?: A Flow–Plaque Interaction Model." *Stroke* 37 (5): 1195–99. https://doi.org/10.1161/01.STR.0000217331.61083.3b.

Liebgott, H., A. Basarab, P. Gueth, D. Friboulet, and P. Delachartre. 2010. "Transverse Oscillations for Tissue Motion Estimation." *Physics Procedia* 3 (1): 235–44. https://doi.org/10.1016/j.phpro.2010.01.032.

Liebgott, H., A. Rodriguez-Molares, F. Cervenansky, J.A. Jensen, and O. Bernard. 2016. “Plane-Wave Imaging Challenge in Medical Ultrasound.” In *2016 IEEE International Ultrasonics Symposium (IUS)*, 1–4. Tours, France: IEEE. https://doi.org/10.1109/ULTSYM.2016.7728908.

Liebgott, H., J. Wilhjelm, J. Jensen, D. Vray, and P. Delachartre. 2007. “PSF Dedicated to Estimation of Displacement Vectors for Tissue Elasticity Imaging with Ultrasound.” *IEEE Transactions on Ultrasonics, Ferroelectrics and Frequency Control* 54 (4): 746–56. https://doi.org/10.1109/TUFFC.2007.308.

Lockwood, G. R., P. C. Li, M. O’Donnell, and F. S. Foster. 1996. “Optimizing the Radiation Pattern of Sparse Periodic Linear Arrays.” *IEEE Transactions on Ultrasonics, Ferroelectrics and Frequency Control* 43 (1): 7–14. https://doi.org/10.1109/58.484457.

Loupas, T., J. T. Powers, and R. W. Gill. 1995. “An Axial Velocity Estimator for Ultrasound Blood Flow Imaging, Based on a Full Evaluation of the Doppler Equation by Means of a Two-Dimensional Autocorrelation Approach.” *IEEE Transactions on Ultrasonics, Ferroelectrics and Frequency Control* 42 (4): 672–88. https://doi.org/10.1109/58.393110.

Lucas, B. D., and T. Kanade. 1981. “An Iterative Image Registration Technique with an Application to Stereo Vision.” In , 674–79. Vancouver.

Luo, J., and E. E. Konofagou. 2011. “Imaging of Wall Motion Coupled With Blood Flow Velocity in the Heart and Vessels in Vivo: A Feasibility Study.” *Ultrasound in Medicine & Biology* 37 (6): 980–95. https://doi.org/10.1016/j.ultrasmedbio.2011.03.004.

Luo, J., and E.E. Konofagou. 2010. “A Fast Normalized Cross-Correlation Calculation Method for Motion Estimation.” *IEEE Transactions on Ultrasonics, Ferroelectrics and Frequency Control* 57 (6): 1347–57. https://doi.org/10.1109/TUFFC.2010.1554.

Luo, J., R. X. Li, and E. E. Konofagou. 2012. “Pulse Wave Imaging of the Human Carotid Artery: An in Vivo Feasibility Study.” *IEEE Transactions on Ultrasonics, Ferroelectrics and Frequency Control* 59 (1): 174–81. https://doi.org/10.1109/TUFFC.2012.2170.

Luo, J., Wei-Ning Lee, Shougang Wang, and E. E. Konofagou. 2008. “Pulse Wave Imaging of Human Abdominal Aortas in Vivo.” In *2008 IEEE Ultrasonics Symposium*, 859–62. Beijing, China: IEEE. https://doi.org/10.1109/ULTSYM.2008.0207.

Lutz, H., and E. Buscarini. 2011. *Manual of Diagnostic Ultrasound*. Edited by World Health Organization. 2nd ed. Geneva, Switzerland: World Health Organization.

MacSweeney, S. T. R., J. T. Powell, and R. M. Greenhalgh. 1994. “Pathogenesis of Abdominal Aortic Aneurysm.” *British Journal of Surgery* 81 (7): 935–41. https://doi.org/10.1002/bjs.1800810704.

Mailloux, G. E., F. Langlois, P. Y. Simard, and M. Bertrand. 1989. “Restoration of the Velocity Field of the Heart from Two-Dimensional Echocardiograms.” *IEEE Transactions on Medical Imaging* 8 (2): 143–53. https://doi.org/10.1109/42.24862.

McCaul, K. A., M. Lawrence-Brown, J. A. Dickinson, and P. E. Norman. 2016. “Long-Term Outcomes of the Western Australian Trial of Screening for Abdominal Aortic Aneurysms: Secondary Analysis of a Randomized Clinical Trial.” *JAMA Internal Medicine* 176 (12): 1761. https://doi.org/10.1001/jamainternmed.2016.6633.

McGill, H. C., C. A. McMahan, and S. S. Gidding. 2008. “Preventing Heart Disease in the 21st Century: Implications of the Pathobiological Determinants of Atherosclerosis in Youth (PDAY) Study.” *Circulation* 117 (9): 1216–27. https://doi.org/10.1161/CIRCULATIONAHA.107.717033.

Mehregan, F., F. Tournoux, S. Muth, P. Pibarot, R. Rieu, G. Cloutier, and D. Garcia. 2014. “Doppler Vortography: A Color Doppler Approach to Quantification of Intraventricular Blood Flow Vortices.” *Ultrasound in Medicine & Biology* 40 (1): 210–21. https://doi.org/10.1016/j.ultrasmedbio.2013.09.013.

Moens, A.I. 1878. *Die Pulscurve*. University of California: Brill.

Montaldo, G., M. Tanter, J. Bercoff, N. Benech, and M. Fink. 2009. “Coherent Plane-Wave Compounding for Very High Frame Rate Ultrasonography and Transient Elastography.” *IEEE*

Transactions on Ultrasonics, Ferroelectrics and Frequency Control 56 (3): 489–506. https://doi.org/10.1109/TUFFC.2009.1067.

Moore, J. E., S. E. Maier, D. N. Ku, and P. Boesiger. 1994. "Hemodynamics in the Abdominal Aorta: A Comparison of in Vitro and in Vivo Measurements." *Journal of Applied Physiology* 76 (4): 1520–27. https://doi.org/10.1152/jappl.1994.76.4.1520.

Nichols, W., M. O'Rourke, and C. Vlachopoulos. 2011. "The Nature of Flow of a Liquid." In *McDonald's Blood Flow in Arteries 6th Edition: Theoretical, Experimental and Clinical Principles*, R. Reneman, 13–54. CRC Press.

Nichols, W. W., and D. A. McDonald. 1972. "Wave-Velocity in the Proximal Aorta." *Medical & Biological Engineering* 10 (3): 327–35. https://doi.org/10.1007/BF02474213.

Niu, L., L. Meng, L. Xu, J. Liu, Q. Wang, Y. Xiao, M. Qian, and H. Zheng. 2015. "Stress Phase Angle Depicts Differences in Arterial Stiffness: Phantom and *in Vivo* Study." *Physics in Medicine and Biology* 60 (11): 4281–94. https://doi.org/10.1088/0031-9155/60/11/4281.

Niu, L., M. Qian, R. Song, L. Meng, X. Liu, and H. Zheng. 2012. "A 2D Non-Invasive Ultrasonic Method for Simultaneous Measurement of Arterial Strain and Flow Pattern." *Clinical Physiology and Functional Imaging* 32 (4): 323–29. https://doi.org/10.1111/j.1475-097X.2012.01130.x.

Nix, L., and G. Johnson. 1988. "Clinical Applications of Doppler Ultrasound." *Journal of Vascular Surgery* 8 (2): 206. https://doi.org/10.1016/0741-5214(88)90421-1.

O'Leary, B., and S. Vaezy. 2019. "Marketing Clearance of Diagnostic Ultrasound Systems and Transducers." Guidance for Industry and Food and Drug Administration Staff.

Papadacci, C., V. Finel, O. Villemain, G. Goudot, J Provost, E. Messas, M. Tanter, and M. Pernot. 2019. "4D Simultaneous Tissue and Blood Flow Doppler Imaging: Revisiting Cardiac Doppler Index with Single Heart Beat 4D Ultrafast Echocardiography." *Physics in Medicine & Biology* 64 (8): 085013. https://doi.org/10.1088/1361-6560/ab1107.

Papadacci, C., M. Pernot, M. Couade, M. Fink, and M. Tanter. 2014. "High-Contrast Ultrafast Imaging of the Heart." *IEEE Transactions on Ultrasonics, Ferroelectrics, and Frequency Control* 61 (2): 288–301. https://doi.org/10.1109/TUFFC.2014.6722614.

"Particular Requirements for the Safety of Ultrasonic Medical Diagnostic and Monitoring Equipment." 2015. International Standard IEC 60601-2-37:2007+AMD1:2015. Medical Electrical Equipment. International Electrotechnical Commission.

Perrot, V., I. K. Ekroll, J. Avdal, L. M. Saxhaug, H. Dalen, D. Vray, L. Lovstakken, and H. Liebgott. 2021. "Translation of Simultaneous Vessel Wall Motion and Vectorial Blood Flow Imaging in Healthy and Diseased Carotids to the Clinic: A Pilot Study." *IEEE Transactions on Ultrasonics, Ferroelectrics, and Frequency Control* 68 (3): 558–69. https://doi.org/10.1109/TUFFC.2020.3015340.

Perrot, V., and D. Garcia. 2018. "Back to Basics in Ultrasound Velocimetry: Tracking Speckles by Using a Standard Piv Algorithm." In *2018 IEEE International Ultrasonics Symposium (IUS)*, 206–12. Kobe: IEEE. https://doi.org/10.1109/ULTSYM.2018.8579665.

Perrot, V., H. Liebgott, A. Long, and D. Vray. 2018. "Simultaneous Tissue and Flow Estimation at High Frame Rate Using Plane Wave and Transverse Oscillation on in Vivo Carotid." In . https://doi.org/10.1109/ULTSYM.2018.8580182.

Perrot, V., L. Petrusca, A. Bernard, D. Vray, and H. Liebgott. 2017. "Simultaneous Pulse Wave and FLow Estimation at High-Framerate Using Plane Wave and Transverse Oscillation on Carotid Phantom." In , 1–4. Washington, DC, USA. https://doi.org/10.1109/ULTSYM.2017.8091683.

Perrot, V., M. Polichetti, F. Varray, and D. Garcia. 2021. "So You Think You Can DAS? A Viewpoint on Delay-and-Sum Beamforming." *Ultrasonics* 111 (March): 106309. https://doi.org/10.1016/j.ultras.2020.106309.

Piechota-Polanczyk, A., A. Jozkowicz, W. Nowak, W. Eilenberg, C. Neumayer, T. Malinski, I. Huk, and C. Brostjan. 2015. "The Abdominal Aortic Aneurysm and Intraluminal Thrombus: Current Concepts of Development and Treatment." *Frontiers in Cardiovascular Medicine* 2 (May). https://doi.org/10.3389/fcvm.2015.00019.

Poree, J., D. Posada, A. Hodzic, F. Tournoux, G. Cloutier, and G. Garcia. 2016. "High-Frame-Rate Echocardiography Using Coherent Compounding With Doppler-Based Motion-Compensation." *IEEE Transactions on Medical Imaging* 35 (7): 1647–57. https://doi.org/10.1109/TMI.2016.2523346.

Powell, J. T. 2016. "Diverse Requirements for Efficient Population Screening for Abdominal Aortic Aneurysm: From Program Management to Maintaining Skills in Open Repair." *Circulation* 134 (16): 1149–51. https://doi.org/10.1161/CIRCULATIONAHA.116.024916.

Price, D J A. 2000. "Tissue Doppler Imaging: Current and Potential Clinical Applications." *Heart* 84 (90002): 11ii–1118. https://doi.org/10.1136/heart.84.suppl_2.ii11.

Provost, J., C. Papadacci, J. E. Arango, M. Imbault, M. Fink, J. L. Gennisson, M. Tanter, and M. Pernot. 2014. "3D Ultrafast Ultrasound Imaging *in Vivo*." *Physics in Medicine and Biology* 59 (19): L1–13. https://doi.org/10.1088/0031-9155/59/19/L1.

Qorchi, S., D. Vray, and M. Orkisz. 2021. "Estimating Arterial Wall Deformations from Automatic Key-Point Detection and Matching." *Ultrasound in Medicine & Biology* 47 (5): 1367–76. https://doi.org/10.1016/j.ultrasmedbio.2021.01.001.

Quaia, E. 2007. "Microbubble Ultrasound Contrast Agents: An Update." *European Radiology* 17 (8): 1995–2008. https://doi.org/10.1007/s00330-007-0623-0.

Rabben, Stein Inge, Steinar Bjærum, Vidar Sørhus, and Hans Torp. 2002. "Ultrasound-Based Vessel Wall Tracking: An Auto-Correlation Technique with RF Center Frequency Estimation." *Ultrasound in Medicine & Biology* 28 (4): 507–17. https://doi.org/10.1016/S0301-5629(02)00487-8.

Raffel, M., C. E. Willert, F. Scarano, C. J. Kähler, S. T. Wereley, and J. Kompenhans. 2018. "Image Evaluation Methods for PIV." In *Particle Image Velocimetry*, by M. Raffel, C. E. Willert, F. Scarano, C. J. Kähler, S. T. Wereley, and J. Kompenhans, 145–202. Cham: Springer International Publishing. https://doi.org/10.1007/978-3-319-68852-7_5.

Ramalli, A., K. Aizawa, A. C. Shore, C. Morizzo, C. Palombo, M. Lenge, and P. Tortoli. 2019. "Continuous Simultaneous Recording of Brachial Artery Distension and Wall Shear Rate: A New Boost for Flow-Mediated Vasodilation." *IEEE Transactions on Ultrasonics, Ferroelectrics, and Frequency Control* 66 (3): 463–71. https://doi.org/10.1109/TUFFC.2018.2889111.

Ramnarine, K. V., D. K. Nassiri, P. R. Hoskins, and J. Lubbers. 1998. "Validation of a New Blood-Mimicking Fluid for Use in Doppler Flow Test Objects." *Ultrasound in Medicine & Biology* 24 (3): 451–59. https://doi.org/10.1016/S0301-5629(97)00277-9.

Ramnarine, Kumar V, Tim Hartshorne, Yvonne Sensier, May Naylor, Joanne Walker, A Ross Naylor, Ronney B Panerai, and David H Evans. 2003. "Tissue Doppler Imaging of Carotid Plaque Wall Motion: A Pilot Study." *Cardiovascular Ultrasound* 1 (1): 17. https://doi.org/10.1186/1476-7120-1-17.

Reile, R., T. Vorno, J. Kals, P. Ilves, and R. A. Kiivet. 2020. "The Cost-Effectiveness of Abdominal Aortic Aneurysm Screening in Estonia." *Value in Health Regional Issues* 22 (September): 1–6. https://doi.org/10.1016/j.vhri.2019.08.477.

Rodriguez-Molares, Alfonso. 2017. "Report on the Safety of Ultrasonic Medical Diagnostic Equipment." Plane-Wave sequences in the Verasonics Vantage 256 Research Platform and GE 9L-D probe.

Roy, C. S. 1881. "The Elastic Properties of the Arterial Wall." *The Journal of Physiology* 3 (2): 125–59. https://doi.org/10.1113/jphysiol.1881.sp000088.

Salles, S., A. J. Y. Chee, D. Garcia, A. C. H. Yu, D. Vray, and H. Liebgott. 2015. "2-D Arterial Wall Motion Imaging Using Ultrafast Ultrasound and Transverse Oscillations." *IEEE Transactions on Ultrasonics, Ferroelectrics, and Frequency Control* 62 (6): 1047–58. https://doi.org/10.1109/TUFFC.2014.006910.

Salles, S., D. Garcia, B. Bou-Said, F. Savary, A. Serusclat, D. Vray, and H. Liebgott. 2014. "Plane Wave Transverse Oscillation (PWTO): An Ultra-Fast Transverse Oscillation Imaging Mode Performed in the Fourier Domain for 2D Motion Estimation of the Carotid Artery." In *2014 IEEE 11th*

International Symposium on Biomedical Imaging (ISBI), 1409–12. Beijing, China: IEEE. https://doi.org/10.1109/ISBI.2014.6868142.

Salles, S., H. Liebgott, O. Basset, C. Cachard, D. Vray, and R. Lavarello. 2014. "Experimental Evaluation of Spectral-Based Quantitative Ultrasound Imaging Using Plane Wave Compounding." *IEEE Transactions on Ultrasonics, Ferroelectrics, and Frequency Control* 61 (11): 1824–34. https://doi.org/10.1109/TUFFC.2014.006543.

Salles, S., F. Varray, D. Garcia, B. Nicolas, and H. Liebgott. 2019. "Investigation on 3D High Frame Rate Imaging with Motion Compensation (MoCo)." In *2019 IEEE International Ultrasonics Symposium (IUS)*, 1274–77. Glasgow, United Kingdom: IEEE. https://doi.org/10.1109/ULTSYM.2019.8926273.

Salles, S., G. Zahnd, H. Liebgott, A. Serusclat, and D. Vray. 2012. "Real Time US-Tagging Combined with Phase-Based Optical Flow Applied to 2D Motion Estimation of the Carotid Artery Wall." In *2012 IEEE International Ultrasonics Symposium*, 1185–88. Dresden, Germany: IEEE. https://doi.org/10.1109/ULTSYM.2012.0295.

Satomura, S. 1957. "Ultrasonic Doppler Method for the Inspection of Cardiac Functions." *The Journal of the Acoustical Society of America* 29 (11): 1181–85. https://doi.org/10.1121/1.1908737.

———. 1959. "Study of the flow patterns in peripheral arteries by ultrasonics." *The Journal of the Acoustical Society of Japan* 15: 151–1578.

Scott, R. 2002. "The Multicentre Aneurysm Screening Study (MASS) into the Effect of Abdominal Aortic Aneurysm Screening on Mortality in Men: A Randomised Controlled Trial." *The Lancet* 360 (9345): 1531–39. https://doi.org/10.1016/S0140-6736(02)11522-4.

Seferidis, V. 1994. "Generalised Block-Matching Motion Estimation Using Quad-Tree Structured Spatial Decomposition." *IEE Proceedings - Vision, Image, and Signal Processing* 141 (6): 446. https://doi.org/10.1049/ip-vis:19941423.

Selfridge, A. R., G. S. Kino, and B. T. Khuri-Yakub. 1980. "A Theory for the Radiation Pattern of a Narrow-strip Acoustic Transducer." *Applied Physics Letters* 37 (1): 35–36. https://doi.org/10.1063/1.91692.

Sonesson, B., F. Hansen, and T. Lanne. 1993. "Compliance and Diameter in the Human Abdominal Aorta -The Influence of Age and Sex." *European Journal of Vascular and Endovascular Surgery* 7 (6): 690–97. https://doi.org/10.1016/S0950-821X(05)80718-2.

Spallanzani, L. 1794. "Lettere Sopra Il Aoqpetto d 'un Nuovo Senso Nei Pipistrelli." In *Le Opere Di Lazzaro Spallanzani*. Vol. 5. Reale Accademia D'Italia.

Spanos, K., N. Labropoulos, and A. Giannoukas. 2018. "Abdominal Aortic Aneurysm Screening: Do We Need to Shift Toward a Targeted Strategy?" *Angiology* 69 (3): 192–94. https://doi.org/10.1177/0003319717710861.

Stefanadis, C., C. K. Antoniou, D. Tsiachris, and P. Pietri. 2017. "Coronary Atherosclerotic Vulnerable Plaque: Current Perspectives." *Journal of the American Heart Association* 6 (3). https://doi.org/10.1161/JAHA.117.005543.

Steward, E. G. 2004. *Fourier Optics: An Introduction.* Courier Corporation. Mineola, NY: Dover publications, INC.

Stewart, S. F. C. 2001. "Effects of Transducer, Velocity, Doppler Angle, and Instrument Settings on the Accuracy of Color Doppler Ultrasound." *Ultrasound in Medicine & Biology* 27 (4): 551–64. https://doi.org/10.1016/S0301-5629(01)00357-X.

Suhling, M., M. Arigovindan, C. Jansen, P. Hunziker, and M. Unser. 2005. "Myocardial Motion Analysis from B-Mode Echocardiograms." *IEEE Transactions on Image Processing* 14 (4): 525–36. https://doi.org/10.1109/TIP.2004.838709.

Sumi, C. 1999. "Fine Elasticity Imaging Utilizing RF-Echo Phase Matching." *IEEE Transactions on Ultrasonics, Ferroelectrics, and Frequency Control* 46 (1): 158–66. https://doi.org/10.1109/58.741527.

———. 2008. “Displacement Vector Measurement Using Instantaneous Ultrasound Signal Phase-Multidimensional Autocorrelation and Doppler Methods.” *IEEE Transactions on Ultrasonics, Ferroelectrics and Frequency Control* 55 (1): 24–43. https://doi.org/10.1109/TUFFC.2008.614.

Szabo, T. L. 2004. *Diagnostic Ultrasound Imaging: Inside Out*. Academic Press. Elvesier.

Tamura, T., R. S. C. Cobbold, and K. W. Johnston. 1991. “Quantitative Study of Steady Flow Using Color Doppler Ultrasound.” *Ultrasound in Medicine & Biology* 17 (6): 595–605. https://doi.org/10.1016/0301-5629(91)90030-Z.

Tanter, M., and M. Fink. 2014. “Ultrafast Imaging in Biomedical Ultrasound.” *IEEE Transactions on Ultrasonics, Ferroelectrics, and Frequency Control* 61 (1): 102–19. https://doi.org/10.1109/TUFFC.2014.2882.

Tong, L., A. Ramalli, R. Jasaityte, P. Tortoli, and J. D’hooge. 2014. “Multi-Transmit Beam Forming for Fast Cardiac Imaging—Experimental Validation and In Vivo Application.” *IEEE Transactions on Medical Imaging* 33 (6): 1205–19. https://doi.org/10.1109/TMI.2014.2302312.

Tortoli, P. 2011. “Simultaneous Ultrasound Assessment of Brachial Artery Shear Stimulus and Flow-Mediated Dilation During Reactive Hyperemia.” *Ultrasound in Medicine and Biology* 37 (10): 10.

Tortoli, P., G. Bambi, F. Guidi, and R. Muchada. 2002. “Toward a Better Quantitative Measurement of Aortic Flow.” *Ultrasound in Medicine & Biology* 28 (2): 249–57. https://doi.org/10.1016/S0301-5629(01)00462-8.

Tortoli, P., M. Lenge, D. Righi, G. Ciuti, H. Liebgott, and S. Ricci. 2015. “Comparison of Carotid Artery Blood Velocity Measurements by Vector and Standard Doppler Approaches.” *Ultrasound in Medicine & Biology* 41 (5): 1354–62. https://doi.org/10.1016/j.ultrasmedbio.2015.01.008.

Tortoli, P., T. Morganti, G. Bambi, C. Palombo, and K. V. Ramnarine. 2006. “Noninvasive Simultaneous Assessment of Wall Shear Rate and Wall Distension in Carotid Arteries.” *Ultrasound in Medicine & Biology* 32 (11): 1661–70. https://doi.org/10.1016/j.ultrasmedbio.2006.07.023.

Trahey, G. E., J. W. Allison, and O. T. Ramm. 1987. “Angle Independent Ultrasonic Detection of Blood Flow.” *IEEE Transactions on Biomedical Engineering* 34 (12): 965–67. https://doi.org/10.1109/TBME.1987.325938.

Trahey, G. E., S. M. Hubbard, and O. T. Ramm. 1988. “Angle Independent Ultrasonic Blood Flow Detection by Frame-to-Frame Correlation of B-Mode Images.” *Ultrasonics* 26 (5): 271–76. https://doi.org/10.1016/0041-624X(88)90016-9.

Tublin, M. E., R. O. Bude, and J. F. Platt. 2003. “The Resistive Index in Renal Doppler Sonography: Where Do We Stand?” *American Journal of Roentgenology* 180 (4): 885–92. https://doi.org/10.2214/ajr.180.4.1800885.

Udesen, J., F. Gran, K. Hansen, J. A. Jensen, C. Thomsen, and M. B. Nielsen. 2008. “High Frame-Rate Blood Vector Velocity Imaging Using Plane Waves: Simulations and Preliminary Experiments.” *IEEE Transactions on Ultrasonics, Ferroelectrics and Frequency Control* 55 (8): 1729–43. https://doi.org/10.1109/TUFFC.2008.858.

Udesen, J., and J. A. Jensen. 2006. “Investigation of Transverse Oscillation Method.” *IEEE Transactions on Ultrasonics, Ferroelectrics and Frequency Control* 53 (5): 959–71. https://doi.org/10.1109/TUFFC.2006.1632686.

Udesen, J., M. B. Nielsen, K. R. Nielsen, and J. A. Jensen. 2007. “Examples of In Vivo Blood Vector Velocity Estimation.” *Ultrasound in Medicine & Biology* 33 (4): 541–48. https://doi.org/10.1016/j.ultrasmedbio.2006.10.014.

Vaitkus, P. J., and R. S. C. Cobbold. 1998. “A New Time-Domain Narrowband Velocity Estimation Technique for Doppler Ultrasound Flow Imaging. Part I: Theory.” *IEEE Transactions on Ultrasonics, Ferroelectrics, and Frequency Control* 45 (4): 939–54. https://doi.org/10.1109/58.710565.

Vappou, J., J. Luo, and E. E. Konofagou. 2010. “Pulse Wave Imaging for Noninvasive and Quantitative Measurement of Arterial Stiffness In Vivo.” *American Journal of Hypertension* 23 (4): 393–98. https://doi.org/10.1038/ajh.2009.272.

Vappou, Jonathan, J. Luo, K. Okajima, M. Di Tullio, and E. E. Konofagou. 2011. “Aortic Pulse Wave Velocity Measured by Pulse Wave Imaging (PWI): A Comparison with Applanation Tonometry.” *Artery Research* 5 (2): 65–71. https://doi.org/10.1016/j.artres.2011.03.002.

Varray, F., and H. Liebgott. 2013. “An Alternative Method to Classical Beamforming for Transverse Oscillation Images: Application to Elastography.” In *2013 IEEE 10th International Symposium on Biomedical Imaging*, 716–19. San Francisco, CA, USA: IEEE. https://doi.org/10.1109/ISBI.2013.6556575.

Viola, F., and W. F. Walker. 2003. “A Comparison of the Performance of Time-Delay Estimators in Medical Ultrasound.” *IEEE Transactions on Ultrasonics, Ferroelectrics and Frequency Control* 50 (4): 392–401. https://doi.org/10.1109/TUFFC.2003.1197962.

Wade, G. 2000. “Human Uses of Ultrasound: Ancient and Modern.” *Ultrasonics* 38 (1–8): 1–5. https://doi.org/10.1016/S0041-624X(99)00063-3.

Walker, W. F., and G. E. Trahey. 1994. “A Fundamental Limit on the Performance of Correlation Based Phase Correction and Flow Estimation Techniques.” *IEEE Transactions on Ultrasonics, Ferroelectrics and Frequency Control* 41 (5): 644–54. https://doi.org/10.1109/58.308499.

Wan, Y., D. Liu, and E. S. Ebbini. 2010. “Imaging Vascular Mechanics Using Ultrasound: Phantom and in Vivo Results.” In *2010 IEEE International Symposium on Biomedical Imaging: From Nano to Macro*, 980–83. Rotterdam, Netherlands: IEEE. https://doi.org/10.1109/ISBI.2010.5490152.

Wang, Y., C. Huang, S. Ma, and Q. He. 2019. “Pulse Wave Imaging for Assessing Arterial Stiffness Change in a Mouse Model of Thoracic Aortic Dissection in Marfan Syndrome.” In , 2206–9. Glasgow, UK: IEEE. https://doi.org/10.1109/ULTSYM.2019.8926304.

Wanhainen, A., R. Hultgren, and A. Linne. 2017. “Outcome of the Swedish Nationwide Abdominal Aortic Aneurysm Screening Program.” *Journal of Vascular Surgery* 65 (2): 585. https://doi.org/10.1016/j.jvs.2016.12.060.

Watson, J. D. B., S. M. Gifford, and D. F. Bandyk. 2020. “Aortic Aneurysm Screening Using Duplex Ultrasound: Choosing Wisely Who to Examine.” *Seminars in Vascular Surgery* 33 (3–4): 54–59. https://doi.org/10.1053/j.semvascsurg.2020.05.002.

Wells, P. N. T. 1969. “A Range-Gated Ultrasonic Doppler System.” *Medical & Biological Engineering* 7 (6): 641–52. https://doi.org/10.1007/BF02551735.

Willert, C. E., and M. Gharib. 1991. “Digital Particle Image Velocimetry.” *Experiments in Fluids* 10 (4): 181–93. https://doi.org/10.1007/BF00190388.

Yeung, F., S .F. Levinson, Dongshan Fu, and K. J. Parker. 1998. “Feature-Adaptive Motion Tracking of Ultrasound Image Sequences Using a Deformable Mesh.” *IEEE Transactions on Medical Imaging* 17 (6): 945–56. https://doi.org/10.1109/42.746627.

Yeung, Fai, S. F. Levinson, and K. J. Parker. 1998. “Multilevel and Motion Model-Based Ultrasonic Speckle Tracking Algorithms.” *Ultrasound in Medicine & Biology* 24 (3): 427–41. https://doi.org/10.1016/S0301-5629(97)00281-0.

Zahnd, G., M. Orkisz, A. Sérusclat, P. Moulin, and D. Vray. 2013. “Evaluation of a Kalman-Based Block Matching Method to Assess the Bi-Dimensional Motion of the Carotid Artery Wall in B-Mode Ultrasound Sequences.” *Medical Image Analysis* 17 (5): 573–85. https://doi.org/10.1016/j.media.2013.03.006.

Zahnd, G., M. Orkisz, A. Serusclat, and D. Vray. 2012. “Longitudinal Motion of the Carotid Artery Wall and Speckle Decorrelation Issue: Accurate Estimation Using a Kalman-Based Speckle Tracking Method.” In *2012 IEEE International Ultrasonics Symposium*, 1366–69. Dresden, Germany: IEEE. https://doi.org/10.1109/ULTSYM.2012.0341.

Zarins, C. K., D. P. Giddens, B. K. Bharadvaj, V. S. Sottiurai, and R. F. Mabon. 1983. “Carotid Bifurcation Atherosclerosis. Quantitative Correlation of Plaque Localization with Flow Velocity Profiles and Wall Shear Stress.” *Circulation Research* 53 (4): 13. https://doi.org/10.1161/01.RES.53.4.502.

Zhu, H., and Z. Wang. 2020. “Feature Matching in Ultrasound Images.” *ArXiv:2010.12216 [Cs]*, October. http://arxiv.org/abs/2010.12216.

Appendices

Résumé en français

Ce travail de thèse est consacré à l'imagerie ultrasonore, aussi appelée échographie. L'objectif est de fournir aux cliniciens un mode d'imagerie permettant d'extraire simultanément le mouvement pariétal et le flux, à une cadence d'imagerie élevée, dans les vaisseaux sanguins pouvant être imagés avec une sonde convexe, telle que l'aorte abdominale.

Les maladies cardiovasculaires regroupent les maladies qui touchent le cœur, les vaisseaux sanguins, ou les deux. Leur processus de formation n'est pas encore totalement compris, bien que l'on suppose que des paramètres liés à la vitesse d'écoulement et au mouvement de la paroi pourraient être des marqueurs de certaines de ces pathologies. Ainsi en suivant l'évolution de ces marqueurs, il serait possible de quantifier l'évolution de la maladie. L'évaluation de ces marqueurs pourrait également permettre une détection précoce de ces maladies.

Le cœur induit des mouvements rapides, transitoires et complexes dans les vaisseaux sanguins et notamment dans les artères. Une modalité à haute cadence d'images est alors nécessaire pour extraire le plus d'informations possible sur l'état du système cardiovasculaire.

Les vaisseaux superficiels, comme la carotide, sont typiquement imagés avec une sonde ultrasonore linéaire. Pour étudier les vaisseaux profonds, les cliniciens privilégient les sondes convexes qui permettent d'obtenir des images ultrasonores avec un plus large champ de vue et dont la fréquence centrale relativement basse est adaptée à l'imagerie de tissus profonds.

A l'heure actuelle, aucune technique n'est utilisée en clinique pour extraire à la fois des marqueurs de flux et de la paroi à des fréquences d'imagerie élevée avec une sonde convexe. Dans cette thèse, une séquence ultrasonore et un algorithme permettant l'extraction des paramètres de flux et de tissu, à des cadences d'imagerie élevées sur des artères visualisées avec une sonde convexe, sont présentés.

Il y a trois contributions scientifiques principales dans cette thèse :

1. la conception de la séquence ultrasonore à une haute cadence d'imagerie,
2. un algorithme pour l'estimation du mouvement 2D du flux et du mouvement tissulaire,
3. une preuve de concept expérimentale.

Ce manuscrit est divisé en cinq chapitres. Le premier chapitre présente le contexte général et introduit le contexte médical et le concept de l'imagerie ultrasonore. L'intérêt de ce travail de thèse est aussi mis en évidence. L'état de l'art des méthodes d'estimation de mouvement utilisées en imagerie ultrasonore est décrit dans le second chapitre. Les méthodes Doppler et non-Doppler sont présentées ainsi que les précédents travaux réalisés sur la mesure simultanée du mouvement tissulaire et du flux. A notre connaissance, aucune étude réalisée à ce jour permet d'étudier simultanément le flux et le mouvement pariétal de vaisseaux imagés avec une sonde convexe. Ce chapitre conclue par les buts et objectifs de cette thèse. Dans le troisième chapitre, la séquence ultrasonore utilisée dans le reste de la thèse est présentée : elle permet de conserver une cadence d'imagerie assez élevée pour l'observation des phénomènes rapides, tout en obtenant une qualité d'image suffisante pour pouvoir étudier ces phénomènes. Le quatrième chapitre décrit la méthode d'estimation 2D de mouvement

dites par “oscillations transverses” utilisée dans cette thèse. La méthode d’oscillations transverses a dû être adaptée pour l’utilisation d’une sonde convexe avec une haute cadence d’imagerie. La chaîne de traitement est ensuite présentée et la méthode a été validée *in vitro* sur un montage expérimental réalisé au laboratoire. Le cinquième chapitre vise à faire avancer la méthode vers l’étude *in vivo*. Des mesures de sécurité ont été réalisées pour prouver que l’émission ultrasonore utilisée ne présente pas de danger apparent. L’aorte abdominale d’un volontaire sain a ensuite été imagée et le flux et le mouvement de la paroi ont pu être extraits.

Chapitre 1

Le cœur est l’organe central du système cardiovasculaire et joue le rôle d’une pompe responsable de la circulation sanguine. Le sang est transporté vers les organes par les artères puis retourne au cœur via le système veineux. Si une faiblesse se développe à n’importe quel endroit du système cardiovasculaire (cœur, artères, veines), l’entièreté du système cardiovasculaire est aussi touchée. Ainsi une maladie cardiaque s’accompagne généralement de problèmes vasculaires et réciproquement. Certaines pathologies peuvent se développer au sein des artères : plaques d’athérome, anévrismes, ou encore sténoses pour en lister quelques-unes. Pour la plupart, elles restent silencieuses et souvent indétectables jusqu’à des stades avancés et potentiellement mortels. Bien que les causes de ces maladies soient encore mal connues, la prévention reste l’approche préconisée ; l’autre possibilité étant l’intervention chirurgicale dans les cas très avancés. Il est alors essentiel de pouvoir détecter ces pathologies le plus tôt possible et de quantifier leur niveau de gravité. La méthode d’imagerie la plus utilisée pour les examens vasculaires est l’imagerie ultrasonore, ou échographie.

L’imagerie ultrasonore se prête particulièrement bien à l’étude du système cardiovasculaire, car elle est non invasive, relativement peu coûteuse, transportable et les examens sont rapidement effectués. Le système artériel est sujet à des phénomènes physiques complexes et rapides. Par conséquent, une méthode d’imagerie à haute cadence (au-delà de 500 images par seconde) est nécessaire. Les méthodes ultrasonores dites « ultra-rapides » ont été développées dans les années 2000, et permettent, en insonifiant le milieu avec un large front d’onde, d’obtenir des cadences d’imagerie dépassant 10 000 images par seconde dans les vaisseaux superficiels. L’énergie ultrasonore est largement dispersée dans le milieu, ce qui diminue la qualité des images obtenues. En combinant plusieurs images, dites basse résolution, acquises avec ces méthodes ultra-rapides, une image finale de bonne qualité peut être obtenue. Ce gain en qualité d’image se fait au détriment de la cadence d’imagerie qui est divisée par le nombre d’images basse résolution combinées. Un compromis doit alors être fait entre qualité d’image et cadence d’imagerie.

Différentes sondes ultrasonores sont utilisées pour différents types d’examens. Ainsi les sondes linéaires, qui ont des fréquences élevées, sont privilégiées lors de l’examen de vaisseaux superficiels. A contrario, les sondes convexes ont des fréquences d’imagerie plus basses qui permettent une plus grande pénétration dans le milieu au détriment de la résolution d’image. Pour des vaisseaux profonds, tels que l’aorte abdominale, ce sont ces sondes qui sont privilégiés, d’autant plus qu’elles offrent un large champ de vue.

Un certain nombre de marqueurs pathologiques artériels ont déjà été développés et sont utilisés en clinique. En ce qui concerne les tissus, le diamètre artériel est mesuré lors des examens cliniques. Par exemple, le diamètre d’un anévrisme est utilisé pour caractériser l’avancement de cette pathologie. Le flux quant à lui est utilisé pour délimiter précisément les limites et la position des parois artérielles.

De plus, la vitesse et la direction du sang dans l'anévrisme permettent de déterminer si celui-ci est à risque de rupture. D'autres marqueurs, plus avancés, ont été développés en recherche mais restent peu utilisés dans la pratique clinique. Par exemple, la rigidité artérielle peut être quantifiée via la mesure de la vitesse de l'onde de pouls. Cette onde mécanique se propage au cours des cycles cardiaques le long des parois artérielles et sa vitesse de propagation est liée à rigidité vasculaire. Elle permet donc de quantifier la rigidité de la paroi qui est souvent considérée comme un des premiers signes du développement de l'athérosclérose (dépôt de plaque affaiblissement une artère). Etant donné les différents paramètres et marqueurs pathologiques existants sur le flux et le tissu, une technique permettant l'extraction simultanée de ces marqueurs est pertinente pour la caractérisation des pathologies artérielles.

En recherche, plusieurs groupes travaillent déjà sur le développement de méthodes d'imagerie simultanée du flux et du mouvement pariétale. Cependant, toutes les méthodes proposées se concentrent sur l'utilisation d'une sonde linéaire, notamment pour l'étude de la carotide. Elles ne sont donc pas directement utilisables à l'usage de sondes convexes qui sont nécessaires pour imager l'aorte abdominale. Il y a donc un réel besoin de développer une méthode permettant l'étude du flux et du mouvement pariétal de manière simultanée spécifiquement dédiée à l'utilisation de sonde convexe.

En conclusion de ce chapitre, les maladies cardiovasculaires sont un fléau mondial, premières causes de mortalité dans les pays développés. L'imagerie ultrasonore se prête particulièrement bien à l'étude du système cardiovasculaire et permet d'obtenir, via des modes d'imagerie « ultra-rapides », une haute résolution temporelle. L'utilisation de l'imagerie ultrasonore à haute cadence est donc pertinente pour l'étude du flux et du mouvement tissulaire pour la détection et caractérisation des pathologies artérielles.

Chapitre 2

Ce deuxième chapitre décrit : les méthodes d'estimation de mouvement utilisées sur des images ultrasonores, les travaux précédents de la littérature sur la mesure simultanée du mouvement tissulaire et du flux et les objectifs de la thèse.

Dans la pratique clinique, les méthodes dites Doppler sont très souvent utilisées pour accéder à la vitesse du flux sanguin. Ces méthodes sont basées sur le principe Doppler : si un diffuseur se déplace dans la direction de propagation des ultrasons, son déplacement va se traduire par une modification locale de la phase et de la fréquence du signal rétrodiffusé par le milieu et reçu par la sonde. Cependant, si le mouvement est perpendiculaire à l'axe de propagation des ultrasons, la mesure. n'est plus possible directement. La vitesse mesurée le long de l'axe ultrasonore est un projeté, sur cet axe, de la vitesse réelle. De nombreuses innovations aussi bien technologiques que méthodologiques, visent à réduire l'influence de l'angle entre le flux et la direction du faisceau ultrasonore, afin de rendre ces méthodes plus robustes. Des estimations de flux en 2D sont aussi maintenant possibles avec certaines approches Doppler.

D'autres méthodes d'estimation de mouvement existent, parfois inspirées du monde de la vision par ordinateur, et permettent de trouver un déplacement 2D mais elles sont encore peu utilisées en pratique. Par exemple, l'appariement de blocs consiste à diviser chaque image ultrasonore en sous-blocs et à trouver le déplacement de chaque bloc entre deux images successives, souvent en se basant sur des fonctions de corrélation. Une autre approche est l'utilisation de méthodes différentielles

s'appuyant sur la conservation du flux optique : en supposant que la luminosité d'un objet est constante au cours du temps et de son déplacement, il est possible d'utiliser cette contrainte pour calculer le déplacer entre deux images. Ce problème peut être modélisé par une relation différentielle faisant apparaitre le gradient spatial et le gradient temporelle de l'intensité de l'image.

Dans la littérature, plusieurs études ont été effectuées sur la mesure simultanée dans les artères du flux vectoriel et du mouvement tissulaire depuis le début des années 2000. Des progrès conséquents ont été réalisés, au cours des dernières années, permettant de passer d'estimation de mouvement sur un unique faisceau ultrasonore à des champs de vitesse complets sur l'entièreté de l'image. Ces méthodes en sont encore à la preuve de concept clinique et commencent à prouver leur réel intérêt pour extraire des marqueurs pathologiques dans le système cardiovasculaire à des cadences d'imagerie élevées. Malgré l'intérêt clinique, aucun de ces travaux de recherche ne se concentrent sur l'utilisation des sondes convexes.

Il y a plusieurs années, une technique capable de produire un flux vectoriel 2D, dite "oscillations transverses", a été développée. Plus récemment, cette méthode a été étendue à l'estimation du mouvement des tissus et a par la suite été utilisée pour la mesure simultanée flux/tissu avec une sonde linéaire.

En conclusion de ce chapitre, les méthodes qui seront utilisées au cours de cette thèse ont été sélectionnées après une étude approfondie de l'état de l'art. La méthode d'oscillations transverses semble indiquée dans le cadre de cette thèse et sera par la suite adaptée afin d'être utilisable avec une sonde convexe. Pour atteindre une fréquence d'imagerie élevée, cette méthode est couplée avec une émission ultrasonore ultra-rapide. L'imagerie ultra-rapide fournit néanmoins des images de plus faible qualité que les émissions ultrasonores classiques. Il sera alors nécessaire de combiner plusieurs de ces images afin d'obtenir des images de qualité suffisante même dans les tissus profonds. La séquence ultrasonore doit alors être parfaitement adaptée pour un compromis entre cadence d'imagerie et qualité de l'image finale. Les objectifs de la thèse sont de : concevoir la séquence ultrasonore ultra-rapide, mettre en œuvre la chaîne de traitement permettant l'extraction simultanée du flux et du tissu par oscillations transverses avec un estimateur de mouvement 2D et valider expérimentalement cette technique. Pour se rapprocher d'une possible application de la méthode *in vivo*, des paramètres de sécurité acoustique ont été mesurés afin de prouver que la séquence ultrasonore utilisée dans cette thèse ne présente pas de danger apparent. Une acquisition *in vivo* a alors été réalisée sur l'aorte abdominale d'un volontaire sain, et les données ont pu être traitées.

Chapitre 3

Ce troisième chapitre présente toute la séquence ultrasonore mise en place lors de cette thèse pour obtenir des images ultrasonores de bonne qualité à des cadences d'imagerie élevés même lors d'étude de tissus profonds. Dans un premier temps, l'émission ultrasonore de la sonde convexe utilisée dans cette thèse (CA631- Easote® Italie) a été étudié à l'aide d'un hydrophone. Puis, une émission ultrasonore ultra-rapide permettant d'accéder à des tissus profonds a été réalisée. Ce travail a été publié dans *IEEE International Ultrasonics Symposium* : "Sequence optimization for high frame rate imaging with a convex array" (2020).

Il est important de caractériser l'émission ultrasonore de la sonde utilisée. Une hypothèse courante est de considérer que la sonde n'insonifie que la région 2D qui lui fait face. Cette hypothèse est

évidemment fausse et une région non négligeable est insonifiée en élévation. Cette région dépend des paramètres de la sonde et varie en fonction de la profondeur du milieu étudié. Caractériser correctement la région insonifiée par la sonde permet de localiser la provenance des échos et, ainsi, de mieux comprendre les résultats d'estimation obtenus, en particulier si ces derniers ne sont pas conformes à ce qui est attendu.

La sonde CA631 a un focus géométrique fixé à 6.5 cm de profondeur, ce qui signifie que l'onde ultrasonore envoyée par la sonde est focalisée en élévation à la profondeur 6.5 cm. Lors des mesures avec un hydrophone, ce focus géométrique est bien observé : l'onde ultrasonore en élévation suit une forme de sablier. Ainsi à 3 cm de profondeur, la zone insonifiée en élévation est d'environ 5 mm d'épaisseur, réduite à 2.5 mm à une profondeur de 5 cm, avant d'atteindre le minimum de 1 mm à partir de 5.5 cm de profondeur. Les acquisitions de pression s'arrêtaient à une profondeur de 7 cm. On peut néanmoins supposer sans risque que la zone insonifiée en élévation va par la suite augmenter en suivant la même dynamique. Pour avoir une zone insonifiée en élévation la plus petite possible (1mm), il est nécessaire de se situer entre 5.5 et 7.5 cm avec la sonde CA631.

Un des buts de cette thèse est de fournir une séquence ultrasonore permettant d'étudier des vaisseaux profonds à une cadence d'imagerie assez élevée pour observer les phénomènes rapides ayant lieux dans les artères. L'imagerie ultrasonore classique ne permet pas d'atteindre des cadences d'imagerie supérieures à 100 images par seconde, ce qui est bien trop faible pour notre application. L'imagerie ultra-rapide, consistant à envoyer des ondes ultrasonores non focalisées dans le milieu, ne limite pas la cadence d'imagerie : celle-ci n'est alors limitée que par le temps d'aller-retour de l'onde ultrasonore. Si l'on considère que l'aorte abdominale est située à 20 cm de la peau, sous les muscles abdominaux et du gras, et qu'en moyenne après 80 ans, son diamètre est de 2 cm, la profondeur maximale a imagé pour observer ce vaisseau est d'alors 22 cm. Ceci limite notre cadence d'imagerie à 3 500 images par seconde maximum.

La cadence d'imagerie doit être assez élevée pour observer des phénomènes rapides, comme la vitesse maximale du flux et la vitesse de l'onde de pouls. Si l'on se place dans les cas les plus challengeant (aorte abdominale très rigide, flux très rapide), on peut considérer que le maximum du flux est à 120 cm/s et la vitesse maximum de l'onde de pouls est à 9 m/s. Sans rentrer plus dans les détails dans ce résumé, on peut en conclure que la cadence d'imagerie pour estimer le flux est de minimum 400 images par seconde, et de minimum 1 000 images par seconde pour estimer la vitesse de l'onde de pouls.

On peut en conclure qu'au maximum trois images basses résolutions peuvent être combinées pour respecter la limite de temps d'aller-retour de l'onde ultrasonore et être capable d'estimer des phénomènes rapides. Aucune étude n'a été réalisée pour déterminer comment acquérir ces trois images afin d'obtenir la meilleure image ultrasonore possible. Dans cette thèse, cette étude est réalisée en utilisant des distributions de sources virtuelles choisies en fonction des distributions standards utilisées avec une sonde linéaire. Les différentes distributions ont ensuite été comparées sur un fantôme expérimental (Gammex Sono403™) en fonction de critères de résolution et de contraste. La distribution optimale est la suivante :

- trois sources virtuelles sont placées uniformément sur un arc de cercle ayant pour centre le centre de la sonde convexe et pour rayon le demi-rayon de la sonde. La position de ces sources

virtuelles fixe les délais à appliquer aux éléments de la sonde lors de l'émission. Une de ces sources virtuelles correspond au centre de la sonde,

- la distance entre ces sources virtuelles est fixée par l'angle entre l'axe perpendiculaire à l'élément central de la sonde et la source virtuelle non au centre de la sonde. L'angle donnant les meilleurs résultats avec cette distribution est de 20°,
- l'apodisation choisie en émission consiste en une fenêtre de Hanning sur 128 éléments, qui se décale devant chaque source virtuelle. En réception, une fenêtre de Hanning sur tous les éléments de la sonde est utilisée.

En conclusion de ce chapitre, la séquence ultrasonore la mieux adaptée à nos besoins a été développée. Elle sera utilisée dans le reste de cette thèse. Afin d'éviter au maximum les échos provenant de la zone insonifiée en élévation, il faut si possible se placer à une distance entre 5.5 et 7.5 cm de profondeur. A noter que ces études ont été réalisées sur une sonde CA631, et que certains de ces résultats ne sont pas directement applicable à une sonde convexe possédant d'autres paramètres, notamment pour la distance optimale entre les sources virtuelles.

Chapitre 4

Ce quatrième chapitre décrit : la méthode d'estimation 2D de mouvement dites par "oscillations transverses", la chaîne de traitement et les validations *in vitro* effectués. Ce travail a été publié dans *IEEE International Ultrasonics Symposium*: "High Frame Rate Vector Flow Imaging with a Convex Array in a Simulated Vessel Phantom" (2019).

Les images ultrasonores possèdent naturellement des oscillations dans la direction de propagation des ultrasons. La méthode des oscillations transverses consiste à introduire virtuellement des oscillations transverses dans ces images afin de pouvoir estimer une phase 2D. Sous l'hypothèse d'être suffisamment loin de la sonde et que l'onde soit monochromatique, la réponse impulsionnelle transverse du système d'imagerie est la transformée de Fourier de l'ouverture active (approximation de Fraunhofer). Par conséquent, les oscillations transverses peuvent être introduites en appliquant une pondération spécifique sur les éléments de la sonde. Une solution consiste à pondérer les éléments (émission ou réception) avec une fonction double Gaussienne créant des oscillations transverses dans le milieu. Une autre approche, adoptée dans cette thèse, consiste à effectuer la transformée de Fourier 2D de l'image et à isoler, avec un masque Gaussien, des fréquences transverses spécifiques. Cette introduction d'oscillations transverses directement par un filtrage fréquentiel a été développé pour une sonde linéaire, et n'a pas encore été appliqué à l'utilisation d'une sonde convexe.

Avec une sonde convexe, l'oscillation naturellement présente est dans la direction radiale. Les oscillations transverses seront introduites dans la direction tangentielle. Un estimateur de phase 2D est utilisé dans cette thèse. En séparant les oscillations 2D (dans le domaine de Fourier) en deux signaux analytiques avec une oscillation purement 1D, la variation de phase de chacun de ces signaux peut être estimée en utilisant l'autocorrélation complexe des signaux ; cette approche est similaire aux techniques Doppler 1D déjà existantes. Puis, ces deux informations 1D sont recombinées pour obtenir le déplacement 2D du milieu. L'estimateur fonctionnant principalement dans le domaine de Fourier, les paramètres d'estimation sont facilement modifiables et l'approche est peu coûteuse en temps et puissance de calcul.

La chaîne de traitement mise en place se décompose en quatre étapes : formation des images ultrasonores, estimation du mouvement tissulaire, rehaussement du signal du sang par un filtre de paroi et estimation du flux vectoriel. Une fois les vitesses caractéristiques du flux et du tissu obtenues, la vitesse de l'onde de pouls peut être extraite.

Une première validation a été réalisée en simulation pour le flux sanguin. Cette simulation est une première étape de validation mais permet aussi de tester l'influence des paramètres des oscillations transverses. La validation expérimentale a été réalisée sur un montage produisant une onde de pouls et un flux sanguin dans un fantôme d'artère. Différents fantômes artériels ont été réalisés, possédant quatre rigidités différentes. Une bonne reproductibilité a été observée avec des vitesses d'ondes de pouls estimées suivant la dynamique attendue en fonction de la rigidité des fantômes. De plus, l'estimation du flux a été validée en comparaison avec un spectre Doppler obtenu avec un échographe clinique. Pour prouver la rigidité de l'estimation du flux, l'angle entre le fantôme et le faisceau ultrasonore central a été diminué de 90° jusqu'à 30°. Même avec une telle inclinaison, le flux est correctement estimé, bien que cette estimation soit plus bruitée. Avec une méthode d'oscillations transverses, il est déconseillé d'augmenter cet angle au-delà de 60°, ce qui n'arrive que très rarement en pratique clinique. Grâce à notre méthode, le flux vectoriel et le mouvement de la paroi peuvent être visualisés simultanément sur les images ultrasonores. Le passage de l'onde de pouls peut être observée ainsi que des mouvements complexes du flux, tels que la création de vortex. Cela représente une avancée comparé aux visualisations disponibles en clinique, qui ne permettent ni de visualiser le flux en 2D, ni d'obtenir des informations du flux et du mouvement du tissu simultanément.

En conclusion de ce chapitre, une méthode d'introduction d'oscillation tangentielle 2D rapide a été validée *in vitro* avec un estimateur de mouvement 2D basée sur la phase. Une validation en simulation a permis d'étudier les paramètres des oscillations transverses, puis une validation *in vitro* a permis de valider la méthode aussi bien sur le mouvement tissulaire que celui du flux.

Chapitre 5

Une fois la méthode validée en simulation et *in vitro*, des paramètres de sécurité doivent être évalués sur la séquence ultrasonore avant de pouvoir passer à une étude clinique *in vivo*. Dans ce chapitre, une étude préliminaire des paramètres de sécurité acoustique a été réalisée, suivie d'une acquisition sur l'aorte abdominale d'un volontaire sain.

L'intensité moyenne du pic spatial ainsi que l'index mécanique de l'émission ultrasonore décrite dans le chapitre 3 ont été mesurées. Ces deux paramètres de sécurité sont en accord avec les directives de la Food and Drug Administration américaine pour une application ultrasonore abdominale.

Une fois que les paramètres de sécurité ont été validés, une acquisition sur l'aorte abdominale d'un volontaire sain a pu être réalisée. Le flux et le mouvement tissulaire ont pu être extraits. Le reflux, normalement présent dans une aorte abdominale saine a pu être observé. La vitesse de l'onde de pouls extraite est en accord avec la littérature. Cette étude *in vivo* est une preuve préliminaire du concept clinique. La méthode devra maintenant être appliquée à des sujets sains et à des patients afin de démontrer l'utilité clinique de simultanément accéder au flux et au mouvement tissulaire.

Conclusion

Le but de cette thèse était de développer une séquence d'imagerie ultrasonore ultra-rapide permettant d'extraire simultanément les vitesses du flux et de la paroi sur des vaisseaux profonds imagés avec une sonde convexe, telle que l'aorte abdominale. Pour cela, une séquence ultrasonore « ultra-rapide » a été spécialement développée pour étudier les tissus profonds, qui sont un défi à imager à la fois en posant une limite forte sur la cadence d'imagerie et en résultant en des images ultrasonores relativement bruitées. Puis, une méthode permettant d'extraire simultanément le mouvement 2D du tissu et du flux a été développée. La validation a été effectuée sur un montage expérimental spécialement développé pour le projet, où une onde de pouls se propage dans un fantôme d'artère en présence de flux. Les estimations se sont révélées précises et cohérentes, avec des écarts types et des erreurs faibles, tant pour le flux que pour le mouvement des tissus. Des fantômes de différentes rigidités ont été imagés et l'onde de pouls extraite de chacun d'eux est cohérente avec les courbes attendues. Une fois la méthode validée, des mesures de sécurité acoustique ont été réalisées sur la séquence d'émission ultrasonore. Ces valeurs étant en accord avec les régulations de la Food and Drug Administration (FDA), une acquisition *in vivo* a pu être réalisée sur l'aorte abdominale d'un volontaire sain, et le mouvement pariétal ainsi que le flux ont pu être extraits.

Comme tout travail de recherche, cette thèse présente certaines limites et des points qui auraient pu être approfondis. Tout d'abord, seule la technique d'oscillations transverses a été utilisée, et aucune comparaison avec d'autres techniques d'estimation n'a été réalisée. Le choix de la technique d'oscillations transverses a été guidé par les travaux antérieurs du laboratoire et le fait que la méthode avait déjà été validée pour le tissu et le flux simultanément avec une sonde linéaire. Toutefois, cela ne signifie pas que d'autres méthodes ne pourraient pas donner des résultats similaires, voire meilleurs. De plus, les paramètres des oscillations transverses doivent être choisis avec soin car ils ont un profond impact sur la qualité des estimations. Pour chaque sonde convexe différente, une gamme optimale de fréquences transverses doit être étudiée. Pour la sonde CA631 d'Esaote, nous conseillons d'utiliser une fréquence transverse comprise entre 1 et 1,3°. Comme le flux et le mouvement de la paroi ont des propriétés différentes, il pourrait être utile d'utiliser deux fréquences transverses différentes pour extraire les deux mouvements, comme cela est parfois fait avec une sonde linéaire. Ici, la même fréquence transverse de 1,2° a été utilisée et a permis d'obtenir des estimations pertinentes tant sur le flux que sur le mouvement de la paroi.

Des mesures d'indice de sécurité acoustique préliminaires ont été effectués sur la séquence ultrasonore proposée au cours de cette thèse. Ce test de sécurité n'est pas complet, et certains indices de sécurité n'ont volontairement pas été mesurés, comme les mesures de température. Pour évaluer ces paramètres, les mesures de température doivent être effectuées sur une période de 30 minutes, d'abord dans l'air, puis dans l'eau. Comme la sonde convexe n'a jamais été utilisée au laboratoire pendant une période aussi longue, nous n'avons pas pris le risque d'endommager certains de ses éléments en prenant ces mesures.

Les perspectives comprennent une étude plus approfondie des paramètres de sécurité qui pourrait conduire à une preuve de concept clinique, où des aortes abdominales saines et malades devraient être considérées. Les paramètres avancés accessibles par notre méthode (tels que la vitesse de l'onde de pouls, le taux de cisaillement moyen et maximal de la paroi) devront être extraits. Couplés à des tests statistiques, ils permettront de mesurer précisément l'intérêt et l'apport de la méthode pour la détection de pathologies vasculaires.

L'utilisation d'une sonde 1D génère plusieurs limitations et problèmes. Le placement de la sonde est particulièrement crucial et cela augmente l'inconsistance inter et intra opérateur. L'utilisation d'une sonde matricielle pour l'imagerie ultrasonore 3D permettrait de s'affranchir de ces problèmes de placement et de mouvements hors du plan. Cependant, l'imagerie ultrasonore 3D reste confrontée à des problèmes techniques majeurs : la taille des éléments rend difficile l'obtention d'un bon rapport signal/bruit et le nombre élevé d'éléments entraîne un coût de calcul important pour le traitement du signal et de l'image. De plus, leur faible ouverture ne semble pas appropriée pour les scanners abdominaux.

Dans le futur, nous espérons que cette thèse pourra apporter des informations précieuses sur la formation des maladies vasculaires dans les vaisseaux profonds, qui est aujourd'hui peu comprises. De nouvelles informations sur l'écoulement et l'interaction des tissus pourraient être utiles pour évaluer un modèle théorique d'artère, afin de prédire son évolution en présence de pathologies.